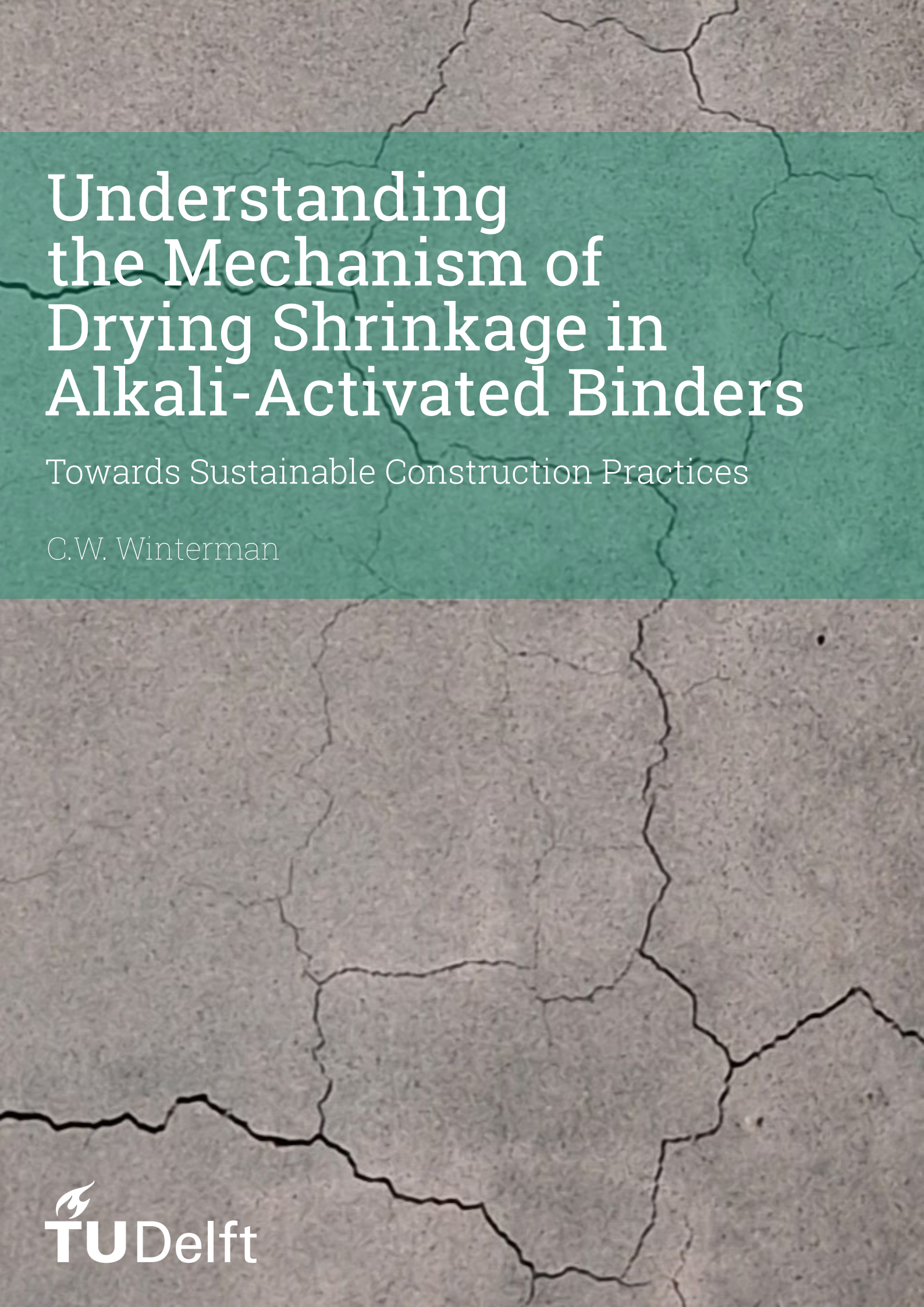

Understanding the Mechanism of Drying Shrinkage in Alkali-Activated Binders

Towards Sustainable Construction Practices

C.W. Winterman

TU Delft

Understanding the Mechanism of Drying Shrinkage in Alkali-Activated Binders

Towards Sustainable Construction Practices

by

C.W. Winterman

to obtain the degree of Master of Science in Civil Engineering
at the Delft University of Technology
to be defended publicly on January 29, 2024 at 14.00h.

Student number:	4579674
Chair:	Dr. ir G. Ye
Thesis committee:	Dr. ir. M. Luković
	Dr. ir. M. Gupta
	Ir. F. Aghabeyk
Project Duration:	February, 2023 - January, 2024
Place:	Faculty of Civil Engineering, Delft

Cover photo made by Christa Winterman.

An electronic version of this thesis is available at https://repository.tudelft.nl/.

TU Delft

Acknowledgements

This master thesis marks the last step towards obtaining my Master's degree in Structural Engineering at Delft University of Technology. In recent months, I have fully immersed myself in scientific research on materials science scale, which I would not have dared to dream of when I started studying eight years ago. From my interest in large constructions and designing and calculating them, I took a leap in the dark to delve into the world of researching an alternative type of concrete. I believe that we all need to try to make the world of tomorrow a bit better, and this thesis feels like a small but valuable contribution.

I am very grateful for the opportunity to work in the lab and will cherish this experience. Conducting experiments and obtaining results is a gratifying experience, especially when you realize afterwards that you have conducted more than 7000 measurements for one experiment. This extensive dataset reflects the dedication and effort invested in the research, providing a robust foundation for the findings in this thesis. I am eager to continue working upon what I have learned during this research, content-wise but also about the approach of performing research.

This study would not have been possible without the support and guidance of my graduation committee. First of all, I would like to be grateful to Guang Ye, to offer me the opportunity to start working on this subject and guidance during my thesis, the discussions we have held have always been substantive and motivating. I really appreciate the understanding and acknowledgement during my concussion and the time to recover from this. Secondly, I want to thank my daily supervisors, Mayank Gupta and Farnaz Aghabeyk for the daily supervision, good discussions, their help in the lab and feedback on my research. I enjoyed working and figuring things out in the lab with you. Thirdly, I want to thank Mladena Luković to give valuable insights and critical comments about alkali-activated materials and drying shrinkage from a different point of view. Regarding the practical challenges in in this thesis, I want to thank Maiko van Leeuwen and Arjan Thijssen for their knowledge, experience and the jokes.

I am also grateful to my family and friends for their support throughout this journey, thanks to their endless support, I always kept my feet on the ground and was able to keep everything in perspective.

This report is something I am really proud of and I hope the people who read enjoy it as well!

Christa Winterman
Delft, January 2024

Abstract

Cement production for concrete is responsible for 5-8% of the global anthropogenic emissions, making it essential to search for alternative binders. This study focuses on alkali-activated materials (AAMs) as a potential replacement for Portland Cement (PC) to reduce carbon emissions. The practical implementation of AAMs in the construction industry faces challenges, particularly related to volume instability caused by drying shrinkage. Drying shrinkage is linked to both water loss through evaporation and the hydration process. The underlying mechanism of drying shrinkage in AAMs is not well understood yet, hindering their widespread application.

The aim of this study is to advance the understanding of the drying shrinkage mechanism in AAMs, by considering the contribution of the pore size distribution and gel characteristics of AAMs. A detailed analysis is performed to identify the governing parameter related to the drying shrinkage mechanism. This is done by controlling the pore size distribution and total porosity at moment of exposure, while differences in the gel composition were obtained. Moreover, the impact of different mix design parameters of blended AAMs on drying shrinkage behaviour, weight loss, microstructural development, flexural and compressive strength are investigated. The selected mix design parameters in this study include slag-to-fly-ash ratio (1, 0.7 and 0.5), curing time (3, 7, 14 and 28 days) and Na_2O wt.% content (4 and 5 wt.%).

Results from the study indicate that drying shrinkage in AAMs is influenced by factors beyond water loss, diverging from the observed correlation in PC. The study highlights important findings related to mix design parameters. In terms of the slag-to-fly-ash ratio, an increase in ground granulated blast furnace slag (GGBFS) content correlates with reduced drying shrinkage, weight loss, refinement of the pore structure and total porosity. Regarding curing time, prolonged curing durations lead to decreased drying shrinkage and weight loss, coupled with improved flexural and compressive strength. As for activator content, an increased amount of activator refines the pore structure, resulting in reduced total porosity, weight loss, and increased compressive strength. However, drying shrinkage remains relatively constant over the 56 days exposure.

Based on the starting point that the pore size distribution of selected samples at the moment of exposure to drying was controlled, it is suggested that gel characteristics, i.e. reaction products, rather than pore size distribution, govern the drying shrinkage phenomenon in AAMs. Comparative analyses underscore the influence of homogeneous reaction products, a higher atomic Ca/Si ratio and the availability of sodium and silicate from the activator. At the moment of exposure, the type of gel is more crucial than the quantity, as demonstrated by the sample with more reaction products exhibiting greater drying shrinkage in the analysis.

The drying shrinkage mechanism in AAMs is strongly correlated with microstructure and the nature of reaction products. The comprehensive results of this study suggest that the gel characteristics have an crucial role as a driving force in the mechanism of drying shrinkage. The study underscores the substantial influence of mix design parameters on drying shrinkage, offering valuable insights for the practical implementation of AAMs in construction. This research marks a significant step forward in enhancing our understanding of this complex phenomenon for AAMs.

The study provides several recommendations for future research, including extending the range of mix design parameters and curing times to evaluate the findings of this study, assessing the rate of reaction of mixtures and considering the impact of drying on the exposed pore structure. Furthermore, the application of N_2 adsorption to detect the smaller range of pores in AAMs, the determination of the influence of internal relative humidity on drying shrinkage, and the investigation of cracking potential of AAMs related to drying shrinkage are also suggested.

Contents

Preface i

Abstract ii

Contents iii

List of Figures v

List of Tables viii

1 Introduction 1
- 1.1 Background information . . . 1
- 1.2 Problem statement . . . 1
- 1.3 Research aim and objectives . . . 3
- 1.4 Scope limitations . . . 3
- 1.5 Outline . . . 3

2 Literature review 4
- 2.1 Alkali-activated materials . . . 4
  - 2.1.1 Precursors: slag and fly ash . . . 4
  - 2.1.2 Characteristics and reaction mechanism of the high-calcium based binders . . . 5
  - 2.1.3 Characteristics and reaction mechanism of low-calcium based binders . . . 6
  - 2.1.4 The blended system of slag and fly ash . . . 7
  - 2.1.5 Curing of AAMs . . . 8
- 2.2 Drying shrinkage in alkali-activated materials . . . 9
  - 2.2.1 Introduction to drying shrinkage . . . 9
  - 2.2.2 Primary concept of drying shrinkage . . . 9
  - 2.2.3 Terminology . . . 10
  - 2.2.4 Fundamental parameters affecting drying shrinkage . . . 10
  - 2.2.5 Factors affecting drying shrinkage in alkali-activated materials . . . 14
- 2.3 Knowledge gaps in drying shrinkage mechanism research . . . 19

3 Approach & Methodology 20
- 3.1 Strategy . . . 20
- 3.2 Design parameters . . . 21
- 3.3 Materials and sample preparation . . . 21
  - 3.3.1 Blast furnace slag and fly ash . . . 21
  - 3.3.2 Alkaline activator . . . 21
  - 3.3.3 Mix design . . . 22
  - 3.3.4 Mixing procedure . . . 22
  - 3.3.5 Sample preparation for drying shrinkage and mechanical properties . . . 22
  - 3.3.6 Sample preparation for MIP and SEM-EDX . . . 23
- 3.4 Test methods . . . 23
  - 3.4.1 Mechanical tests . . . 23
  - 3.4.2 Drying shrinkage test . . . 24
  - 3.4.3 Weight loss . . . 24
  - 3.4.4 Autogenous shrinkage test . . . 25
  - 3.4.5 Mercury intrusion porosimetry . . . 25
  - 3.4.6 SEM-EDX . . . 25
- 3.5 Sample selection based on pore size distribution . . . 26

4 Results 27
- 4.1 Flexural and compressive strength results . . . 27

4.1.1 The effect of slag content on flexural and compressive strength . . . 27
4.1.2 The effect of activator contents on flexural and compressive strength . . . 28
4.2 Drying shrinkage and weight loss . . . 29
4.2.1 Influence of the slag-to-fly-ash ratio on drying shrinkage and weight loss . . . 29
4.2.2 Influence of the curing time on drying shrinkage and weight loss . . . 31
4.2.3 Influence of the activator content on drying shrinkage and weight loss . . . 32
4.2.4 Correlation between drying shrinkage strain and weight loss . . . 33
4.2.5 Autogenous shrinkage and external drying shrinkage . . . 34
4.3 Porosity and pore size distribution results . . . 37
4.3.1 Influence of slag-to-fly-ash ratio on porosity and pore size distribution . . . 37
4.3.2 Influence of the curing time on porosity and pore size distribution . . . 38
4.3.3 Influence of activator content on porosity and pore size distribution . . . 40
4.4 Results of the pore structure analysis and selection . . . 41
4.5 A comparative study: S100N4T3 and S70N4T14 results . . . 42
4.5.1 Drying shrinkage and weight loss results . . . 42
4.5.2 Flexural and compressive strength results . . . 43
4.5.3 Volume of reaction products and chemical composition results . . . 43
4.6 A comparative study: S70N4T7 and S50N5T3 results . . . 46
4.6.1 Shrinkage and weight loss results . . . 46
4.6.2 Flexural and compressive strength results . . . 46
4.6.3 Volume of reaction products and chemical composition . . . 46

5 Discussion **49**
5.1 Result analysis . . . 49
5.1.1 The effect of slag-to-fly-ash ratio . . . 49
5.1.2 The influence of curing time . . . 50
5.1.3 The effect of activator content . . . 50
5.1.4 Correlation between drying shrinkage and mass loss . . . 51
5.1.5 Contribution of external drying shrinkage . . . 51
5.1.6 Correlation of pore and gel characteristics on the drying shrinkage mechanism . . . 51
5.1.7 Compressive and flexural strength development . . . 53
5.2 Drying shrinkage in AAMs: the driving force . . . 54
5.3 Challenges of AAMs . . . 55
5.4 Reflections on experiments and analysis . . . 55
5.5 Novelty of research . . . 56

6 Conclusion and recommendations **58**
6.1 Conclusion . . . 58
6.2 Recommendations . . . 59

References **61**

A Remaining results **66**
A.1 Original data set of flexural and compressive strength results . . . 66
A.2 Drying shrinkage and weight loss results of N5 samples . . . 66
A.2.1 70% BFS, 5 wt.% Na_2O content . . . 66
A.2.2 50% BFS, 5 wt.% Na_2O content . . . 67
A.2.3 50% BFS, 4 and 5 wt.% Na_2O content, 7 and 14 curing days . . . 67
A.2.4 70% BFS, 4 and 5 wt.% Na_2O content . . . 68

B Pictures of samples after compressive strength test **69**

C Pictures of samples during drying shrinkage measurements **70**

List of Figures

1.1 Early age drying shrinkage and water loss of PC and alkali-activated slag concrete (SC). SC1-SC2: M_s = 1.5, %Na_2O = 4, 5; SC3-SC5: M_s = 0.75, %Na_2O = 4, 5, 6; [11]. 2
1.2 Early age drying shrinkage and water loss of PC and alkali-activated fly ash concrete (FC). FC1-FC3: M_s = 1.5, %Na_2O = 4, 5, 6 [11]. 2

2.1 Schematic overview of C-A-S-H gel structure. Blue triangles are tetrahedral Si sites, while the red triangle indicates the Al substitution [9] 6
2.2 Schematic overview of N-A-S-H gel structure [36] 6
2.3 Explanatory model for N-A-S-H gel formation [23] 6
2.4 N-A-S-H gel stability in terms of pH and calcium content [7] 7
2.5 Schematic overview of influence of pore size and RH on meniscus development when water evaporates 9
2.6 Schematizing definition of drying shrinkage 10
2.7 Schematizing definition of autogenous shrinkage 10
2.8 Cummulative pore size distribution of PC and AAS for 3, 7 28 and 56 days [19] 11
2.9 Drying shrinkage vs pore radius for AAS and PC, with w/b = 0.5 [19] 11
2.10 The effect of different FA/GGBFS ratios on cumulative pore size distribution at 3 and 365 days. N: wt.% Na_2O activator content; S: proportion of slag; T: curing time in days. Data from [53, 58] 12
2.11 The effect of amount of fly ash on the drying shrinkage behaviour of alkali-activated blended binders after 3 days, w/b = 0.35, N4: 4 wt.% Na_2O content in the activator; F0-F7: 0-70% fly ash replacement of slag F[53] 12
2.12 Effect of sealed curing on drying shrinkage of blended alkali-activated paste with 60% FA, 40% slag, M_s = 1.5 [61] 15
2.13 Drying shrinkage strain of blended AAMs influenced by both curing time and alkali activation conditions. n: molar ratio of SiO_2/Na_2O [8] 15
2.14 Microstructure of fly ash paste activated with sodium hydroxide after 28 days cured at 40°C (from [63]) 16
2.15 Microstructure of fly ash paste activated with sodium silicate after 28 days cured at 40°C (from [63]) 16
2.16 7 and 28 days porosity of alkali-activated slag-fly ash mortars with M_s equal to 1, 1.4 and 1.8 by [15] 17
2.17 Pore size distribution of mortars with M_s equal to 0, 0.4 and 1.2 [64] 17
2.18 Effect of activator modulus and sodium oxide concentration on drying shrinkage at 6 months of AAS [64] 18
2.19 Drying and autogeneous shrinkage of 2.5% Na_2O mortars [16] 18
2.20 Drying and autogeneous shrinkage of 4.5% Na_2O mortars [16] 18

3.1 Variable mix design parameters 21
3.2 Storage of resealed prisms in standard curing room 23
3.3 Samples for micro-structural analysis 23
3.4 Crushed samples for micro-analysis 23
3.5 Polished S70N4T14 sample ready for analysis 23
3.6 Samples of S50N4T28 after performing the flexural test 24
3.7 Digital length comparator to measure the variation in length 24
3.8 Autogenous shrinkage measurement set up 25

4.1 Flexural strength results of mixtures with 100%, 70% and 50% GGBFS and 4% Na_2O content after 3, 7, 14 and 28 days of curing 27

4.2 Compressive strength results of mixtures with 100%, 70% and 50% GGBFS and 4% Na_2O content after 3, 7, 14 and 28 days of curing . . . 28
4.3 Flexural and compressive strength results of mixtures with 70% GGBFS, 4 and 5 wt.% Na_2O content after 3, 7, 14 and 28 days of curing . . . 28
4.4 Flexural and compressive strength results of mixtures with 50% GGBFS, 4 and 5 wt.% Na_2O content after 3, 7, 14 and 28 days of curing . . . 29
4.5 Drying shrinkage strain and weight loss of samples with 3 days of curing and 4 wt.% Na_2O content . . . 29
4.6 Drying shrinkage strain and weight loss of samples with 7 days of curing and 4 wt.% Na_2O content . . . 30
4.7 Drying shrinkage strain and weight loss of samples with 14 days of curing and 4 wt.% Na_2O content . . . 30
4.8 Drying shrinkage strain and weight loss of samples with 28 days of curing and 4 wt.% Na_2O content . . . 31
4.9 Drying shrinkage strain and weight loss of mixtures with 100% slag and 4 wt.% Na_2O content . . . 31
4.10 Drying shrinkage strain and weight loss of mixtures with 70% slag and 4 wt.% Na_2O content . . . 32
4.11 Drying shrinkage strain and weight loss of mixtures with 50% slag and 4 wt.% Na_2O content . . . 32
4.12 Drying shrinkage strains and weight loss of samples with 50% slag and 4 or 5 wt.% Na_2O content after 3 and 28 days of curing . . . 33
4.13 Weight loss as function of drying shrinkage for PC (data from [17]) and mixtures with 100%, 70% and 50% GGBFS after 7 days of curing over 56 days of exposure in 50% RH 33
4.14 Weight loss as function of drying shrinkage for PC (data from [17]) and mixtures with 100%, 70% and 50% GGBFS over 56 days of exposure in 50% RH . . . 34
4.15 Weight loss as function of drying shrinkage for mixtures with 4 wt.% and 5 wt.% Na_2O content and 50% GGBFS over 56 days of exposure in 50% RH. Curing times are indicated with symbols, T3:● and T28:□. . . . 34
4.16 Autogenous shrinkage of N4 mix designs measured for 28 days . . . 35
4.17 Translation of the coordinate system for S100N4T3 mixture after 3 days of curing, with (3, -4682) as new origin (O') . . . 35
4.18 Proportion of autogenous shrinkage and external drying shrinkage in mixtures with different GGBFS percentages (100%, 70%, and 50%) and 4 wt.% Na_2O content, observed after 3 days (left) and 14 days (right) . . . 36
4.19 Capillary pore volume and differential pore size distribution of mixtures with 3 days of curing and 4 wt.% Na_2O . . . 37
4.20 Capillary pore volume and differential pore size distribution of mixtures with 7 days of curing and 4 wt.% Na_2O . . . 38
4.21 Capillary pore volume and differential pore size distribution of mixtures with 14 days of curing and 4 wt.% Na_2O . . . 38
4.22 Capillary pore volume and differential pore size distribution of mixtures with 100% GGBFS and 4 wt.% Na_2O content . . . 39
4.23 Capillary pore volume and differential pore size distribution of mixtures with 70% GGBFS and 4 wt.% Na_2O content . . . 39
4.24 Capillary pore volume and differential pore size distribution of mixtures with 50% GGBFS and 4 wt.% Na_2O content . . . 40
4.25 Capillary pore volume and differential pore size distribution with 4 and 5 wt.% Na_2O content 40
4.26 Sample selection based on pore size distribution for S100N4T3 and S70N4T14 . . . 41
4.27 Sample selection based on pore size distribution for S70N4T7 and S50N5T3 . . . 41
4.28 Drying shrinkage strains and weight loss of S100N4T3 and S70N4T14 . . . 42
4.29 Proportion of autogenous shrinkage and external drying shrinkage for the S100N4T3 and S70N4T14 mixtures . . . 42
4.30 SEM images of S100N4T3 and S70N4T14 with accelerating voltage of 15 kV, magnitude of 1000 and 10 mm working distance. . . . 43

4.31 2D scatter plots of EDX point analysis of Na/(Si+Al) and Ca/(Si+Al) ratios for S100N4T3 and S70N4T14 44
4.32 Atomic ratios of the elements in the matrix of the S100N4T3 and S70N4T14 45
4.33 Ternary diagram of normalised Ca/Si, Na/Si and Al/Si ratios for S100N4T3 and S70N4T14 45
4.34 Drying shrinkage strains and weight loss of S70N4T7 and S50N5T3 46
4.35 SEM images of S70N4T7 and S50N5T3 with accelerating voltage of 15 kV, magnitude of 1000 and 10 mm working distance. 47
4.36 2D scatter plots of EDX point analysis of Na/(Si+Al) and Ca/(Si+Al) ratios for S70N4T7 and S50N5T3 47
4.37 Atomic ratios of the main elements in the matrix of the S70N4T7 and S50N5T3 48
4.38 Ternary diagram of normalised Ca/Si, Na/Si and Al/Si ratios for S70N4T7 and S50N5T3 48

5.1 Relationship between compressive and flexural strength for different types of alkali-activated concretes, including the relationship of PC concretes indicated with ACI 318-02 [12], including results from this research. 53

A.1 Drying shrinkage strain and weight loss of samples with 70% slag and 5 wt. % Na_2O content 66
A.2 Drying shrinkage strain and weight loss of samples with 50% slag and 5 wt.% Na_2O content 67
A.3 Drying shrinkage strains and weight loss of samples with 70% slag and 4 or 5 wt.% Na_2O content after 7 and 14 days of curing 67
A.4 Drying shrinkage strains and weight loss of samples with 70% slag and 4 or 5 wt.% Na_2O content after 3 and 28 curing days 68
A.5 Drying shrinkage strains and weight loss of samples with 70% slag and 4 or 5 wt.% Na_2O content after 7 and 14 curing days 68

B.1 Pictures of samples after compressive strength test, showing brittle failure 69

C.1 Pictures of samples with 50% GGBFS during drying shrinkage measurements 70
C.2 Pictures of samples with 100% GGBFS during drying shrinkage measurements 71

List of Tables

2.1 Classification of pore sizes in AAMs according to Mindess *et al.* [54] 11

3.1 Chemical composition of GGBFS and FA measured with XRF [wt.%] (data from [65]). . 21
3.2 Mix designs of all samples. 22

4.1 Final setting time results according to EN 196-3 34
4.2 Porosity by mercury intrusion of mixtures 37
4.3 Results of flexural and compressive strength of S100N4T3 and S70N4T14 43
4.4 Mean atomic ratios and amount of reaction products of S100N4T3 and S70N4T14 . . . 43
4.5 Results of flexural and compressive strength of S70N4T7 and S50N5T3 46
4.6 Mean atomic ratios and amount of reaction products of S70N4T7 and S50N5T3 46

A.1 Flexural strength of all samples in MPa 66
A.2 Compressive strength of all samples in MPa 66

1 Introduction

1.1. Background information

Concrete has become one of the most widely consumed products globally, second only to water [1]. Its popularity can be attributed to its affordability, widespread availability, resistance to water and a variety of shapes and sizes that can easily be made [2]. The composition of concrete involves the combination of water and cement, which acts as a binder when combined with aggregates. Nowadays, the majority of cement used is Portland Cement (PC), which is easily produced by burning limestone and clay. The production of PC contributes to anthropogenic CO_2 emissions, accounting for 5-8% of global emissions [3].

To combat climate change and limit global temperature rise well below 2 °C, 196 parties agreed to the Paris Agreement in 2015 [4]. The harmful emissions of greenhouse gasses should be limited as soon as possible, to reach a climate-neutral world in 2050. The Dutch government has set a target for the building sector to become fully circular by 2050, prompting the exploration of various pathways to decrease the carbon footprint of the world's second most utilized material. This thesis focuses on investigating an alternative binder as a potential substitute for PC. Alkali-activated materials (AAMs) are considered a viable and sustainable alternative, given their potential to reduce the CO_2 emissions by 80-90% compared to PC [5].

Alkali-activated materials are created by aluminosilicate precursors that need to be activated in an alkaline environment to form a hardened binder, in order to serve as binding agent to hold the aggregates in concrete together [6]. Precursors consist of a wide range of solid industrial by-products, raw materials and recycled aluminosilicates [7]. Among the industrial by-products, the most popular and extensively studied materials are ground granulated blast furnace slag (GGBFS) and fly ash (FA) [8, 9]. The use of alkali-activated binders offers the advantage of reducing waste streams and CO_2 emissions, thereby benefiting the environment [7, 10, 11]. AAMs exhibit promising properties regarding strength development, mechanical characteristics, chloride resistance, fire resistance and acid resistance [7, 12].

1.2. Problem statement

The practical implementation of AAMs as marketable products in the construction and building industry faces challenges due to volume instability, particularly drying shrinkage [11, 13, 14]. Drying shrinkage, a complex phenomenon associated with the evaporation of free water from the pores of hardened materials, will be elaborated in section 2.2.2 [10, 15, 16]. While the mechanism of drying shrinkage in PC can be directly associated with weight loss of water, the mechanism of AAMs is more complex, involving various different chemical and physical processes [17, 18].

The impact of drying shrinkage in AAMs has been extensively documented in literature, and demonstrated that AAMs containing materials such as GGBFS or FA exhibit a two to six times higher magnitude of shrinkage and shrinkage strain compared to equivalent PC [11, 17–19]. Figure 1.1 presents a

comparison between concrete specimens including GGBFS and PC, varying the amount of activator concentration and activator modulus [11]. The figure illustrates that in extreme cases, the shrinkage strain is nearly twice as high for alkali-activated slag concrete compared to PC concrete, while the mass loss is approximately four times lower. Additionally, a comparison between PC and alkali-activated slag binders shows that while slag binders experience lower mass loss, they display a higher magnitude of drying shrinkage and faster shrinkage kinetics [11, 13]. For this reason, the direct relation between mass loss and shrinkage strain used for PC is not valid for AAMs. Similarly, Figure 1.2 shows the comparison between concrete specimens including FA and PC, highlighting the same distinction between shrinkage strain. However, the mass loss is higher compared to PC, due to higher availability of evaporate water and porosity in alkali-activated fly ash binders [11].

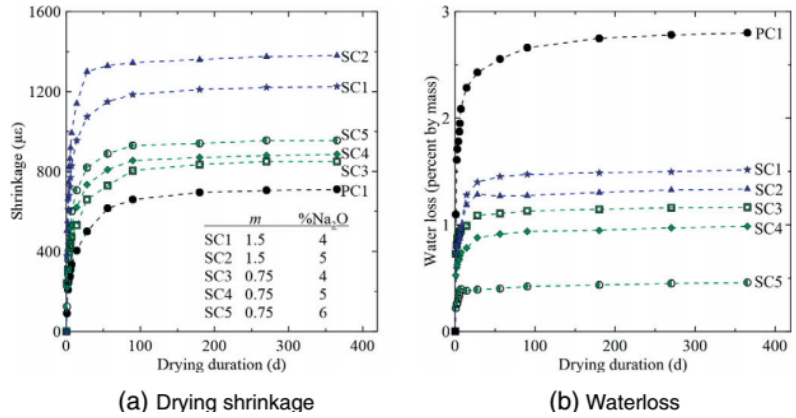

Figure 1.1: Early age drying shrinkage and water loss of PC and alkali-activated slag concrete (SC). SC1-SC2: M_s = 1.5, %Na_2O = 4, 5; SC3-SC5: M_s = 0.75, %Na_2O = 4, 5, 6; [11].

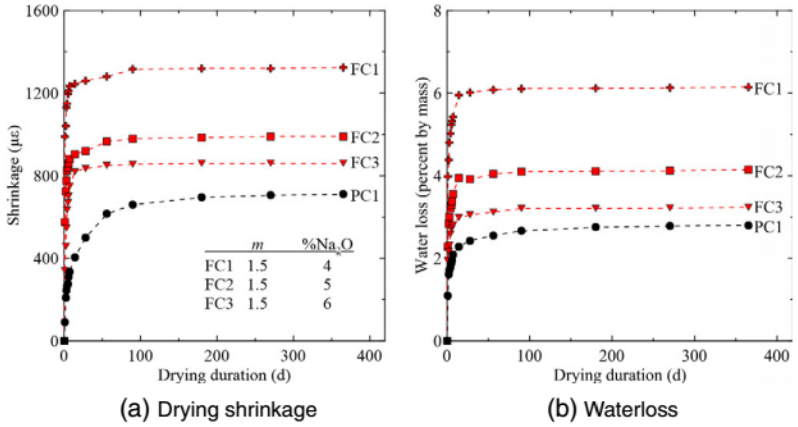

Figure 1.2: Early age drying shrinkage and water loss of PC and alkali-activated fly ash concrete (FC). FC1-FC3: M_s = 1.5, %Na_2O = 4, 5, 6 [11].

The drying shrinkage of AAMs is influenced by various parameters, including raw material properties, mix design and curing conditions. This complexity poses challenges in both controlling and accurately predicting drying shrinkage behaviour [13]. While previous research extensively addressed the differences in magnitude, there remains a limited understanding of the mechanism responsible for drying shrinkage in AAMs [18]. Additional research is needed to explore the parameters influencing this mechanism and establish a scientific understanding, especially in correlating microstructure with drying shrinkage [18, 20–22]. To overcome these challenges, it is crucial to comprehend the mechanism of drying shrinkage in alkali-activated binders and its consequences for engineering practice.

1.3. Research aim and objectives

The primary aim of this thesis is to advance the understanding of the drying shrinkage mechanism in alkali-activated binders. This thesis aims to unveil the microstructural feature governing the drying shrinkage mechanism in AAMs, considering the pore size distribution and gel characteristics. By doing so, this thesis will not only contribute to the knowledge base but also provide a foundation for the development of strategies. These strategies ensure the sustainable implementation of alkali-activated materials in construction and building practices, promoting a more environmentally friendly and circular construction industry.

To reach the research aim, the following research objectives are stated:

1. To determine the influence of mix design parameters, such as slag-to-fly-ash ratio, curing time and Na_2O wt.% content, on the drying shrinkage behaviour and mechanical properties of alkali-activated binders. This objective seeks to provide a comprehensive understanding of how these parameters affect the pore structure and gel characteristics parameters and therefore the performance of alkali-activated materials.
2. To study the influence of mix design parameters on the development of the microstructure of alkali-activated binders. This objective strives to unveil the microstructural changes induced by variations in the mix design, with the goal of revealing their contribution to the phenomenon of drying shrinkage.
3. To attain a fundamental understanding of drying shrinkage mechanism by thoroughly examining the pore structure and gel characteristics of alkali-activated materials. This objective is dedicated to identifying which fundamental parameter exerts the most significant influence on the mechanism through comprehensive analysis of pore structure and gel characteristics in alkali-activated binders.

1.4. Scope limitations

In order to ensure the completion of this research within the allocated time frame, certain limitations have been imposed on its scope. The scope limitations of this research include the following:

- Precursor: This study focuses on two precursors, namely ground granulated blast furnace slag and fly ash class F. Other precursors are not considered in this research.
- Sample type: The study is conducted only on paste samples. Other forms, such as mortar or concrete, are not included.
- Curing time constraint: The maximum curing time for samples is limited to 28 days. Extended curing periods beyond this duration are not investigated.
- Drying shrinkage experiment duration: The drying shrinkage experiments are conducted up to a maximum period of 56 days.

1.5. Outline

To achieve the formulated research aim, this thesis is subdivided into distinct chapters. The state of the art of alkali-activated materials, the mechanism of drying shrinkage, fundamental parameters and factors affecting drying shrinkage in alkali-activated materials are addressed in Chapter 2. Chapter 3 covers the formulated research structure, the chosen design parameters, used materials, sample preparation and the test methods applied in this study. Chapter 4 provides insight into all results gained from the performed experiments. In Chapter 5, the result analysis, the challenges of AAMs, reflections on the performed and analysis and the novelty of research are discussed. Chapter 6 finishes by giving conclusions found in this research and providing recommendations for future research.

2

Literature review

2.1. Alkali-activated materials

As mentioned in the introduction, AAMs consist of various aluminosilicate precursors and activators, combined to create an alternative binder for Portland cement (PC) [23, 24]. AAMs require the inclusion of alkali activators to initiate a chemical reaction that results in the formation of a hardened binder [9]. The most commonly used precursors in AAMs are by-products from the industry, with fly ash, ground granulated blast furnace slag, and metakaolin being the predominant choices in conducted research [7, 9]. Precursors differ in terms of availability, reactivity, CO_2 emission, chemical properties, resulting in diverging mechanical properties [18]. Within alkali-activated materials, the calcium content of the precursor plays a crucial role, resulting in the formation of distinct binder systems. The presence these systems gives rise to variations in the activation process, reaction mechanism, and final hydration products. The binder systems have been defined as [7, 9, 18]:

1. High-calcium ($(Na, K)_2O - CaO - Al_2O_3 - SiO_2 - H_2O$) based binder system
2. Low-calcium ($(Na, K)_2O - Al_2O_3 - SiO_2 - H_2O$) based binder system
3. Blended alkaline system

This section focuses on selected precursors, characteristics and reaction mechanisms of high- and low-calcium based binders, the blended system of GGBFS and FA, and the role of curing in AAMs.

2.1.1. Precursors: slag and fly ash

This thesis focuses on ground granulated blast furnace slag and fly ash, as they exhibit highly promising characteristics for the large-scale production of alkali-activated materials [12]. These industrial byproducts contribute to waste reduction, recycling, and environmental benefits. They are extensively utilized as supplementary cementitious materials in concrete production due to their notable pozzolanic properties. These properties enable them to react with calcium hydroxide in the presence of water, forming additional cementitious compounds [25]. While both materials contribute to enhancing concrete properties and reducing environmental impact by replacing PC, they exhibit distinct characteristics and behaviours in the alkali-activated materials system [7].

Ground granulated blast furnace slag is an industrial by-product that is produced during the iron and steel production process, primarily composed of silicates and aluminosilciates [2, 9, 13, 26]. During production, molten iron flows down the furnace, while it reacts with impurities resulting in molten slag that flows on top of the molten iron. This molten slag is tapped from the furnace and rapidly cooled in water [26]. Afterwards, the residues are dried and finely ground into a powder. The chemical and physical properties of GGBFS are constant, which can be attributed to quality control during iron production and the homogeneous nature of the material [27]. However, the chemical composition of GGBFS can vary due to differences in the composition of raw materials and the locations of furnaces in the production process [25, 27]. The composition of GGBFS typically consists out of 35-40% CaO, 25-35% SiO_2, 5-15% Al_2O_3 and 5-10% MgO [28]. The shape of GGBFS particles is irregular, with a glassy surface.

GGBFS exhibits latent hydraulic behavior, meaning it has the ability to react with water and form cementitious compounds over time [25]. Furthermore, the reactivity of GGBFS is influenced by particle size. Smaller particles react more rapidly, while larger particles require a longer time to fully react. Therefore, controlling the pore size distribution of GGBFS can be tested to manage the strength development [27].

Fly ash is a by-product of coal combustion in power plants, generated during electricity production. It forms when finely powdered coal is exposed to high temperatures, causing mineral impurities to melt and transform into fine spherical glass particles [9]. These particles, referred to as fly ash, are carried by the flue gas stream and subsequently separated using a range of techniques [2]. Due to variations in coal sources and combustion processes applied in power plants, the fly ash can show significant variations in terms of chemical composition, alkali content, glass phase fraction and particle size distribution [7, 9, 22, 27]. The primary chemical components of fly ash are silica (SiO_2), alumina (Al_2O_3) and calcium oxide (CaO) [26]. It presents a heterogeneous mineral composition, comprising both amorphous and crystalline (mainly quartz and mullite) phases [29]. In accordance with classification esthablished by the American Society for Testing Materials (ASTM) C618, fly ash can be sorted into two categories [30]. This categorization is dependent on the content of calcium, silica, alumina and iron present. Class C includes high calcium content ($\geq$ 20% CaO), whereas Class F fly ash includes lower CaO levels ($\leq$ 7%) [27]. Characterized by a spherical shape, fly ash particles enhance paste workability by reducing water demand and optimizing particle packing. Consequently, the combined leads to a reduction in overall porosity [27].

2.1.2. Characteristics and reaction mechanism of the high-calcium based binders

High-calcium binder systems are defined with a Ca/(Si+Al) ratio of approximately 1 and mainly formed using GGBFS, which is rich in calcium and silicon (CaO + $SiO_2 \geq$ 70%) [7, 9]. The high-calcium based system can be activated at room temperature under moderate alkali conditions [7, 12]. The main hydration products are calcium-alumino silicate hydrate (C-A-S-H) gels, that usually coexist with secondary hydration products, like crystalline phase of hydrotalcite type ($Mg_6Al_2CO_3(OH)_{16} \cdot H_2O$) and C_4AH_{13}-type phases [7, 31, 32]. The formation of secondary hydration products depends on the composition and structure of slag, the type and concentration of activator, pH and curing conditions [9, 31, 32]. C_4AH_{13}-type phases form when the system is activated with only NaOH, whereas the presence of hydrotalcite-like phases can be detected when waterglass, NaOH, or a combination of these activators is used [7].

Documented beneficial properties of high-calcium based binders compared to PC are high early and final flexural and compressive strength, decrease in total porosity, lower hydration heat and better resistance to high sulfate and seawater environments [9, 18, 22]. They also present some disadvantages compared to PC as quick setting, higher drying and autogeneous shrinkage strains with micro-cracking formation [31, 32].

Glukhovsky and Krivenko proposed in 1994 a series of reaction mechanism in the alkaline activation with GGBFS, including the reactions below [33, 34]. In this model, it can be observed that the alkaline cation (R^+) is the catalyser in the first phases of the hydration process, by cationic exchange with Ca^{2+} ions. The activation involving slag consists of multiple stages, from slag destruction to polycondensation, making it a complex process.

$$\equiv Si - O^- + R^+ \equiv\equiv Si - O - R \tag{2.1}$$

$$\equiv Si - O - R \equiv\equiv Si - O - R - OH^- \tag{2.2}$$

$$\equiv Si - O - R - OH^- + Ca^{2+} \equiv\equiv Si - O - Ca - OH + R^+ \tag{2.3}$$

C-A-S-H gel is the main reaction product of high-calcium based systems, with a disordered tobermorite C-S-H structure [12, 31]. The gel is slightly different compared to C-S-H gel of PC, due to the incorporation of aluminium, having a lower C/S ratio (C/S = 0.9-1.2) [7, 32]. A schematic overview of a C-(A)-S-H layered structure is given in Figure 2.1, showing that the incorporation of aluminium predominantly takes place in the bridging tetrahedral sides. In addition, the substitution of aluminium is limited

by the total Al/Si ratio as this influences the degree of cross-linking of the gel [9]. The formation of the gel can be influenced by the activator used, as a more ordered nanostructure with higher Ca/(Si+Al) ratio is created working with sodium hydroxide [9]. The developed matrix with C-A-S-H gels are dense [35]. Due to the presence of calcium, C-A-S-H-type gels are created which reduce the permeability due to the capacity to chemical binding of water [9].

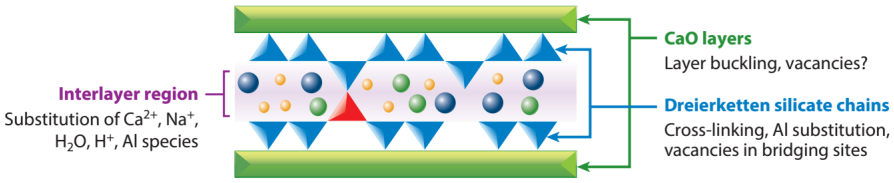

Figure 2.1: Schematic overview of C-A-S-H gel structure. Blue triangles are tetrahedral Si sites, while the red triangle indicates the Al substitution [9]

2.1.3. Characteristics and reaction mechanism of low-calcium based binders

Low-calcium based systems consist primarily of aluminium and silicon, activated with low calcium based materials such as metakolin and type F fly ash [7]. The main hydration product of low-calcium binders is sodium aluminosilicate hydrate (N-A-S-H) gel, which is structurally disordered and highly cross-linked, as can be seen in Figure 2.2 [9]. Similarities can be found between the N-A-S-H gels and zeolites, which in addition is the secondary reaction product in various forms [7, 9]. The reaction temperature plays an important role regarding the activation of low-calcium based binders, as high temperatures (60-200°C) are required to initiate the reaction [32]. In addition, high alkaline environments and therefore more aggressive working conditions are necessary [7].

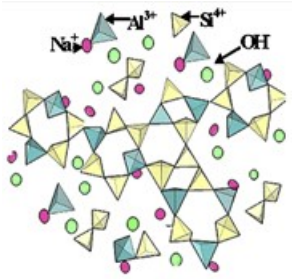

Figure 2.2: Schematic overview of N-A-S-H gel structure [36]

For low-calcium based binder systems, the reaction mechanism of Glukhosvky (1994) is primarily followed in past research, which includes the following steps: (a) destruction-coagulation; (b) coagulation-condensation; and (c) condensation-crystallisation [33]. A descriptive model following these steps is given in Figure 2.3 [23]. During the first stage, alkali break down Si-O-Si, Al-O-Si and Al-O-Al bonds. Subsequently, polycondensation takes place resulting in the formation of clusters growing in all directions [7, 23]. Finally, N-A-S-H gel synthesis continues resulting in reaction products whose chemical composition is dependent on the nature of origin constituents, curing conditions and the origin and concentration of the activator [24, 37].

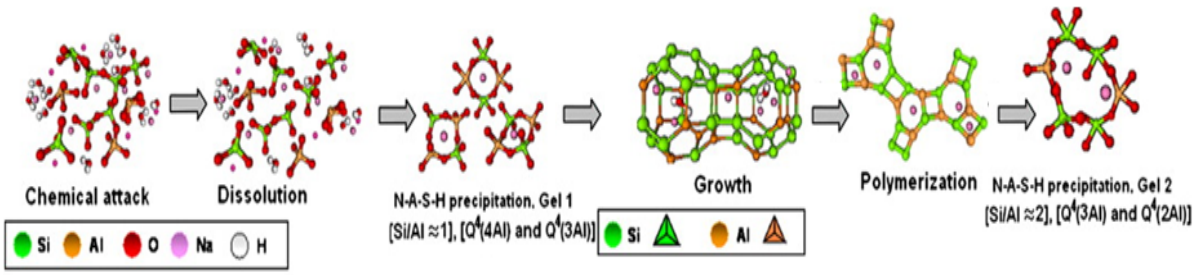

Figure 2.3: Explanatory model for N-A-S-H gel formation [23]

When mixing FA, less water is demanded due to its unique spherical shape [27]. Furthermore, the setting time is longer relative to high-calcium binders [38]. The presence of anion-binding mechanisms slows chloride ingress, enhancing the resistance of low-calcium binders to aggressive environments, attributed to their more porous structure [9]. Despite these advantages, limitations result from low compressive strength and elastic modulus, coupled with low reactivity at room temperature, make them insufficient for structural applications [18].

The addition of soluble silica to the binder enhances the structural stability of the N-A-S-H gel [37]. The properties of both N-A-S-H-type and zeolite-type gels vary depending on factors such as curing temperature, curing time and activator content [13]. Maintaining longer curing times promotes the development of mechanical strength by increasing the degree of reaction and the formation of silica-rich products [7]. Finally, it is important to note that water does not act as a structural component in N-A-S-H gel, as it is not chemically bound [9, 39]

2.1.4. The blended system of slag and fly ash

In this section, the focus is on the blended system consisting of mixtures using GGBFS and FA. The resulting reaction products are a mix of various gels, depending on the reaction conditions. These gels include compositions of C-A-S-H, C-N-A-S-H and N-A-S-H gels [7]. Binders with a moderate calcium content may offer a compromise between durability and strength, as the properties of fly ash and slag are counterbalanced, leading to the development of a more uniform microstructure [40, 41].

It has been documented that when the amount of slag ranges between 25-50%, there is a transition from N-A-S-H to C-A-S-H [39]. Moreover, when the amount of fly ash increases the binding phase becomes less dense, as the N-A-S-H gel exhibits lower density.

Studies have shown that co-precipitation of two gels is possible, however Garcia-Lodeiro *et al.* stated that the gels are interacting with each other, instead of developing as two separate gels [42]. Figure 2.4 illustrates the stability of the blended gel system, which primarily depends on the calcium content and pH [7, 18]. The N-A-S-H gel becomes unstable for high pH (>12) [42]. When the calcium content increases, a transformation from N-A-S-H to C-A-S-H gel can be observed, causing an increase matrix density [7]. The formation of C-A-S-H gel products results in a denser microstructure, as this reaction product is more space-filling compared to N-A-S-H gel [41, 43, 44]. The strong influence of calcium on the gel chemistry is clearly evident in a system with fly ash/slag ratio of 1, as the microstructural features closely resemble the slag-based binder system rather than a fly ash based system [43]. In addition, the amount bound water is affected within the gel, considering N-A-S-H gel cannot chemically bind water [43]. An increase in curing time results in higher polymerisation and cross-linking of the C-(N)-A-S-H gel, but can also provide generation of more N-A-S-H gel (when enough alumina and alkali are present (Al/Si ≈ 0.15))[45].

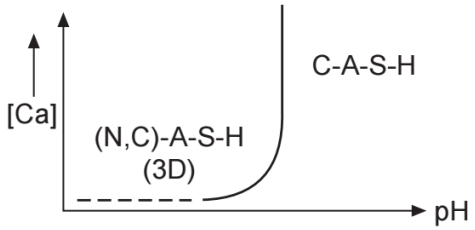

Figure 2.4: N-A-S-H gel stability in terms of pH and calcium content [7]

In conclusion, AAMs offer an alternative binder composed of various precursors and activator. The formation of different gel systems, such as high-calcium (C-A-S-H) and low-calcium (N-A-S-H), is dependent on the composition of the activators. The high-calcium binder system displays a stiffer and more ordered structure compared to PC. Moreover, it includes better mechanical properties and the ability to chemically bind water. On the other hand, the low-calcium based binder system is structurally disordered and highly cross-linked, shows exceptional resistance against aggressive environments.

Additionally, a blended system leads to the coexistence of gel compositions, from C-A-S-H to C-N-A-S-H and N-A-S-H gels. The transition from N-A-S-H to C-A-S-H gel occurs when the calcium content increases, resulting in a denser microstructure and the capacity to chemically bind water.

2.1.5. Curing of AAMs

Curing of AAMs involves the management of specific conditions to promote the hydration of precursors. Similar to traditional concrete, these conditions include factors such as time, relative humidity (RH) and temperature [2]. These curing conditions are introduced shortly after the placement of the AAM mixture, and their significance lies in their capacity to facilitate the necessary chemical reactions. In the subsequent section, these factors and their implications in the context of AAMs development is provided.

Relative humidity

The RH maintained during the curing process plays an important role in microstructural development of AAMs. The level of RH directly impacts the availability of moisture, influencing the duration of the hydration process. Continuing higher RH levels ensures a longer hydration process, promoting the creation of a stronger matrix. This can be done by creation of an impermeable membrane through techniques like moist curing. This impermeable membrane prevents premature drying of the binder, retaining the unaffected hydration process maintaining the desired rate of strength development [2]. Sealing is another effective strategy to prevent moisture loss, as it creates a barrier against water escaping from the system. However, even after both sealed and moist curing, exposure of AAMs to environmental conditions can still impact the binder, potentially leading to issues such as cracking, especially in lower RH environments.

A study by Criado *et al.* focused on the activation of AAFA, revealing the influence of curing conditions on both nano- and microstructural development. Curing at a high relative humidity (above 90%), within airtight containers results in a compact and dense material with developing mechanical properties over time. On the other hand, curing at low relative humidity, in direct contact with the atmosphere results in a granular, porous material with stable, aluminum-rich reaction products. Despite the structural differences, the chemical composition remains consistent during the curing process, ultimately contributing to a weaker matrix [46].

Curing temperature

The impact of curing temperature is dependent on the type of system that is considered, for low-calcium based systems elevated temperatures (60-200 °C, depending on reactivity of fly ash) are needed before hydration products can be created [9, 47]. For high-calcium based systems, elevated-temperature water (up to 60°C) accelerates the early hydration products of the pastes [48]. This accelerates the geopolymerization process leading to earlier strength gain.

The curing temperature has been observed to impact the reaction products. At elevated temperatures (60-80 °C), both C-A-S-H and N-A-S-H gels coexist, while at room temperature, there is a dominance of C-A-S-H gel, which is considered more stable [8].

Curing time

Curing time is the time that specimens are kept under specific curing conditions to promote hydration and gain strength. In general, the longer curing time is included, the better the microstructure development is. Additionally, the overall porosity reduces with increasing time. The demanded curing time of the alkali-activated mixture is dependent on the temperature, activation conditions and setting time [12]. When longer curing times are considered, silica-rich products can be formed which favour the development of mechanical strength in low-calcium based binders [24].

2.2. Drying shrinkage in alkali-activated materials

This section provides an introduction to drying shrinkage, followed by the primary concept of drying shrinkage based on the literature. Subsequently, the fundamental parameters affecting drying shrinkage are described, specifically the pore size distribution and gel characteristics. Finally, the factors influencing drying shrinkage in alkali-activated materials are addressed.

2.2.1. Introduction to drying shrinkage

Drying shrinkage refers to the dimensional changes related to the water loss to the external environment at low RH [2, 11, 18]. The drying shrinkage of PC and AAMS is the time-dependent strain measured in an unrestrained and unloaded specimen at constant temperature [49]. Drying shrinkage starts when specimens are exposed to drying, due to a difference in RH, initiating evaporation of free water. When the stresses due to shrinkage exceeds the tensile stresses, cracking occurs [2, 11].

The dominant mechanisms involved in the drying shrinkage of cementitious materials include the capillary pressure mechanism, disjoining pressure mechanism, the solid surface energy mechanism, and interlayer water movement mechanism [35, 40, 48, 50]. In PC, capillary pressure emerges as the primary mechanism governing the drying shrinkage when the relative humidity exceeds 40% [40]. Consequently, this study focuses on the capillary pressure mechanism as primary concept, which is extensively detailed in section 2.2.2. Moreover, the fundamental parameters associated with drying shrinkage in alkali-activated are described, followed by an examination of the various mix design and curing parameters that contribute to this phenomenon.

2.2.2. Primary concept of drying shrinkage

The capillary pressure theory is based on the developing surface tension on the pore walls due to the formation of the meniscus by the loss of water [40]. In literature, the capillary stress σ_{cap} is described by the Kelvin - Laplace equation:

$$\sigma_{cap} = \frac{2\gamma \cos\theta}{r_c} = \frac{-ln(RH)RT}{V_m} \tag{2.4}$$

Where γ represents the surface tension between vapor and pore water, θ is the contact angle, r_c is Kelvin radius (capillary radius at the position of the meniscus), RH is relative humidity, R is the universal gas constant, T is temperature in Kelvin, V_m is the molar volume of the liquid. The RH and pore solution properties play a critical role in the determination of the Kelvin radius [13].

When free water evaporates, an internal drop of RH is generated within the paste, producing capillary tension due to the existence of menisci on the liquid interface. The capillary tension must be counteracted by compressive stress resulting in contraction of the paste, causing drying shrinkage [17]. Equation 2.4 reveals that for smaller pores, the capillary stress is higher and causing higher drying and autogenous shrinkage. In Figure 2.5, the development of the menisci under different RH is illustrated, as when the RH decreases, water evaporates and the pore size where the meniscus if formed becomes smaller. As equilibrium is created at the meniscus, internal stresses increase as pore size decreases. In the case of AAMs, the volume fraction of smaller pores is higher, causing an increase of capillary tension acting on the matrix phases, which ultimately results in an amplified increase in drying shrinkage [17].

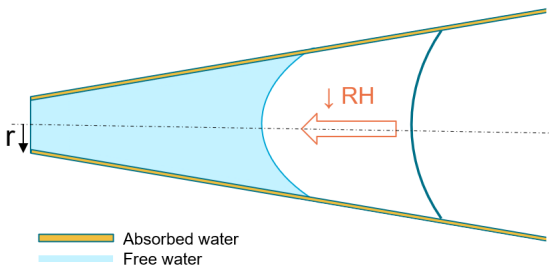

Figure 2.5: Schematic overview of influence of pore size and RH on meniscus development when water evaporates

2.2.3. Terminology

As mentioned above, drying shrinkage is associated with the loss of water to the environment caused by differences in RH. According to ASTM 596, drying shrinkage is defined as the decrease in length of a test specimen, attributed to factors other than externally applied forces [51]. This volume change is a result of both moisture exchange with the environment and internal reactions within the paste during hydration. Figure 2.6 schematizes the concept of drying shrinkage. Exposure to lower RH conditions increases drying shrinkage over time. However, if a specimen is restrained, tensile stresses can develop, potentially causing cracking due to drying shrinkage [2].

Autogenous shrinkage is exclusively related to the volume change without any moisture exchange with the environment. ASTM C1698 defines autogenous shrinkage as the bulk strain of a sealed specimen not subjected to external forces, measured from the final setting until a specified age [52]. Autogenous shrinkage arises only from internal drying of the microstructure, as illustrated in Figure 2.7. The mechanisms for autogenous shrinkage differ between materials; for PC, it is linked to microstructure development, RH, and chemical reactions. Conversely, in alkali-activated fly ash (AAFA), research suggests that autogenous shrinkage is not caused by the traditional self-desiccation process but is associated with the continuous reorganization and polymerization of the alumino-silicate gel structure [17]. Despite these differences, both materials have in common that water is consumed from hydration products during the the reaction process.

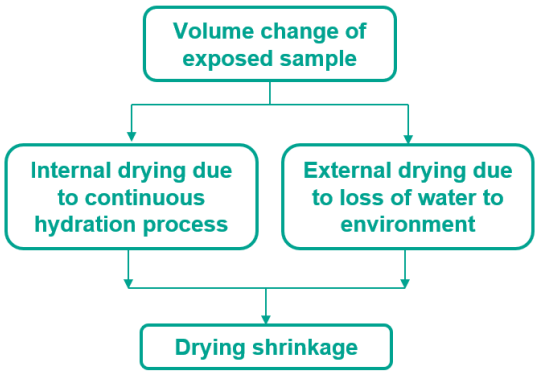

Figure 2.6: Schematizing definition of drying shrinkage

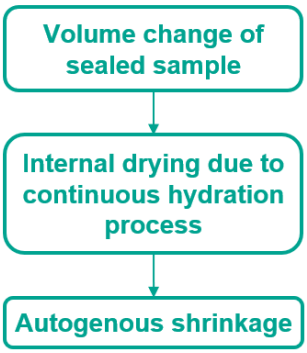

Figure 2.7: Schematizing definition of autogenous shrinkage

To summarize, autogenous shrinkage is related to the internal reactions of hydration and the resulting self-desiccation, while drying shrinkage is associated with both the hydration process and external water loss due to environmental conditions. Previous investigations into drying shrinkage primarily focus on the external part; nevertheless, measurements often include both internal and external drying processes [11, 17, 19, 53]. To exclusively study the contribution of external drying shrinkage, it is necessary to account for the autogenous shrinkage component by separate measurements. From this point in the thesis, external shrinkage is specifically defined as the water loss to the external environment.

2.2.4. Fundamental parameters affecting drying shrinkage

The drying shrinkage mechanisms of both AAMs and PC can be related to pore size distribution and reaction products. However, due to the influence of considerably more factors on these parameters in AAMs, the drying shrinkage mechanism in AAMs is more complex [13, 18, 19, 35, 48]. The pore size of AAMs is finer relative to PC, but includes differences between high-calcium, low-calcium and blended based binders. In addition, the differences in gel characteristics may have its influence on drying shrinkage, because the hydration products influence the solid skeleton in AAMs and therefore the mechanical response of the paste [13]. In coming sections first, the pore size distribution including differences between binders is discussed. Subsequently, the influence of gel characteristics on drying shrinkage are taken into account.

Pore size distribution and drying shrinkage

In context to te pore size distribution and its relation to drying shrinkage, an overview of the considered pore classification is presented in Table 2.1 [54]. Where capillary pores consist of both macropores and medium capillaries, and gel pores comprise of small isolated capillaries, micropores and interlayer spaces.

Table 2.1: Classification of pore sizes in AAMs according to Mindess *et al.* [54]

Designation	Diameter	Description
Capillary pores	10.000 - 50 nm	Macropores
	50 - 10 nm	Medium capillaries
Gel pores	10 - 2.5 nm	Small isolated capillaries
	2.5 - 0.5 nm	Micropores
	$\leq$ 0.5 nm	Interlayer spaces

PC consists mainly of capillary pores, unlike AAMs which contain a higher volume of medium and small isolated capillaries, particularly in slag systems. Past research on both GGBFS and FA paste systems observed that this increased volume of medium and small isolated capillaries, also referred to as mesopores in the literature, contributes to a refined pore structure. This refined pore structure is one of the main factors responsible for the enhanced drying shrinkage strain observed in AAMs [17, 19]. The sizes of developed pores are dependent on the type and quantity of raw materials in AAMs. Consequently, the aforementioned binder systems are discussed separately.

High-calcium based binders

The research conducted by Collins *et al.* showed that alkali-activated slag (AAS) pastes have a higher proportion of pore sizes within the mesopore region (82%) and a lower amount of macropores compared to PC pastes (36.4% in mesopore region), the result is also shown in Figures 2.8 and 2.9 [19]. Because of this difference, the meniscus reaches such pores more quickly, resulting in elevated capillary pressure. Moreover, the smaller size and consequently reduced volume of mesopores in alkali-activated slag systems contribute to the lower overall weight loss, as demonstrated in Figure 1.1. This observation further supports the theory that capillary pressure, occurring during the drying process, significantly influences the drying shrinkage of alkali-activated slag pastes [19].

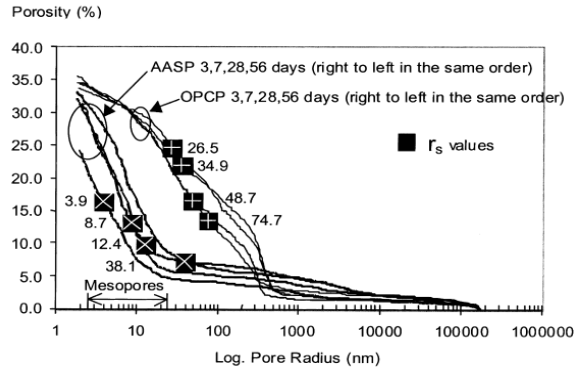

Figure 2.8: Cummulative pore size distribution of PC and AAS for 3, 7 28 and 56 days [19]

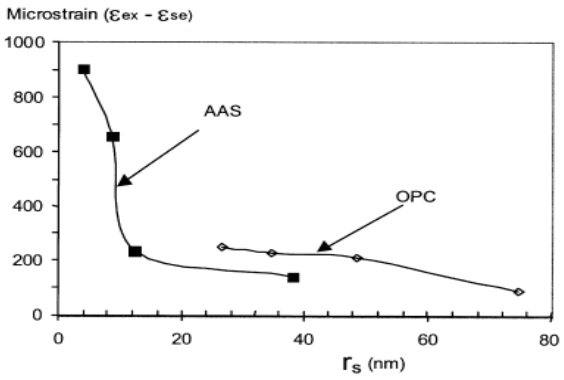

Figure 2.9: Drying shrinkage vs pore radius for AAS and PC, with w/b = 0.5 [19]

In conclusion, the presence of mesopores within a specific range significantly contributes to the elevated drying shrinkage observed in alkali-activated slag systems, primarily due to their susceptibility to water loss [11, 14, 18, 22]. The different pore size distribution and properties of the pore solution result in reduced degrees of saturation and stiffness, consequently leading to increased drying shrinkage [50]. Therefore, it is important to consider the pore radius at which the meniscus forms, rather than only focusing on water loss, when evaluating the drying shrinkage behaviour.

Low-calcium based binders
Low-calcium binders contain higher volume of medium capillaries and have a wider range compared to high-calcium binders [11, 22]. However, its distribution is in general finer than PC binders. The total porosity of alkali-activated fly ash binders is higher than alkali-activated slag binders, resulting an larger surface area available to evaporate of water, so the total water loss increases [11, 53]. However, in other studies it was found that binders of fly ash exhibit lower drying shrinkage strains, dependent on the curing conditions [55].

The higher porosity is causing a lower density of the binder [40]. Moreover, it is documented that instead of large capillary pores, large cavities are detected in the microstructure [56]. The pore structure and its pore size distribution is affected by properties and proportions of raw materials, alkali and silica content [40, 56].

Blended binders
Consistent with previous research (see section 2.1.4), C-A-S-H gels have been recognized for their superior space-filling effect compared to N-A-S-H gels, resulting in a denser pore structure with reduced pore size distribution and overall porosity [44, 57]. This transition towards greater densification can also be observed in Figure 2.10, where an increase in slag content leads to an denser pore structure [53, 58].

The study conducted by Wang *et al.* examined the pore size distribution, drying shrinkage behaviour and weight loss of alkali-activated blended system with varying proportions of fly ash and slag [53]. The findings of this study revealed that samples containing 30-50% fly ash exhibited the lowest rates of drying shrinkage, correlated with a denser pore structure, as illustrated in Figures 2.10 and 2.11. Additionally, specimens with higher slag content showed lower reduced weight loss during the drying process [53]. It is important to note that these results do not clearly establish a direct relationship between lower water loss and reduced drying shrinkage. This phenomenon may also be attributed to the finer pore structure that arises from increased slag incorporation [16, 19].

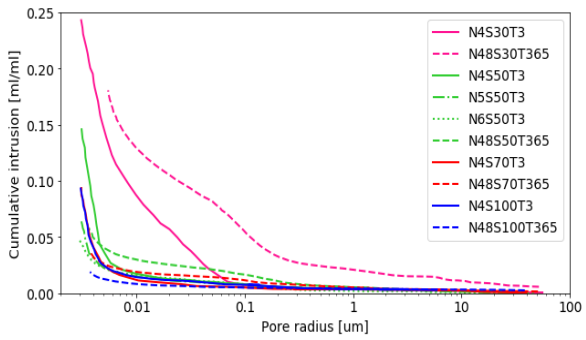

Figure 2.10: The effect of different FA/GGBFS ratios on cumulative pore size distribution at 3 and 365 days. N: wt.% Na_2O activator content; S: proportion of slag; T: curing time in days. Data from [53, 58]

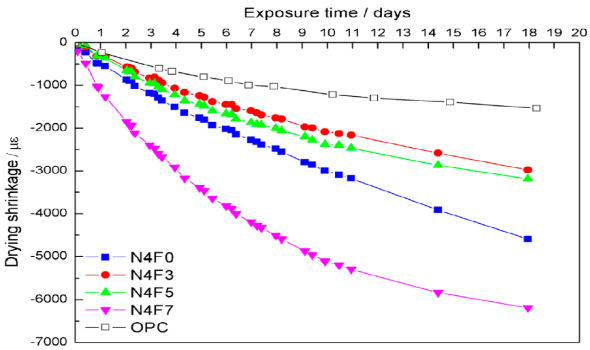

Figure 2.11: The effect of amount of fly ash on the drying shrinkage behaviour of alkali-activated blended binders after 3 days, w/b = 0.35, N4: 4 wt.% Na_2O content in the activator; F0-F7: 0-70% fly ash replacement of slag F[53]

Based on the findings discussed above, it can be concluded that the pore structure of AAMs is influenced by the type of precursors chosen for the mix design. Specifically, samples with lower fly ash content exhibited a denser pore structure. This observation suggests that the proportion of fly ash plays a crucial role in determining the pore size distribution.

Influence of gel characteristics on drying shrinkage
In addition to the pore structure, other factors such as the type and structure of the gels formed are known to significantly impact the drying shrinkage of AAMs [14, 19, 53]. As shown in Figure 2.4, the stability of N-A-S-H gel itself is mainly influenced by the calcium concentration and pH, of which the former has the most impact [18, 36]. This section focuses on the dimensional stability of the reaction products related to drying shrinkage.

AAMs have lower elastic stiffness compared to traditional PC, according to past research this contributes to the increased magnitude of drying shrinkage [14]. The formation of diverse binder systems, influenced by the choice of precursor and/or activator type and concentration, leads to microstructural changes, which become a significant factor influencing drying shrinkage, as discussed in [53].

High-calcium based binders
According to Ye *et al.*, the drying shrinkage mechanism and corresponding viscous performance is highly dependent on the RH. The driving force is the rearrangement and reorganisation of C-A-S-H gel particles under the present capillary stress, therefore, the viscous characteristic is not due to the loss of moisture but due to this micro-structural re-arrangement. For this reason, most shrinkage of AAS dried at high RH is irreversible, because the organized structure is changed permanent [20].

Depending on the type and concentration of activator C-A-S-H gel is formed, affecting the magnitude of drying shrinkage. For example, more drying shrinkage is observed when waterglass is used, as more silica-rich gel is formed resulting in more contraction when it loses moisture [16, 31]. This contraction does not take place when sodium hydroxide is used. The stiffness of the matrix is also affected by the activator, research of Cartwright *et al.* observed 33% lower elastic modulus using sodium hydroxide instead of waterglass [14].

The magnitude of drying shrinkage of AAS can be reduced through various adjustments, examples are decreasing the modulus of activator (M_s) and slag fineness, or by increasing the aggregate to slag ratio [31].

Low-calcium based binders
As mentioned before, in low-calcium binders water molecules are not chemically bound and therefore prone to evaporation [18]. Research of Ma *et al.* showed that most of the water is free water, which can be found in the aluminosilicate gel pores and voids left by dissolved FA particles [17]. The results regarding drying shrinkage and moisture loss demonstrate that the mechanism is affected by the microstructure of the binder, as the drying shrinkage increases while the quantity of water lost decreases [17].

The drying shrinkage strain of AAFA is smaller compared to AAS, according to literature, this difference can be explained by the higher porosity and difference in gel composition and its relation to drying shrinkage [11, 18]. Moreover, the behaviour of interlayers on nanoscale upon drying are not investigated and therefore unclear, in contrast to high-calcium binders.

N-A-S-H gel evolves into higher strength matrices as it gets silicon-richer by changes in reaction time and curing temperature [7]. Curing at high RH (over 90%) results in a dense, compact material, in contrast when it is cured at low RH, as this results in a porous and granular material [37]. The stiffness of N-A-S-H matrices is weakened when increasing the curing temperature, as the connectivity and chemical bond stability is lowered [59]. For the micro-structural development the curing conditions are therefore of greatest importance.

Blended binders
Blended binders exhibit drying shrinkage levels that are higher than those of PC but generally smaller than pure AAS or AAFA binders [53]. The addition of FA to slag can significantly mitigate the drying shrinkage of samples [15]. The mechanism governing drying shrinkage in blended binders is more complex, as it is influenced by the properties and proportions of the raw materials used, which in turn affect the composition of the gel [40]. Both the stability of N-A-S-H gel and the drying shrinkage of blended binders are greatly influenced by the calcium content [18]. Increasing the proportions of C-(N)-A-S-H gel leads to an increase in both the rate and magnitude of drying shrinkage. On the other hand, this increase in gel composition also enhances the mechanical properties of the binder, improving its stiffness and strength. In other words, the shrinkage phenomenon in the mixed binder is influenced by a competing mechanism between the particle size distribution and stiffness [40].

2.2.5. Factors affecting drying shrinkage in alkali-activated materials

The drying shrinkage mechanism in AAMs is intricately influenced by pore size distribution and gel characteristics, as described in the previous section. These fundamental parameters are, in turn, subject to the impact of mix design choices and curing conditions. Therefore, those factor are examined in this section. Initially, common influencing factors, also known from PC, are described. Following this, the state-of-the-art influencing factors specific to AAMs are considered.

Common influencing factors of drying shrinkage

The common influencing factors considered are water-to-binder-ratio and general curing conditions.

Water-to-binder ratio

As drying shrinkage is caused by the evaporation of unbound water, the amount of water available in the paste is of importance. Therefore, higher water-to-cement ratios in conventional concrete provides more water available that can evaporate, contributing to higher drying shrinkage. In AAMs, the water-to-binder ratio is considered instead of the water-to-cement ratio. Similar to conventional concrete, higher water-to-binder ratios can result in higher drying shrinkage, as there is excessive water available in the matrix available for evaporation. It is important to note that a smaller water-to-binder ratio corresponds to minor drying shrinkage, but can result in more significant autogeneous shrinkage behaviour [60].

Curing time

Thomas *et al.* investigated the impact of an extended curing time (90 days) on the drying shrinkage strain in AAMs, suggesting that the elevated dimensional instability causing drying shrinkage is primarily attributed to delayed product formation and microstructural development [11]. Furthermore, autogenous shrinkage decreases with extended curing times, indicating that the duration of exposure to the environment directly has a direct impact to drying shrinkage [57].

Relative humidity

The external and internal relative humidity are factors influencing drying shrinkage in AAMs. The external RH refers to the moisture conditions in the surrounding environment where AAMs are placed, impacting the overall drying process. Generally, higher external RH results in lower the moisture evaporation from the surface, maintaining saturation and preventing drying. On the other hand, internal RH refers to the moisture content within the matrix, influenced by factors such as water-to-binder ratio and external RH. As discussed in section 2.2.2, the internal RH affects the external RH by driving the evaporation of free water.

The migration rate of water molecules in various pore sizes within AAMs is regulated by both internal and external RH. A decrease in external RH intensifies water loss in mesopores, potentially leading to higher pore pressure associated with drying shrinkage [40]. This finding aligns with the observations of Ye *et al.*, emphasizing that drying shrinkage is related to how water moves through the system rather than the quantity of water that is lost to the external environment, stating that drying shrinkage is governed by RH Ye *et al.* Moreover, the study suggested that the RH influence the hydration products by affecting the kinetics of shrinkage, as the pore size diameters are refined upon drying which process is magnified for RH $\geq$ 70% [50]. Additionally, research by Ye *et al.* and Criado *et al.* highlight the impact of different shrinkage conditions across various RH ranges and pore sizes, with low RH potentially contributing to the development of a loosely compacted structure with large pores [13, 37]. In addition, it is reported that the critical RH at which the capillary meniscus becomes unstable under equilibrium conditions is commonly considered to be 40% RH [50].

According to Marjanović *et al.*, drying shrinkage of alkali-activated slag-fly ash mortars can be reduced when curing at 95 °C for the first 24 hours, making it comparable with drying shrinkage of PC based mortar cured at room temperature [8]. Moist curing resulted in a reduction of drying shrinkage compared to curing to the air [48]. The effect of sealed curing to drying shrinkage is studied by Yong, it was shown that curing specimens for an extended period before testing results in a more mature binder, enhancing resistance to dimensional changes [12, 61]. The result is shown in Figure 2.12. With sealed curing, only autogenous shrinkage can occur as external water ingress or loss is prevented [11]. When samples are unsealed, both drying and autogenous shrinkage occur at the same time.

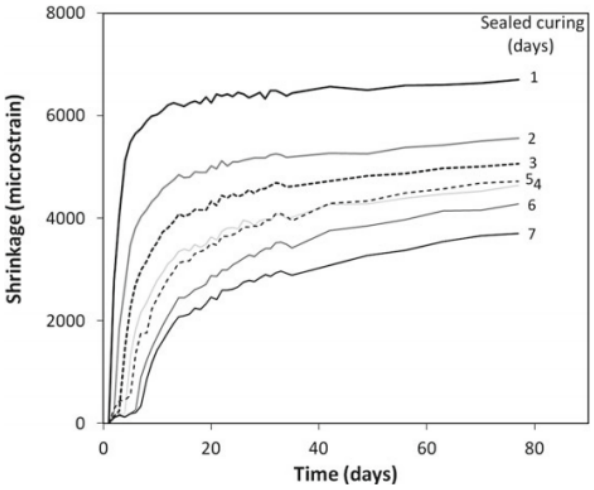

Figure 2.12: Effect of sealed curing on drying shrinkage of blended alkali-activated paste with 60% FA, 40% slag, M_s = 1.5 [61]

Temperature

In addition to relative humidity, curing temperature significantly affects drying shrinkage. A study conducted by Cai *et al.* observed an 80 % decrease in drying shrinkage caused by the effect of heat curing (60 °C). The key contributing factor is the occurrence of most autogenous shrinkage in the initial days due to the accelerated hydration process. As the measurements of drying shrinkage began, including autogenous shrinkage, the recorded autogenous shrinkage was lower than for samples cured at normal temperatures. Moreover, elevated temperatures led to accelerated hydration, resulting in more reaction products and a denser pore structure. Consequently, the smallest porosity was observed under these conditions [48].

The research of Ma *et al.* observed increased drying shrinkage in AAFA pastes compared to other studies, due to a lower curing temperature (40 °C instead of 80°C). It is suggested that the improved resistance to drying shrinkage is linked to the heightened resistance of the paste matrix, resulting from the formation of a denser structure at higher curing temperatures [17, 40].

The study of Marjanović *et al.* stated that the curing temperature mostly affects drying shrinkage behaviour of blended slag and fly ash AAMs. Curing at 95 °C for the first 24 hours significantly reduced the drying shrinkage [8]. The results are shown in Figure 2.13, where n represents the molar ratio of SiO_2/Na_2O and % Na_2O the percentage of Na_2O relative to the weight of precursor [8]. Furthermore, it was discovered that this drying shrinkage behaviour was nearly equivalent to that of the PC mortar cured at room temperature Marjanović *et al.*

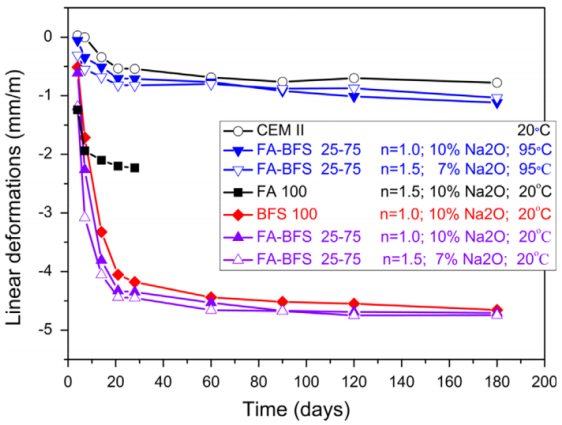

Figure 2.13: Drying shrinkage strain of blended AAMs influenced by both curing time and alkali activation conditions. n: molar ratio of SiO_2/Na_2O [8]

Distinctive factors shaping drying shrinkage in AAMs

Activator type

The choice of activator in alkali-activated materials plays an essential role in shaping both mechanical properties and microstructure, thus influencing the overall shrinkage behavior [13]. In general, alkaline activators such as sodium hydroxide (NaOH), waterglass (sodium silicate, Na_2SiO_3), and sodium carbonate (Na_2CO_3) are commonly used, with the combination of NaOH and waterglass being the most common [18].

The microstructure formation is highly dependent on the activator type, and this dependency extends to its impact on shrinkage behavior. Previous research indicates that comparable cement shrinkage strains are observed when sodium hydroxide and sodium carbonate solutions are used, contrasting with waterglass solutions, which result in larger drying shrinkage strains [31, 40, 62]. Moreover, a higher sodium silicate content leads to the formation of more silica-rich gel, which is more susceptible to drying due to its higher water content, contracting as water is lost [31].

Ma investigated the microstructure formation of alkali-activated fly ash paste, as depicted in Figures 2.14 and 2.15 [63]. In sodium hydroxide-activated fly ash paste, reaction products primarily develop on the surface of fly ash grains, resulting in a relatively loose microstructure. Conversely, sodium silicate-activated fly ash paste exhibits uniformly dispersed reaction products throughout the matrix, leading to a denser microstructure. Additionally, sodium hydroxide raises the pH of the activating solution, enhancing fly ash dissolution and contributing to the formation of a finer pore structure [17].

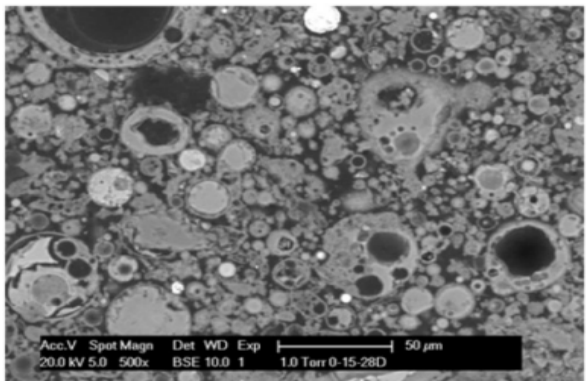

Figure 2.14: Microstructure of fly ash paste activated with sodium hydroxide after 28 days cured at 40°C (from [63])

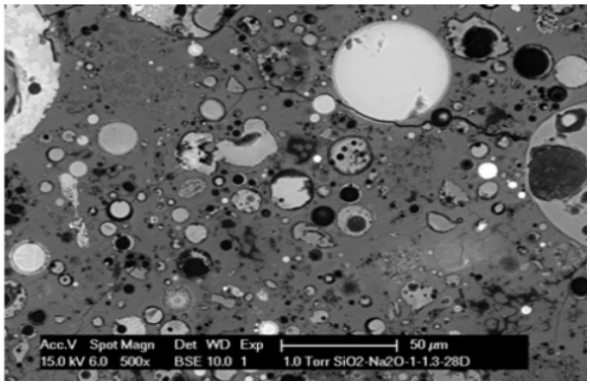

Figure 2.15: Microstructure of fly ash paste activated with sodium silicate after 28 days cured at 40°C (from [63])

Similarly, Aydin *et al.* observed a comparable distinction in alkali-activated slag pastes, highlighting that waterglass-activated slag displays a dense and compact structure compared to NaOH-activated slag [64]. This results in higher compressive strength and more pronounced drying shrinkage for waterglass-activated slag [64]. Moreover, Cartwright *et al.* found that alkali-activated slag mortars activated solely with NaOH exhibited a 33% lower elastic modulus compared to PC mortar, whereas mortars activated with water glass showed a similar elastic modulus to PC [14].

The above-mentioned points highlight the significant influence of activators on the mechanical properties and shrinkage characteristics of alkali-activated materials.

Activator modulus

The activator modulus (M_s), representing the molar ratio of SiO_2 to Na_2O, is influenced by the choice and concentration of the activator. It is important to note that AAMs activated with waterglass exhibit higher drying shrinkage, a tendency which is intensified when the activator modulus increases.

A study by Ma *et al.* investigated the impact of different activator moduli (ranging from 1 to 0.67) on drying shrinkage behaviour and corresponding pore size distribution of AAFA. The reduction of the activator modulus resulted in a decrease in drying shrinkage and a coarsening of the pore structure [17].

This finding aligns with the observations of Gao *et al.*, who suggested that decreasing the additional silicate content from the activator could also lead to a certain extent of decrease in drying shrinkage [15]. Additionally, the influence on the porosity of different moduli and slag-to-fly-ash-ratios was considered, where the mixtures with lower slag content exhibit higher porosity, and this porosity decreases with increasing activator modulus, as shown in Figure 2.16 [15].

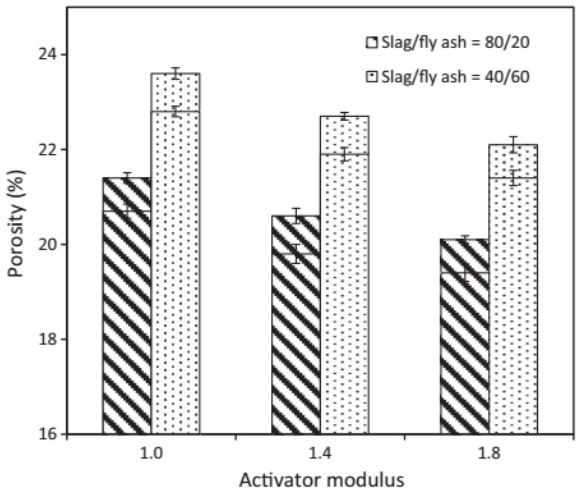

Figure 2.16: 7 and 28 days porosity of alkali-activated slag-fly ash mortars with M_s equal to 1, 1.4 and 1.8 by [15]

In the investigation of Aydin *et al.*, the influence of the activator modulus was explored among other factors. Figure 2.17 illustrates the differences observed in slag mortars with M_s equal to 0, 0.4 and 1.2 [64]. A more refined pore size distribution is evident when silicate is present in the system, with the amount of mesopores for M_s of 1.2 approximately twice as large compared to M_s equal to 0.4. Mortars with no silicate present (M_s = 0) exhibit a coarser pore size distribution with more macropores and mesopores, indicating a poorly packed and porous structure. Additionally, a distinct microstructure was identified in the same study, suggesting a correlation with different drying shrinkage strains; lower drying shrinkage strains were observed for mortars with no silicate present [64].

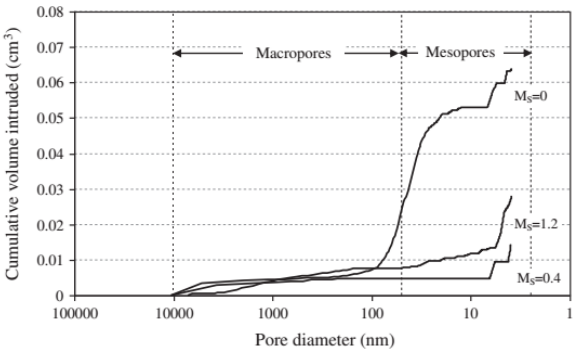

Figure 2.17: Pore size distribution of mortars with M_s equal to 0, 0.4 and 1.2 [64]

Activator concentration

In this section, the influence of alkali content on the microstructure of AAMs is considered. A higher concentration of alkali in the activators leads to an increased degree of chemical reactions during the hydration process. This heightened reactivity results in the formation of more complete hydration products, which, in turn, limits the availability of free water for evaporation. Additionally, the increased hydration and geopolymerization is associated with the creation of smaller pores in the microstructure of the material [11, 40]. Consequently, the overall porosity is reduced, causing a notable shift in the pore size distribution. Past research documented this densification is considered to be the reason why drying shrinkage of high calcium AAMs (so also blended slag and FA) increases along with the alkali

content [31, 40]. Research of Jin *et al.* noted that the drying shrinkage increases with higher dosage of activators, as well as slag fineness [10]. It is worth noting that in the literature, the interplay between activator concentration and modulus is often considered simultaneously, acknowledging their collective impact on the reactivity and microstructure of alkali-activated materials.

A study of Aydin *et al.* demonstrated that decreasing both alkaline content and activator modulus can effectively mitigate autogeneous and drying shrinkage because of the reduced hydration reaction. It is suggested that this reduction is caused by a densified pore structure and therefore reduced porosity. An overview of this result is shown in Figure 2.18 [64].

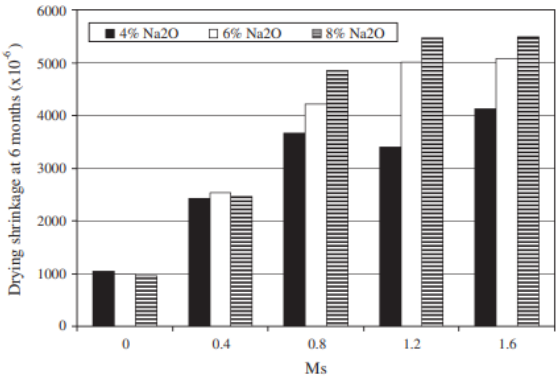

Figure 2.18: Effect of activator modulus and sodium oxide concentration on drying shrinkage at 6 months of AAS [64]

In the study of Thomas *et al.*, it was reported that an increase of sodium oxide concentration from 4 to 6 % resulted in a reduction of the shrinkage [11], the results are shown in Chapter 1, Figures 1.1 and 1.2. For AAFA, it was suggested that an increase of Na_2O concentration resulted in reduced shrinkage due to reduced porosity and improved stiffness and strength. For AAS, both higher activator content and a higher activator modulus resulted in increased shrinkage as well as strength, possibly due to an increase in pore fineness and lower porosity. It is also noted that this affects the sensitivity to water loss [11].

In the research of Melo Neto *et al.*, the effect of the activator concentration on both drying and autogeneous shrinkage in alkali-activated slag was investigated, with activator modulus at 1.7, with 2.5 and 4.5% of Na_2O (see Figures 2.19 and 2.20). This study also showed that the quantity of silicate within the activator significantly impacts both autogeneous and drying shrinkage. Higher levels of sodium silicate lead to a rise in overall shrinkage. Consequently, an increase in sodium silicate content is associated with a reduction in total porosity and meso-pores volume, which directly elevating the activator modulus quantity triggers greater hydration, thereby boosting C–S–H volume and reducing porosity. Moreover, it was found that the mesopore volume decreased, which, in turn, has a direct impact on shrinkage attributed to self-desiccation [16, 18].

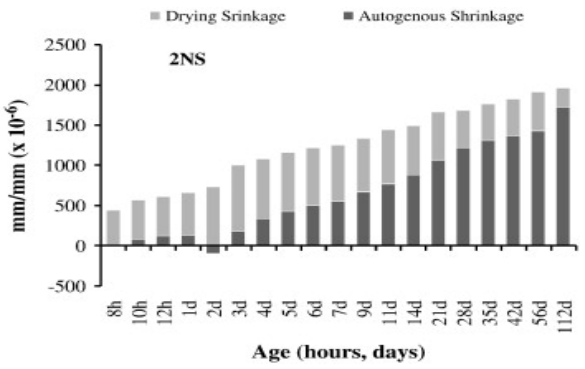

Figure 2.19: Drying and autogeneous shrinkage of 2.5% Na_2O mortars [16]

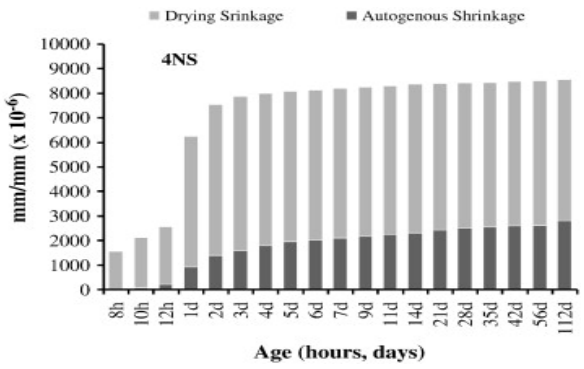

Figure 2.20: Drying and autogeneous shrinkage of 4.5% Na_2O mortars [16]

Available calcium content in the matrix
In addition to its notable impact on the stability of the NASH gel (discussed in Section 2.1.4), the available calcium content in the matrix plays a crucial role in influencing the drying shrinkage behavior of alkali-activated materials. As discussed in Section 2.2.4, high-calcium based systems result in a finer pore structure and low-calcium systems lead to coarser pore structures.

AAS pastes have a lower Ca/Si ratio in the hydration products of C-S-H gels (Ca/Si = 1.1) compared to PC pastes (Ca/Si = 2.0) [38]. The drying shrinkage of the pastes is observed to occur more prominently in C-S-H gels with a low Ca/Si ratio, as highlighted by Zhang *et al.* [38]. Mastali *et al.* also emphasizes the significant influence of the molar ratio of Ca/Si on the rate of drying shrinkage in AAMs. It is suggested that a higher Ca/Si ratio contributes to the formation of a fine pore structure, impacting tensile stresses in capillary pores, as well as strength and elastic modulus [18].

Gao *et al.* suggests that the C-A-S-H gels with low Ca/Si ratio display a natural tendency for shrinkage, and modifying this property can be achieved through methods such as incorporating fly ash into slag or reducing the silicate content from the activator [15]. The review of Huang *et al.* discusses the competition mechanism between slag and class F fly ash, highlighting that the CaO content of raw materials does not exhibit a monotonic relationship with the drying shrinkage of alkali-activated materials. The pore size distribution of the blended AAMs are identified as determinants of drying shrinkage [40].

2.3. Knowledge gaps in drying shrinkage mechanism research

Existing research on drying shrinkage in alkali-activated materials reveals several critical knowledge gaps that need attention for a more comprehensive understanding.

1. **Unclear governing mechanism**
   Uncertainty persists about the primary governing factor initiating the drying shrinkage process. While studies point to differences in gel composition and pore size distribution, a clear understanding of the triggering mechanism is still ambiguous.
2. **Autogenous shrinkage and external drying shrinkage**
   Existing literature predominantly concentrates on drying shrinkage, including the autogenous drying shrinkage part. This discrepancy hinders an understanding of the external drying shrinkage mechanism.
3. **Insufficiency in comprehensive shrinkage data**
   Current studies lack comprehensive shrinkage data where multiple parameters are held constant. A focused examination of specific influential factors under consistent conditions is needed to uncover nuanced insights into their isolated effects.

3

Approach & Methodology

To advance the understanding of the drying shrinkage mechanism in AAMs, this study aims to identify whether the pore structure or gel characteristics explain the mechanism. To achieve this, it is essential to control one characteristic while varying the other. Therefore, the pore size distribution is controlled, offering the opportunity to quantify the effect of gel composition on drying shrinkage. This chapter presents the strategy and defined design parameters applied in this study. Subsequently, information about materials, mix design and corresponding sample preparation is provided. In addition, the experimental methods are described. Finally, the applied selection method for samples is outlined, considering the same pore size distribution.

3.1. Strategy

This thesis is divided into two main parts, each focusing on distinct objectives of the research:

Part 1: Influence of mixture design parameters on properties and microstructure
In the first part, the focus is on understanding the impact of mixture design parameters on properties and microstructure characteristics of alkali-activated binders. The investigation delves into how variations in slag-to-fly-ash ratios, curing time and activator content affect the drying shrinkage, weight loss, mechanical properties and pore size distribution. This provides a comprehensive perspective on how these mixture design parameters interact with and influence the properties and microstructure of alkali-activated materials.

Part 2: Correlation of pore and gel characteristics on drying shrinkage
The second part is dedicated to advancing the understanding of the drying shrinkage mechanism, Here, the emphasis lies on controlling pore size distribution and investigating the most susceptible main hydration product concerning drying shrinkage. Initially, pore size distributions of different mixture designs are compared. When these distributions fall within a similar range, the study proceeds to compare the drying shrinkage behavior, weight loss, flexural, and compressive strength. Additionally, variations between the volume of reaction products and the chemical composition are considered. This approach offers an opportunity to quantify the effect of gel composition on drying shrinkage in alkali-activated materials.

3.2. Design parameters

To control the pore size distribution and ensure variety in the reaction products, various slag-to-fly-ash ratios, curing times and Na_2O contents were investigated. The aim in all cases was to develop a microstructure as uniform as possible. Specific values for this study are provided below in Figure 3.1.

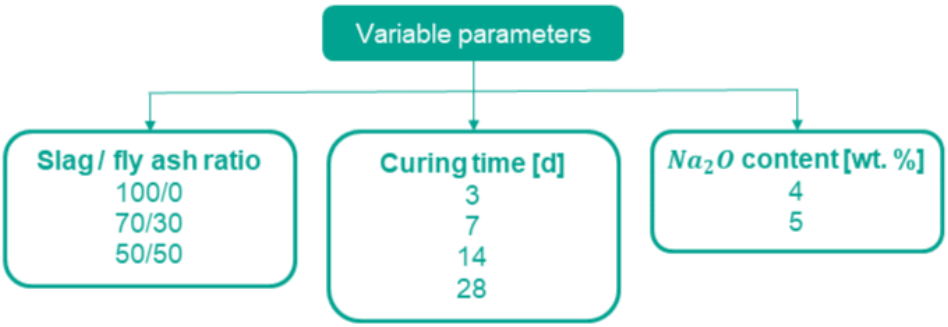

Figure 3.1: Variable mix design parameters

For the slag-to-fly-ash ratios, only ratios above 50% FA were considered. This decision was based on findings in the literature, which indicated that fly ash ratios below 50% resulted in coarsened pore size distributions that deviated too much from the range of pore size distributions of other ratios, as discussed in Section 2.2.4. Additionally, the aim was to achieve higher compressive strength, which are more likely to be used in the industry. This implied a preference for the presence of C-(N)-A-S-H gels in the microstructure.

Curing times of 3, 7, 14, and 28 days were selected, with longer curing times expected to result in a more refined pore size distribution, as discussed in Chapter 2. Longer curing times were also necessary for samples with higher fly ash content, given the slower hydration process of fly ash.

In addition, a sodium oxide content of 4 and 5 percent of the weight of precursor was chosen, with a higher content providing a more refined pore structure [11]. Combining longer curing times with increasing amounts of fly ash aimed to achieve a pore structure within the same range as a sample with lower fly ash content and shorter curing time. To increase the probability uniform pore size distribution within the mix designs, the sodium oxide content was added as a parameter.

3.3. Materials and sample preparation

This section includes information about the GGBFS, FA and alkaline activator used in this study. Moreover, the mix designs, the mixing procedure and sample preparation are outlined.

3.3.1. Blast furnace slag and fly ash

The study incorporated Ground Granulated Blast Furnace Slag from Ecocem Benelux B.V. and Fly Ash class F from Vliegasunie B.V.. The chemical composition determined by X-ray fluorescencse (XRF) is given in Table 3.1 [65].

Table 3.1: Chemical composition of GGBFS and FA measured with XRF [wt.%] (data from [65]).

	SiO_2	CaO	Al_2O_3	Fe_2O_3	Na_2O	K_2O	MgO	SO_3	P_2O_5	TiO_2	Others
GGBFS	34.99	36.33	14.32	0.4	0.24	0.46	9.42	1.36	0.01	1.21	1.26
FA	55.29	4.43	25.03	6.94	0.91	1.66	1.41	0.73	1.01	1.23	1.36

3.3.2. Alkaline activator

For the alkaline activator, a mixture of waterglass solution, sodium hydroxide solution and deionized water was used to achieve the desired activator modulus M_s. The activator modulus is defined by the molar ratio of SiO_2 and Na_2O. The 50% sodium hydroxide solution in this study is from Brenntag, and the waterglass comes from PQ corporation, with SiO_2/Na_2O ratio of 2.0-2.1 and composition by weight

percent of 15% Na_2O, 30% SiO_2 and 55% H_2O. The activator was synthesized by mixing all ingredients approximately 5 to 6 hours. Subsequently, the activator was kept in the laboratory to cool down for at least 24 hours before use.

3.3.3. Mix design

A water-to-precursor ratio (w/p) of 0.4 and M_s of 1.0 were maintained for all specimens. Table 3.2 shows all mix designs with their corresponding labels. The labels used in this study were structured as S[x]N[y]T[z], where S represents the percentage of GGBFS, N the sodium oxide content with respect to the weight of precursor and T the curing time in days.

Table 3.2: Mix designs of all samples.

Label	GGBFS [wt.%]	FA [wt.%]	Na_2O[wt.%]	Curing time [d]
S50N4T3	50	50	4	3
S50N4T7	50	50	4	7
S50N4T14	50	50	4	14
S50N4T28	50	50	4	28
S70N4T3	70	30	4	3
S70N4T7	70	30	4	7
S70N4T14	70	30	4	14
S70N4T28	70	30	4	28
S100N4T3	100	0	4	3
S100N4T7	100	0	4	7
S100N4T14	100	0	4	14
S100N4T28	100	0	4	28
S70N5T3	70	30	5	3
S70N5T7	70	30	5	7
S70N5T14	70	30	5	14
S70N5T28	70	30	5	28
S50N5T3	50	50	5	3
S50N5T7	50	50	5	7
S50N5T14	50	50	5	14
S50N5T28	50	50	5	28

3.3.4. Mixing procedure

1. The accurate amount of precursor (GGBFS and/or FA) was weighed out and placed into the mixing bowl of the Hobart mixing machine.
2. The precursors were dry-mixed for 2 minutes.
3. The activator was slowly added while the mixing machine was on the lowest speed, and then mixed for 1 minute.
4. The mixer was stopped, and the paste was scraped to ensure everything could be mixed thoroughly.
5. The mixing machine ran for 1 more minute at high speed.
6. The paste was poured into relevant moulds and sealed to prevent moisture loss.

3.3.5. Sample preparation for drying shrinkage and mechanical properties

For measurements of drying shrinkage and mechanical properties, three prisms with dimensions of 40x40x160 mm were prepared for all mix designs in Table 3.2. The prisms were demoulded and resealed with foil to prevent moisture loss 24 hours after casting (Figure 3.2), and placed in the standard curing room at 20 °C and 95% RH. They remained in the curing room until the indicated curing time per mix design was reached and the specified test could be performed.

Figure 3.2: Storage of resealed prisms in standard curing room

3.3.6. Sample preparation for MIP and SEM-EDX

Cylinders with 25 mm diameter and height of 40 mm were used as molds for micro-analysis samples. These containers were sealed using paraffin foil and the lid (see Figure 3.3). They were then immediately placed in the standard curing room to control the temperature. When the indicated curing time for a mix design was reached, the samples were broken into pieces with a hammer and chisel (Figure 3.4). The crushed samples were placed in a new, clean container, discarding the pieces that had been in contact with the small casting container. The hydration process was then stopped by immersing the broken particles in isopropanol for 7 days, with the isopropanol being refreshed once after the first 24 hours. After 7 days, the crushed particles were placed in a vacuum freeze-dryer for a minimum of 21 days to ensure the complete removal of all liquid from the paste. For MIP, the samples were now ready to use.

Preparing samples for SEM-EDX analysis required some additional steps. First, the samples were impregnated with epoxy and subsequently ground from grain size 220 to 800. To ensure that the epoxy reached all the pores, a second layer of epoxy was applied, which was then ground and polished. The grinding steps performed include grain sizes 320 - 800 - 1200 - 2000 - 4000, the polishing started at 9 μm to respectively 3 - 1 - 0.25 μm. Each polishing step was performed for 4 minutes. The result of this grinding and polishing of one sample is shown in Figure 3.5.

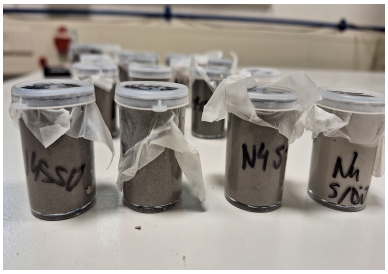

Figure 3.3: Samples for micro-structural analysis

Figure 3.4: Crushed samples for micro-analysis

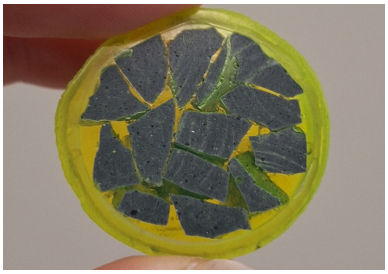

Figure 3.5: Polished S70N4T14 sample ready for analysis

3.4. Test methods

The description of tests methods are presented in the following section.

3.4.1. Mechanical tests

A three-point bending test was executed on three specimens selected from each mix. These tests were conducted according to NEN-EN 196-1, utilizing a hydraulic testing machine with a consistent loading rate of 0.1 kN/s, a start load of 0.1 kN and stop load of 20% [66]. The specimens were positioned

and loaded at their mid-span. The specimens 50% slag with 4 wt.% Na_2O after 28 days of curing after performing the flexural tests are shown in Figure 3.6.

Subsequent to the flexural tests, the resulting halves of the prisms were subjected to a compressive strength test, with a loading rate of 2.4 kN/sec, start load of 1 kN and stop load of 20%, following standard NEN-EN 196-1 [66]. For all measurements collected during the experiments, the average of the maximum strengths were used to calculate both the flexural and compressive strengths.

3.4.2. Drying shrinkage test

For the measurement of drying shrinkage, it is possible to examine two conditions: restrained and unrestrained conditions. In this study, the unrestrained shrinkage was determined. Under these conditions, samples are free to deform in length. The measurement of drying shrinkage started when the specified curing time of the samples were reached and the seal was removed. The drying shrinkage behaviour was measured for a time span of 28 days, throughout this time the samples were stored in a climate chamber with 20 °C and 55% RH. Three specimens were measured in parallel for each mix design.

The change in length of the samples were measured using a digital length comparator, with measuring accuracy of 0.001 mm (see Figure 3.7). The initial length is assumed to be the original length (160 mm) minus the first measurement with the comparator. The linear drying shrinkage is calculated using formula 3.1.

$$\epsilon_L = \frac{L_t - L_0}{L_0} \tag{3.1}$$

With:
L_t = the length at time t [mm]
L_0 = initial length, 160 - first measurement [mm] .

Figure 3.6: Samples of S50N4T28 after performing the flexural test

Figure 3.7: Digital length comparator to measure the variation in length

3.4.3. Weight loss

In addition to the length, the weight is measured in order to calculate the moisture loss of the samples with equation 3.2. The initial weight m_0 is assumed to be the weight after the specified curing time was reached. Each time a shrinkage measurement was performed, the weight was also measured by a balance with an accuracy of 0.1 g.

$$\Delta_m = \frac{m_0 - m_t}{m_0} \times 100\% \tag{3.2}$$

With:
m_t = the mass at time t [g]
m_o = initial weight [g].

3.4.4. Autogenous shrinkage test

To distinguish the autogenous shrinkage component in the conducted drying shrinkage measurements, autogeneous shrinkage was measured by using the corrugated tube method per ASTM 1698-09 [52]. The N4 mixtures were measured over 28 days. For 100% slag, two tubes were measured, while only one tube was used for 70% and 50% due to a limited quantity of LDTV's available.

The final setting time for each mix design was needed for calculating the autogeneous shrinkage strain. The Vicat needle test, conducted in accordance with NEN-EN 196-3, was employed to determine the final setting time [67]. Three measurements were taken for all N4 mix designs to ensure consistency.

Figure 3.8: Autogenous shrinkage measurement set up

3.4.5. Mercury intrusion porosimetry

Mercury intrusion porosimetry (MIP) was used to measure and identify the pore size distribution and the corresponding total porosity of AAMs. In this method, mercury was forced into the pores of the sample by applying two cycles of pressure. The measurements consisted of two distinct phases: an initial stage involving low pressure conditions (0 - 0.0036 MPa), followed by a subsequent high-pressure phase (0.0036 - 210 MPa). The cumulative intrusion of mercury at the maximum pressure allowed the determination of the total porosity. The contact angle and surface tension values used in this study was 141° and 0.485 N/m. The pore diameter ranging from 0.007 μm to 401.874 μm was detected.

MIP utilizes Washburn's equation to establish a connection between pressure required for mercury intrusion and the pore radius. This equation enables the determination of pore size distribution and other pore-related properties of porous materials.

$$D = \frac{-4\gamma cos(\theta)}{P} \tag{3.3}$$

With:
D = pore diameter [μm]
γ = surface tension of mercury [N/m]
θ = contact angle of the mercury and the AAMs[°]
P = applied pressure [MPa]

The test method has limitations, with the ink-bottle effect and possible damage during sample preparation being the most frequently mentioned issues in the literature [17]. However, it remains a relatively fast method for identifying the pore structure in the mesopore region.

3.4.6. SEM-EDX

The Scanning Electron Microscope (SEM) was employed to examine the hydration products, with a specific focus on the gel phases. The chemical composition of the gel phase was investigated using

the Energy Dispersive X-ray Spectroscopy (EDX) detector integrated with the SEM. An accelerating voltage of 15 kV, a magnification of 1000 and a working distance of 10 mm were utilized in this analysis. The volume of reaction products was determined through analysis of 35 SEM images per sample, which were segmented using Ilastik, an interactive machine learning and segmentation toolkit.

For the assessment of the chemical composition, EDX point analysis was performed on selected samples, specifically targeting the gel phases. The point analysis was conducted at a magnification of 5000, maintaining an equal accelerating voltage and working distance. The image resolution for this analysis was set at 1024 by 682.

This comprehensive approach facilitated the determination of both the chemical composition of the gel phases and the degree of reaction, providing a detailed characterization of the nature of the reacted gel. This information is crucial for identifying the proportions of C-(N)-A-S-H and N-A-S-H gels within the gel phases.

3.5. Sample selection based on pore size distribution

The strategy for this study is outlined in paragraph 3.1 to achieve the defined aim and objectives. To determine whether pore structure or gel characteristics govern the drying shrinkage mechanism of AAMs, it is necessary to achieve uniform pore structures across different mix designs. This approach allows for investigating the influence of various gel characteristics on drying shrinkage, given the established uniformity in pore structure at the time of exposure. Hence, controlling the pore size distribution becomes a crucial element in examining the drying shrinkage mechanism. As discussed in the literature review in Section 2.2.4 (Table 2.1), medium capillaries (0.01 - 0.05 μm) and small isolated capillaries (0.0025 - 0.01 μm) are predominantly present and therefore most important for AAMs. To address this, an iterative method is devised for sample selection based on the pore size distribution using both quantitative and qualitative approaches, involving the following steps:

1. **Visual inspection:**
   Visual inspection served as an initial screening method, to quickly assess the samples before continuing with the area under the curve analysis. This preliminary step not only facilitated a quick evaluation of the samples but also allowed for a qualitative assessment, contributing to a more comprehensive understanding of the detailed characteristics within the samples.
2. **Area under the curve analysis:**
   The area under the curve calculation is used as a second step to determine if equal pore structure is present between the mix designs. The trapezoidal rule is used to calculate the area under the curve (AUC) to analyse the selected samples qualitatively. It is method for numerical integration, where the trapezoidal rule is used to find the value of the definite integral, using equation 3.4

$$AUC = \int_a^b f(x)dx \tag{3.4}$$

   The calculation is performed for medium and small isolated capillaries separately.
3. **Selection of samples:**
   Based on step 1 and 2, samples were selected with an emphasis on achieving an uniform pore size distribution among different mix designs.
4. **Subtraction of the area under the curve for medium and small isolated capillaries:**
   This step was included to refine the selection process and focus on these important regions.

The criterion for selection was set such that the difference in the area under the curve for selected samples should be below 3.5%.

4

Results

This chapter presents the outcomes of the conducted experiments. First, the flexural and compressive strength results are shown. Subsequently, the autogenous shrinkage, drying shrinkage and corresponding weight loss results are presented. Next, the porosity and pore size distribution results from MIP experiments are shown. Finally, results from the sample selection based on the pore size distribution are provided, followed by two comparative studies between the selected samples to investigate the influence of different gel characteristics on the drying shrinkage mechanism.

4.1. Flexural and compressive strength results

Initially, the flexural and compressive strength results of the effect of different slag contents are given, followed by the influence of two activator contents on the strength. The values of the original data set are provided in Appendix A.1. For the compressive strength test, brittle failure of the samples was observed, of which pictures are shown in Figure B.1 of Appendix B.

4.1.1. The effect of slag content on flexural and compressive strength

Figure 4.1 illustrates the flexural strength results of mixtures with 100%, 70% and 50% GGBFS after 3, 7, 14 and 28 days of sealed curing. At each curing age, the S100N4 mixture demonstrates the highest flexural strength, followed by S70N4 and then S50N4. The results for S100N4 show a 26% increase in flexural strength from 3 to 28 days. In the case of the S70N4 mixture, a notable increase of 78% was observed, particularly between 3 and 7 days. Similarly, the S50N4 mixture showed a 57% increase in flexural strength from 3 to 28 days.

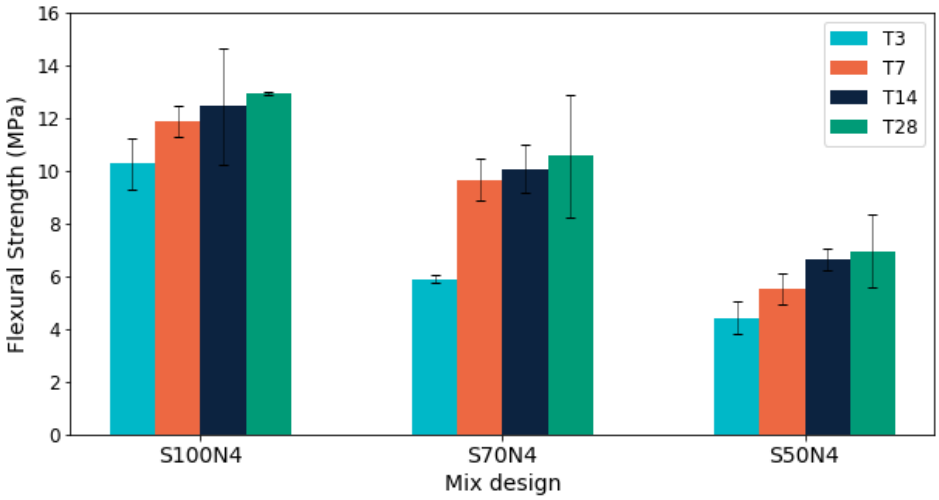

Figure 4.1: Flexural strength results of mixtures with 100%, 70% and 50% GGBFS and 4% Na_2O content after 3, 7, 14 and 28 days of curing

The compressive strength results for the aforementioned mixtures are presented in Figure 4.2. Over time, all mixtures show a continues increase in compressive strength. Specifically, for S100N4, S70N4 and S50N4, the strength increases by 45%, 34% and 80%, respectively, from 3 to 28 days. With the exception of the 7-day compressive strength, the S70N4 mixture exhibits the highest strength. Moreover, both S100N4 and S70N4 demonstrate an equivalent strength of 57.9 MPa after 28 curing days.

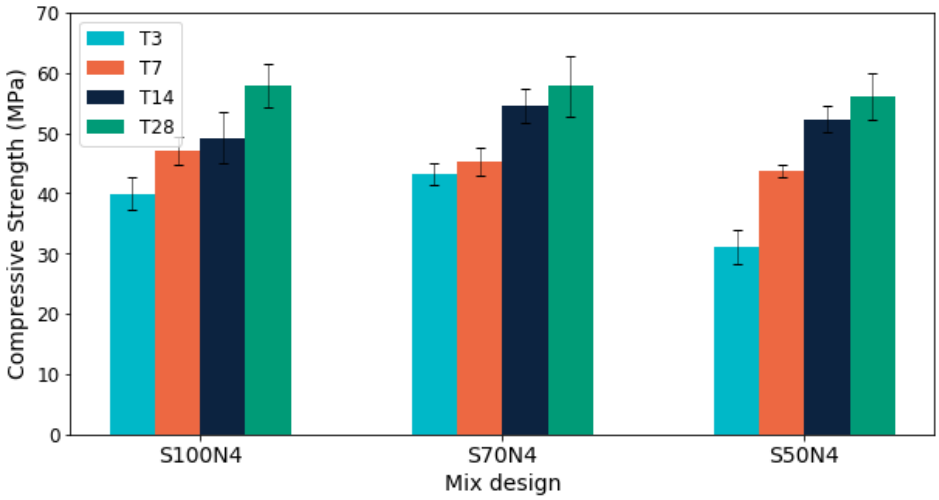

Figure 4.2: Compressive strength results of mixtures with 100%, 70% and 50% GGBFS and 4% Na_2O content after 3, 7, 14 and 28 days of curing

4.1.2. The effect of activator contents on flexural and compressive strength

Figure 4.3a shows the flexural strength results for S70 mixtures with 4 and 5 wt.% Na_2O content. A decrease in strength of 34%, 76% and 36% is observed for samples cured for 7, 14 and 28 days, respectively, when the activator content is increased from 4 to 5 wt.%. Conversely, for the 3-day strength, an increase in activator content resulted in a 12% rise in flexural strength. The compressive strength results, shown in Figure 4.3b, demonstrate a contrast to the flexural strength results. An increase of compressive strength is observed for mixtures with higher activator content for all curing ages. Specifically, for S70 mixtures, there are increases of 20% at 3 days, 30% at 7 days, 12% at 14 days and 15% at 28 days.

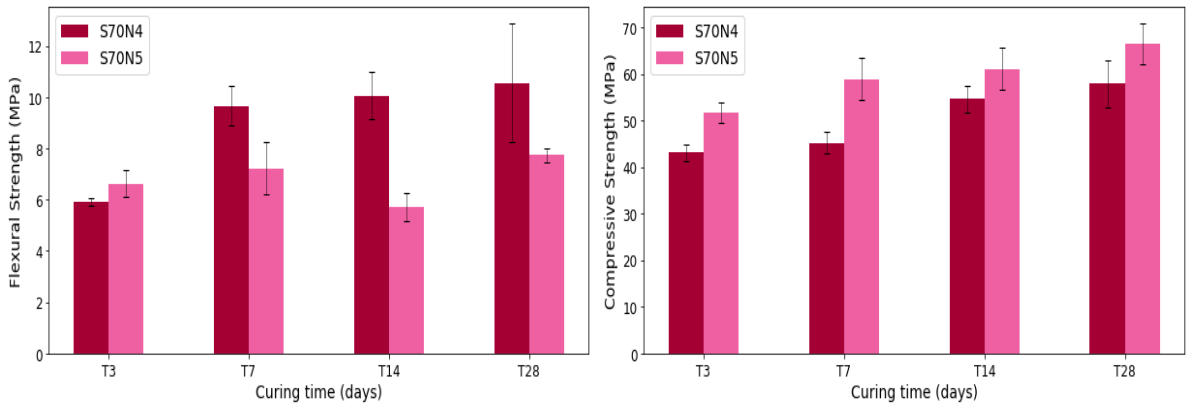

(a) Flexural strength

(b) Compressive strength

Figure 4.3: Flexural and compressive strength results of mixtures with 70% GGBFS, 4 and 5 wt.% Na_2O content after 3, 7, 14 and 28 days of curing

In Figure 4.4a, the flexural strength results are presented for S50 mixtures with 4 and 5 wt.% Na_2O content. The S50 mixtures exhibit a similar but less noticeable trend compared to S70 mixtures regard-

ing flexural strength, with reductions of only 14%, 16% and 2% after 7, 14 and 28 days, and a higher flexural strength of 8% after 3 curing days. In Figure 4.4b the compressive strength results are displayed for S50 mixtures with 4 and 5 wt.% Na_2O content. The results for S50 mixtures show increases in compressive strength of 43%, 21%, 11% and 14% at the corresponding curing periods.

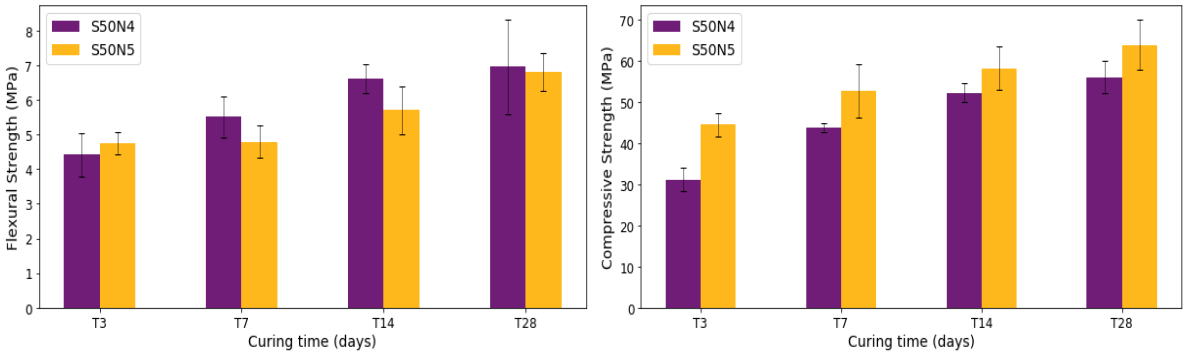

(a) Flexural strength **(b)** Compressive strength

Figure 4.4: Flexural and compressive strength results of mixtures with 50% GGBFS, 4 and 5 wt.% Na_2O content after 3, 7, 14 and 28 days of curing

4.2. Drying shrinkage and weight loss

This section presents the results of drying shrinkage and weight loss. The influence of the slag-to-fly-ash ratio on drying shrinkage and weight loss results are addressed first. Subsequently, the results for the variations in curing time and activator content are shown. Next, the correlation between shrinkage and weight loss is considered. Finally, the extent of autogenous and external shrinkage in drying shrinkage of AAMs is explored.

4.2.1. Influence of the slag-to-fly-ash ratio on drying shrinkage and weight loss

To show the effect of the slag-to-fly-ash ratio on the results of shrinkage and weight loss clearly, the results are shown separately for different curing times.

3 days of curing

Figure 4.5 illustrates the drying shrinkage and weight loss for mixtures after 3 days of sealed curing, maintaining a consistent activator content but varying slag content at 100%, 70% and 50%. The results indicate that S50 mixtures exhibit the highest drying shrinkage and weight loss compared to S70 and S100 mixtures. After 56 days of exposure, S50 mixtures show a drying shrinkage magnitude 65% larger than S100, alongside 2.86 times more weight loss. Comparing S70 and S50 mixtures after 56 days shows a drying shrinkage magnitude 32% larger in S50, along with 1.65 times more weight loss relative to S70.

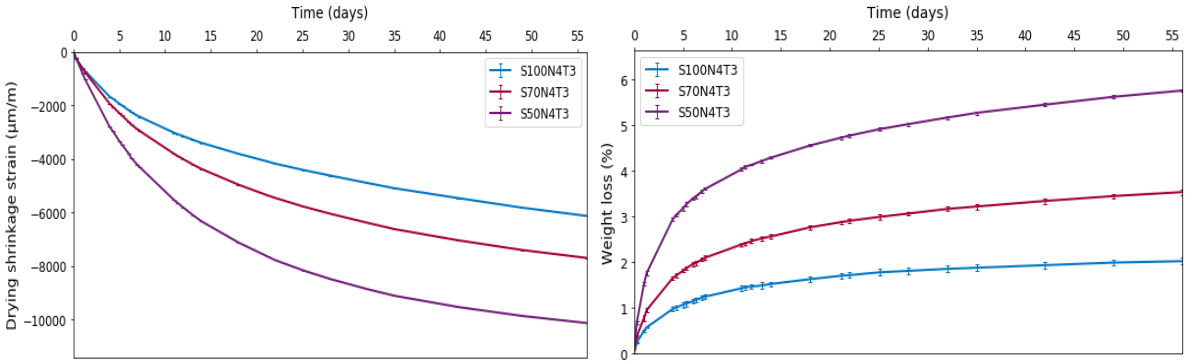

(a) Drying shrinkage strain **(b)** Weight loss

Figure 4.5: Drying shrinkage strain and weight loss of samples with 3 days of curing and 4 wt.% Na_2O content

7 days of curing

In Figure 4.6, the results after 7 days are displayed, indicating a trend similar to that observed at 3 days, though with a smaller magnitude. The magnitude of drying shrinkage at 56 days of exposure increases with 45% from S100 to S50, accompanied by a weight loss that is 2.78 times greater. Again, the difference in magnitude and weight loss between S70 and S50 is smaller but still noticeable, with 16% more drying shrinkage and 1.5 times more weight loss.

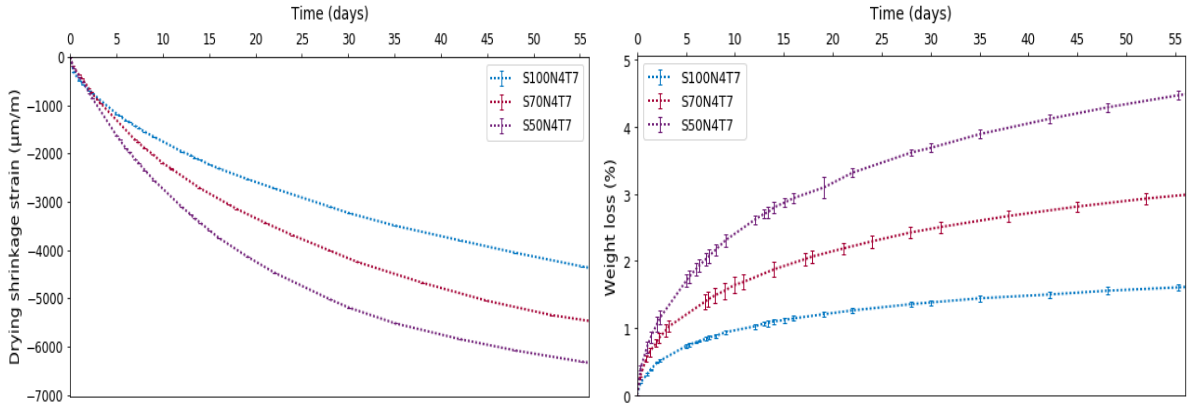

(a) Drying shrinkage strain **(b)** Weight loss

Figure 4.6: Drying shrinkage strain and weight loss of samples with 7 days of curing and 4 wt.% Na_2O content

14 days of curing

Figure 4.7 presents the results of drying shrinkage and weight loss after 14 days of sealed curing. In comparison to the observations at 3 and 7 days, the distinctions in drying shrinkage after 14 days between the S100 and S50 mixtures are less significant, showing a 26% increase. The magnitude and trend of shrinkage of S70 and S50 closely align. However, there is a notable contrast in weight loss, with S100 to S50 exhibiting 3 times more weight loss, and for S70 to S50 1.21 times more.

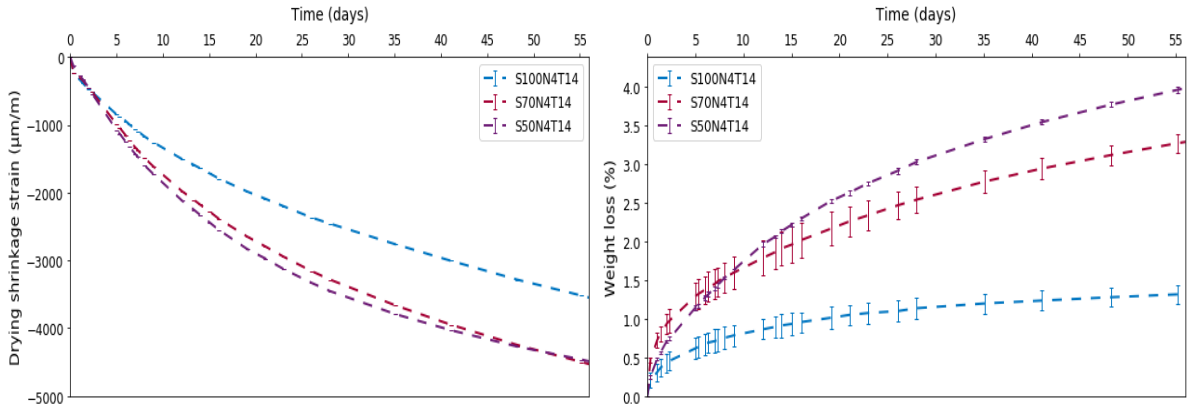

(a) Drying shrinkage strain **(b)** Weight loss

Figure 4.7: Drying shrinkage strain and weight loss of samples with 14 days of curing and 4 wt.% Na_2O content

28 days of curing

Figure 4.8 shows the results for drying shrinkage and weight loss after 28 days of curing. The drying shrinkage strain and magnitude show similarities across the three mixtures throughout the measured time. In contrast, the weight loss is 2.67 and 1.86 times greater when comparing the S100 to S50 and S70 to S50 mixtures, respectively.

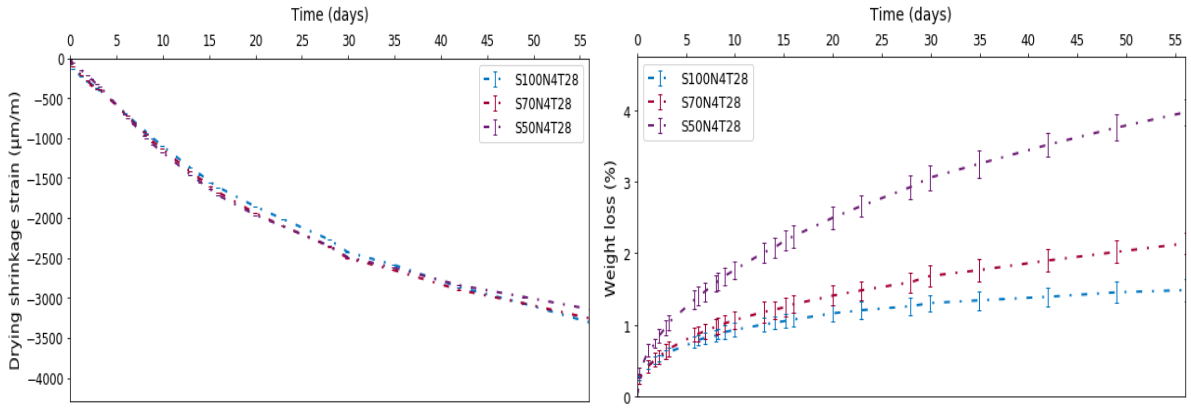

(a) Drying shrinkage strain **(b)** Weight loss

Figure 4.8: Drying shrinkage strain and weight loss of samples with 28 days of curing and 4 wt.% Na_2O content

4.2.2. Influence of the curing time on drying shrinkage and weight loss

The results related to the influence of the curing time (3, 7, 14 and 28 days) on drying shrinkage and weight loss are presented for mixtures with 100%, 70% and 50% GGBFS, with 4 wt.% Na_2O content. The results for mixtures with 5 wt.% Na_2O content are provided in Appendix A.2.

100% GGBFS

Figure 4.9 shows the drying shrinkage and weight loss results for the mixture with 100% slag and 4 wt.% Na_2O content after 3, 7, 14 and 28 curing days. After 56 days of exposure, a decrease in curing time from 28 to 3 days corresponds to a 85% increase in drying shrinkage and a 36% increase in weight loss. The results of the mixture with 7 days of curing fall within the margins of 3 and 28 days, with an increase of 32% in drying shrinkage and 9% for weight loss relative to 28 days. Although the drying shrinkage strain after 14 days of curing increased by 7% relative to 28 curing days, the weight loss is the lowest in this study for mixtures with 100% slag.

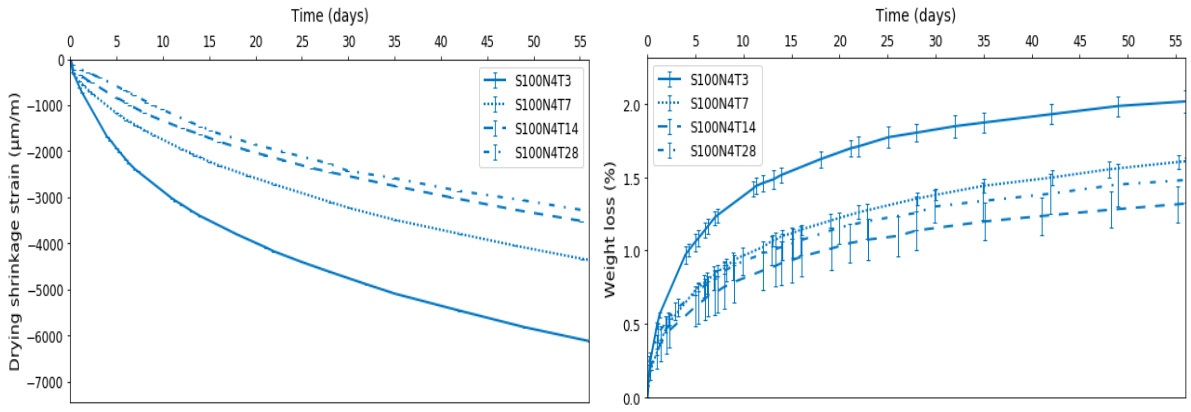

(a) Drying shrinkage strain **(b)** Weight loss

Figure 4.9: Drying shrinkage strain and weight loss of mixtures with 100% slag and 4 wt.% Na_2O content

70% GGBFS

Figure 4.10 illustrates the results of drying shrinkage and weight loss for mixtures with 70% GGBFS and 4 wt.% Na_2O content. The drying shrinkage magnitudes increases consistently over the entire exposure time when decreasing the curing time from 28, 14, 7 and 3 days. In contrast, for weight loss, an increase is observed from 28 to 7, 14 and 3 days. However, both drying shrinkage and weight loss results indicate that the curing times of 3 and 28 days serve as minimum and maximum limits.

Both the magnitude of drying shrinkage and weight loss increase by 136% and 65%, when lowering the curing time from 28 to 3 days. In the comparison between 14 and 3 days, this increase is 70% and

7%, but the difference is more significant between 0 and 30 days of exposure. From 7 to 3 days, the increase in drying shrinkage is 67%, and for weight loss it is 39%.

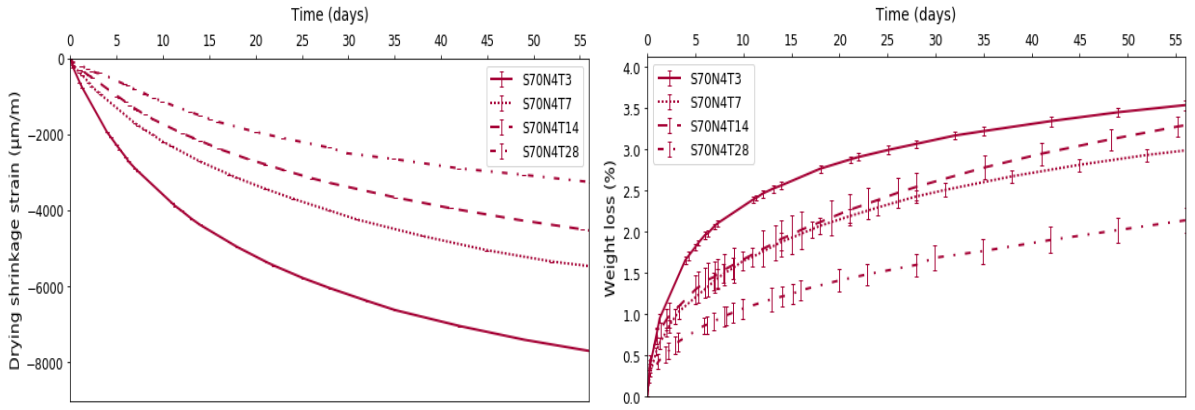

(a) Drying shrinkage strain **(b)** Weight loss

Figure 4.10: Drying shrinkage strain and weight loss of mixtures with 70% slag and 4 wt.% Na_2O content

50% GGBFS

Figure 4.11 presents the results of mixtures with 50% GGBFS. The drying shrinkage magnitude increases by 222% after 56 days of exposure when decreasing the curing time from 28 to 3 days, along with a 45% increase in weight loss. An increase in drying shrinkage and weight loss of approximately 100% and 12% is observed from 28 to 7 days. Comparing the results from 28 to 14 days reveals an increase in drying shrinkage of 42%, while weight loss appears to be equal.

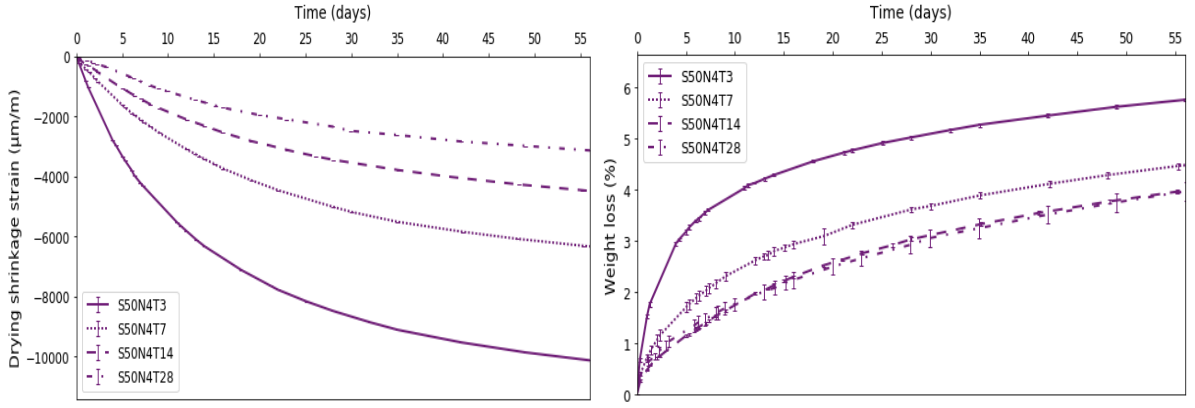

(a) Drying shrinkage strain **(b)** Weight loss

Figure 4.11: Drying shrinkage strain and weight loss of mixtures with 50% slag and 4 wt.% Na_2O content

4.2.3. Influence of the activator content on drying shrinkage and weight loss

The results in this section illustrate the influence of varying Na_2O content from 4 wt.% to 5 wt.% on drying shrinkage and weight loss in mixtures with 50% GGBFS after 3 and 28 days of curing. In Appendix A.2, the results after 7 and 14 days of the S50 mixture can be found, along with the results for the mixture with 70% GGBFS due to a similar observed trend.

Overall, mixtures with higher Na_2O content exhibit slightly higher drying shrinkage magnitudes. However, these differences converge for all curing times with minimal variation. In contrast, weight loss results indicate higher and more widespread values for mixtures with 4 wt.% Na_2O content. Over curing times from 3 and 28 days, the weight loss increases by 58% and 21% when the Na_2O content is increased.

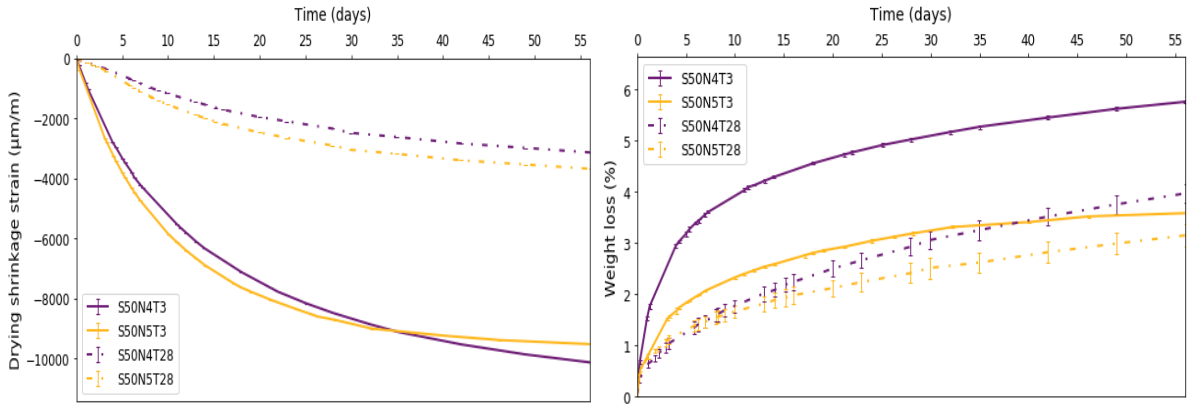

(a) Drying shrinkage strain

(b) Weight loss

Figure 4.12: Drying shrinkage strains and weight loss of samples with 50% slag and 4 or 5 wt.% Na_2O content after 3 and 28 days of curing

4.2.4. Correlation between drying shrinkage strain and weight loss

In this section, the correlation of drying shrinkage strain and weight loss for all mixtures over 56 days of exposure is considered, along with a comparison to PC (data from [17]). Again, the results regarding the influence of different slag-to-fly ash ratio are presented, followed by the influence of curing time and Na_2O content.

Figure 4.13 represents weight loss as function of drying shrinkage for mixtures S100, S70 and S50 after 7 days of curing, over 56 days of exposure to 50% RH. It is observed that with increasing GGBFS content, both drying shrinkage magnitude and weight loss decrease. Additionally, the mixtures become less sensitive to water loss as the trend becomes steeper. In comparison to PC, less weight loss but more drying shrinkage is observed for AAMs.

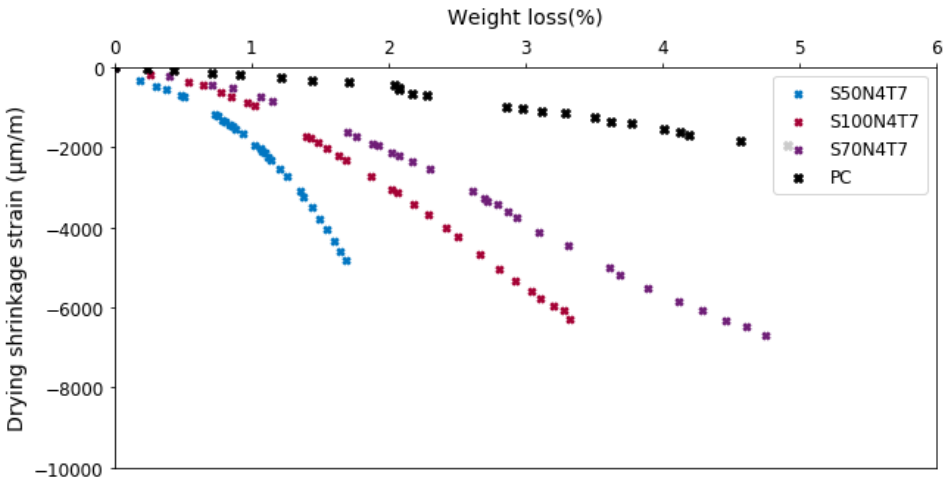

Figure 4.13: Weight loss as function of drying shrinkage for PC (data from [17]) and mixtures with 100%, 70% and 50% GGBFS after 7 days of curing over 56 days of exposure in 50% RH

In Figure 4.14, the results of weight loss as a function of drying shrinkage strain are illustrated with variations in curing time (Figure 4.14a = 3 days, Figure 4.14b = 28 days). It can be observed for the three mixtures that drying shrinkage and weight loss decrease with longer curing times. Moreover, the correlation of the S100 mixtures after 3 and 28 curing days show overlap, where the mixture with 3 days of curing shows an increase in both drying shrinkage and weight loss. This overlap decreases with an increase in fly ash content.

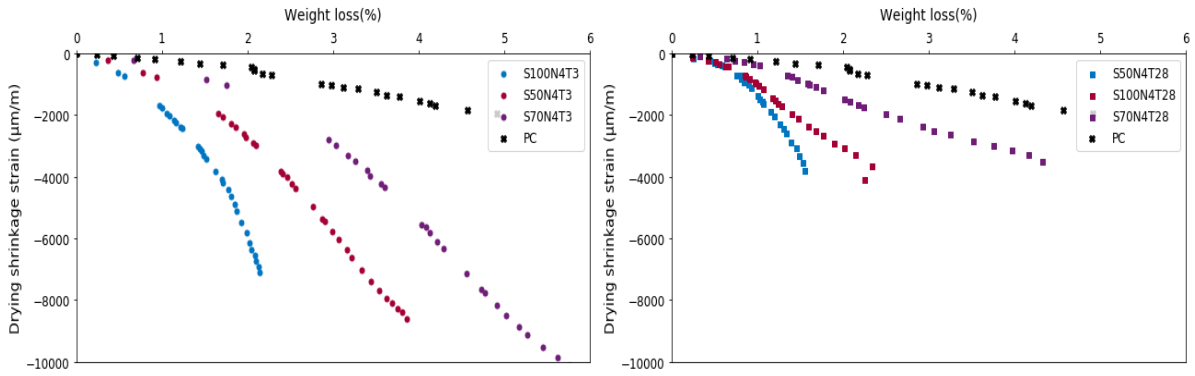

(a) 3 curing days **(b)** 28 curing days

Figure 4.14: Weight loss as function of drying shrinkage for PC (data from [17]) and mixtures with 100%, 70% and 50% GGBFS over 56 days of exposure in 50% RH

Figure 4.15 shows the relationship between weight loss and drying shrinkage for mixtures with 4 wt.% and 5 wt.% Na_2O content and 50% GGBFS. Observable is that, for equal drying shrinkage magnitudes, mixtures with higher activator content are less prone to moisture loss, which is most evident for samples with shorter curing times.

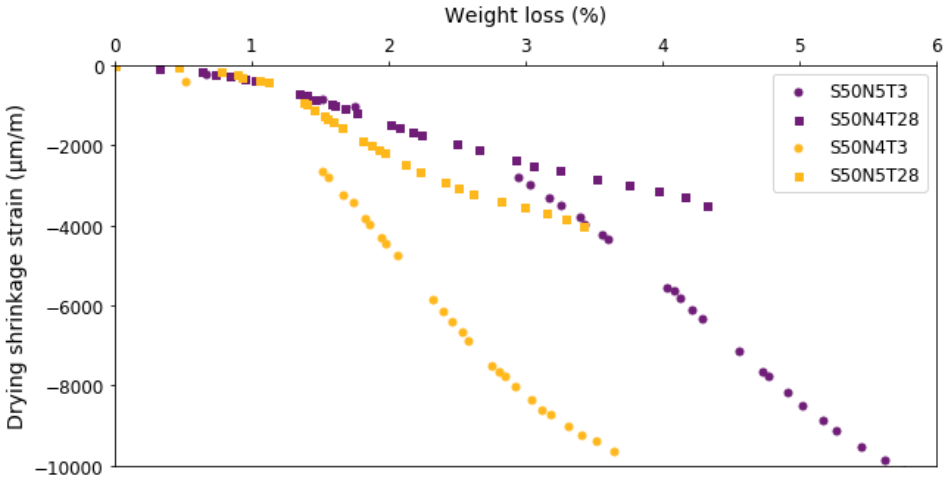

Figure 4.15: Weight loss as function of drying shrinkage for mixtures with 4 wt.% and 5 wt.% Na_2O content and 50% GGBFS over 56 days of exposure in 50% RH. Curing times are indicated with symbols, T3:● and T28:□.

4.2.5. Autogenous shrinkage and external drying shrinkage

As mentioned in Section 2.2.3, drying shrinkage is linked to both internal reactions during hydration, leading to autogenous shrinkage, and external water loss influenced by environmental conditions, referred to as external drying shrinkage. To specifically examine the contribution of external drying shrinkage, the autogenous shrinkage results are presented first for the mixtures with 4 wt.% Na_2O content. Subsequently, the extent of autogenous and external drying shrinkage in AAMs is investigated. The results of the final setting time to calculate the autogenous shrinkage of the mixtures are shown in Table 4.1. It is observed that the setting time increases for lower slag content.

Table 4.1: Final setting time results according to EN 196-3

Mix design	Final setting time [min]
S100N4	117
S70N4	146
S50N4	207

The results of the autogenous shrinkage, measured from final setting time, are shown in Figure 4.16. It is notable that, across all mixtures, autogenous shrinkage is most prominent in the initial three days after casting. Furthermore, the magnitude of autogenous shrinkage in S100 mixtures is nearly 4.5 times larger than in S50 mixtures after 3 days. This difference decreases to 2.70 times difference after 28 days.

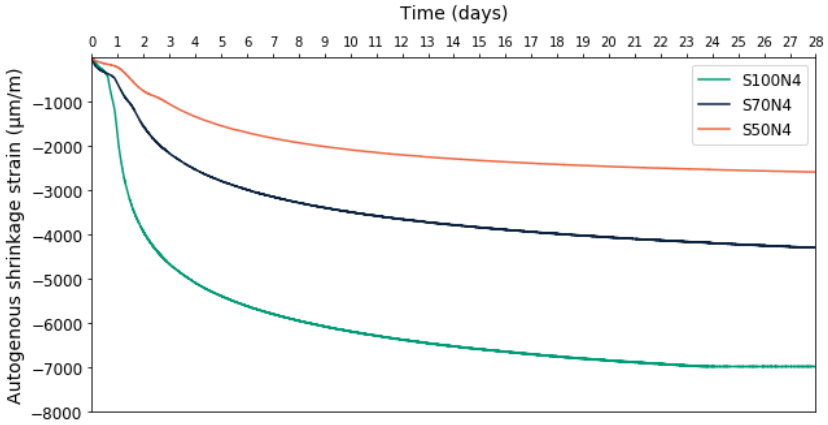

Figure 4.16: Autogenous shrinkage of N4 mix designs measured for 28 days

To make a distinction between autogenous shrinkage and external drying shrinkage, the autogenous shrinkage results are adjusted by shifting the coordinate system to 3 and 14 sample days. Figure 4.17 illustrates this translation for the S100N4T3 mixture, with the origin of the translated coordinate system set at (3, -4682). Following this, the autogenous shrinkage strain is subtracted from the drying shrinkage strain to derive the external drying shrinkage strain.

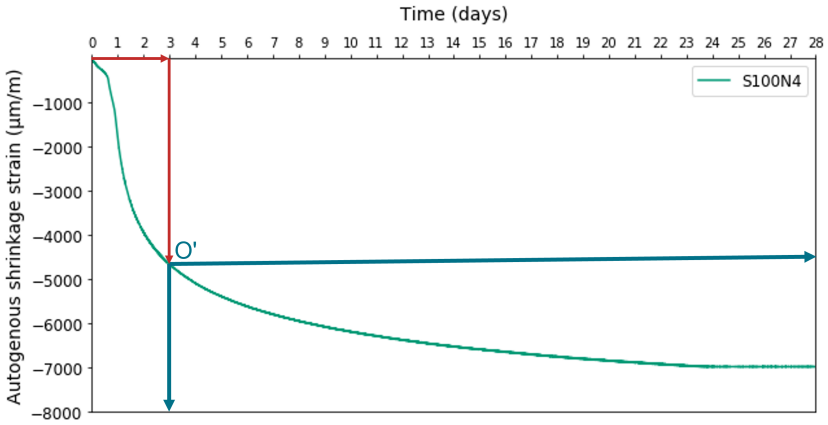

Figure 4.17: Translation of the coordinate system for S100N4T3 mixture after 3 days of curing, with (3, -4682) as new origin (O')

Figure 4.18 presents the results, including a extent of autogenous shrinkage and external drying shrinkage in drying shrinkage for mixtures with different GGBFS percentages, measured over a total sample age of 28 days. The drying shrinkage measurements started after 3 and 14 curing days. It is observed that the proportion of external drying shrinkage relative to autogenous shrinkage increases with an extended curing time. Furthermore, the extent of external drying shrinkage is higher than autogenous shrinkage in all cases, except for the mixture with 100% GGBFS and a sample age of 3 days (Figure 4.18a). However, for the latter case, the degree of external drying and autogenous shrinkage are equal after 28 days. Regarding the slag content in the mixture, it is observed that the extent of external drying shrinkage increases with decreasing GGBFS content in the mixture.

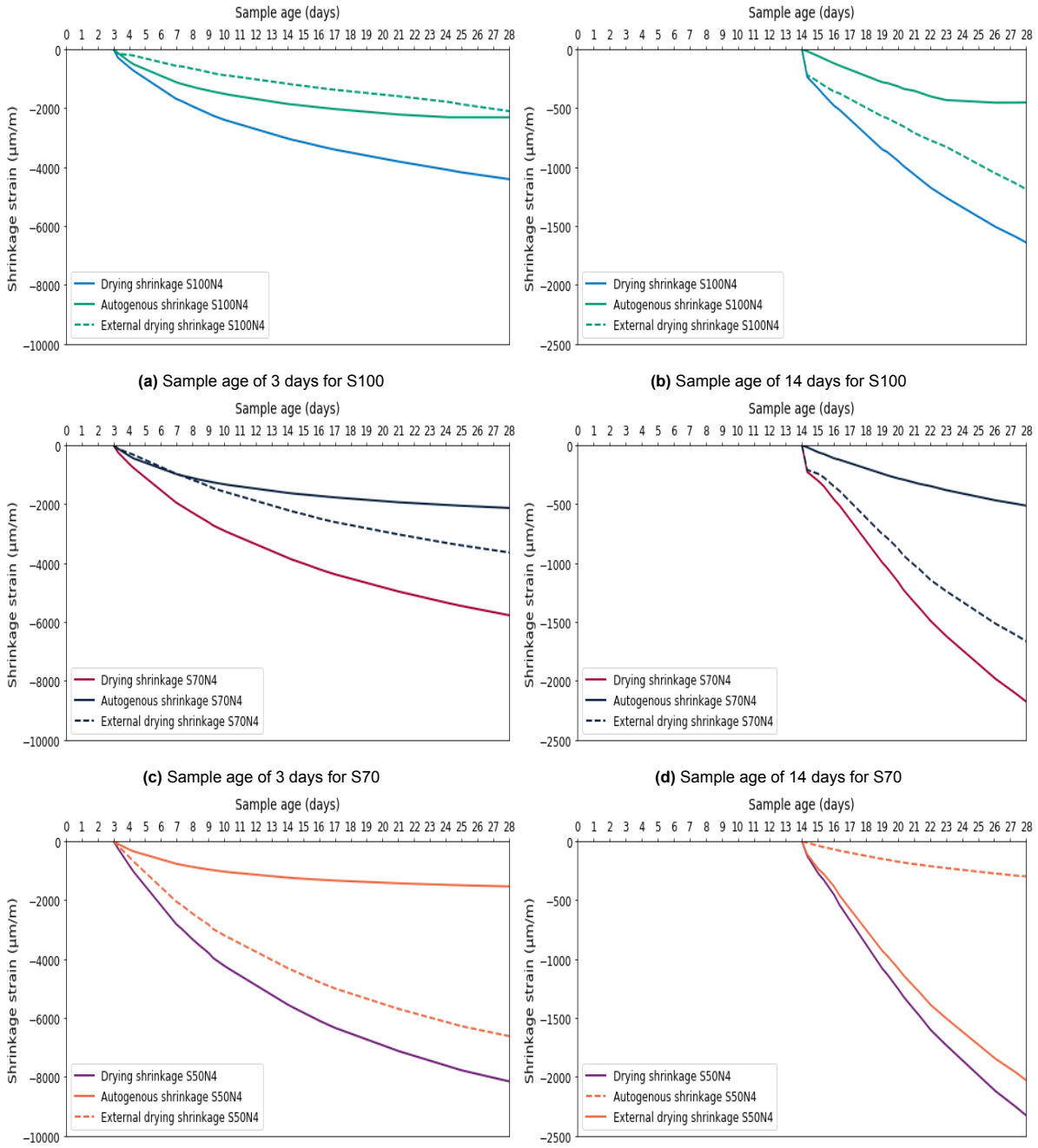

(a) Sample age of 3 days for S100

(b) Sample age of 14 days for S100

(c) Sample age of 3 days for S70

(d) Sample age of 14 days for S70

(e) Sample age of 3 days for S50

(f) Sample age of 14 days for S50

Figure 4.18: Proportion of autogenous shrinkage and external drying shrinkage in mixtures with different GGBFS percentages (100%, 70%, and 50%) and 4 wt.% Na_2O content, observed after 3 days (left) and 14 days (right)

4.3. Porosity and pore size distribution results

The results from the MIP experiments are outlined in this section. First, the porosity of the samples is presented. Subsequently, the influence of slag-to-fly ash ratio, curing time and activator content is considered, with the same structure as the results on drying shrinkage and weight loss. It should be noted that the data set is not complete due to technical problems with the available equipment.

In Table 4.2, the porosity measured by mercury intrusion of the mixtures is presented. It is observed that, for all mixtures, the porosity decreases with longer curing times. The increase in curing time from 3 to 14 days corresponds to a porosity decrease of 30%, 30% and 15% for mixtures with 100%, 70% and 50% GGBFS, respectively, and equal activator content. For mixtures with equal curing times but decreasing slag content (100% to 50%), the porosity increases for all curing times. Regarding 3 days, an increase of 39% is measured, for 7 and 14 days increases of 77% and 69% are noticed.

Table 4.2: Porosity by mercury intrusion of mixtures

	Porosity (%)			
	T3	**T7**	**T14**	**T28**
S100N4	15.85	12.07	11.14	8.63
S70N4	20.48	17.24	14.33	
S50N4	22.10	21.39	18.84	
S50N5	17.85			

4.3.1. Influence of slag-to-fly-ash ratio on porosity and pore size distribution

The influence of varying slag-to-fly-ash ratios are shown for each curing time.

3 days of curing

Figure 4.19 illustrates the results of the cumulative pore volume (Fig. 4.19a) and the differential pore size distribution (Fig. 4.19b), for mixtures with 100%, 70% and 50% GGBFS after 3 days of curing and 4 wt.% Na_2O content. From the differential pore size distribution it is observed that with increasing slag content the pore structure refines, as almost no pores are measured larger than 0.02 μm. The aforementioned decrease in porosity of 39% between S100 and S50 is also reflected in Figure 4.19a. For the S50 and S70 mixtures, a peak is visible around 0.002 μm.

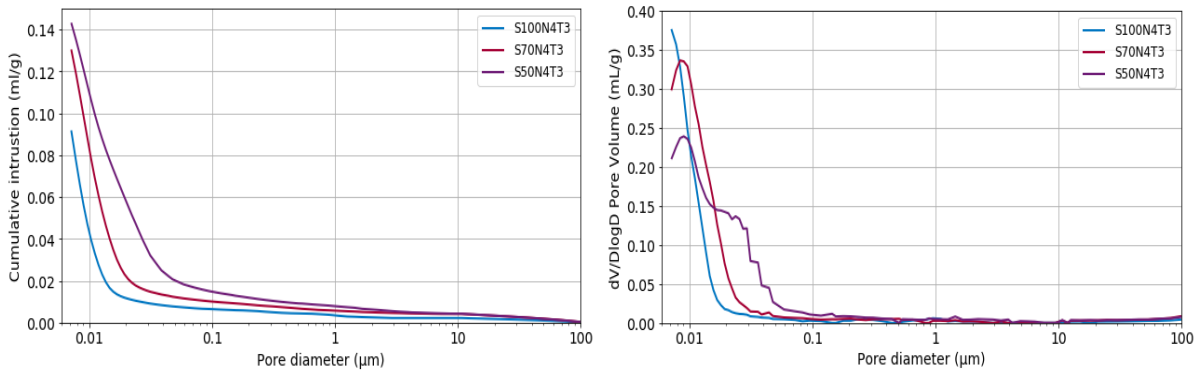

(a) Cumulative pore size distribution after 3 days of curing

(b) Differential pore size distribution after 3 days of curing

Figure 4.19: Capillary pore volume and differential pore size distribution of mixtures with 3 days of curing and 4 wt.% Na_2O

7 days of curing

Figure 4.20 shows the results of cumulative pore volume and differential pore size distribution for mixtures after 7 days of curing. The pore sizes are mainly present within the medium and small isolated capillaries region. The cumulative intrusion of the 7-day samples are more widely spaced, with 77% increase between S100 and S50 and 43% increase between S100 and S70. Only a peak in pore sizes is visible for the S50 mixture around 0.0015 μm, for the S100 and S50 mixtures, a steep line can be seen that contains no peak.

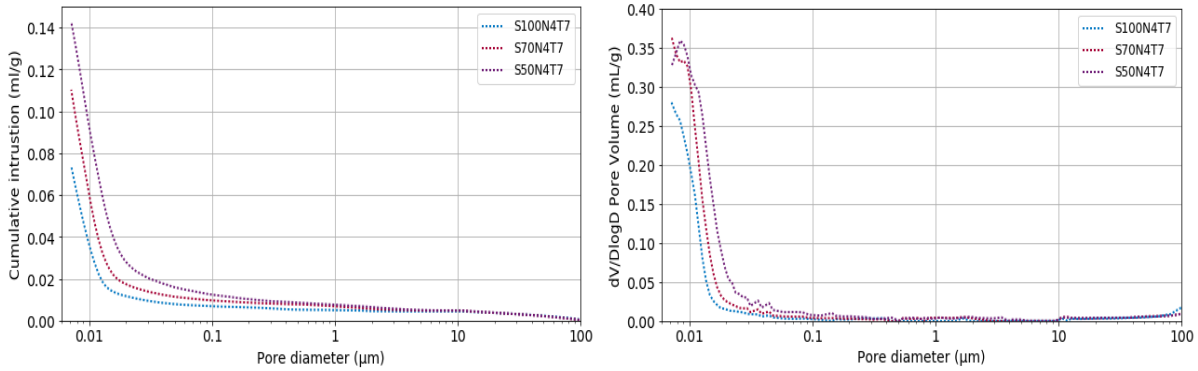

(a) Cumulative pore size distribution after 7 days of curing

(b) Differential pore size distribution after 7 days of curing

Figure 4.20: Capillary pore volume and differential pore size distribution of mixtures with 7 days of curing and 4 wt.% Na_2O

14 days of curing

Figure 4.21 illustrates the results of cumulative pore volume and differential pore size distribution after 14 days of curing. Once again, a prominent peak around 0.01 μm is evident for the S50 mixture. The pore structure further refines, leading to a 29% increase in porosity from S100 to S70 and a 69% increase from S100 to S50. Additionally, a bump is observed around 0.5 μm for the S100 mixture.

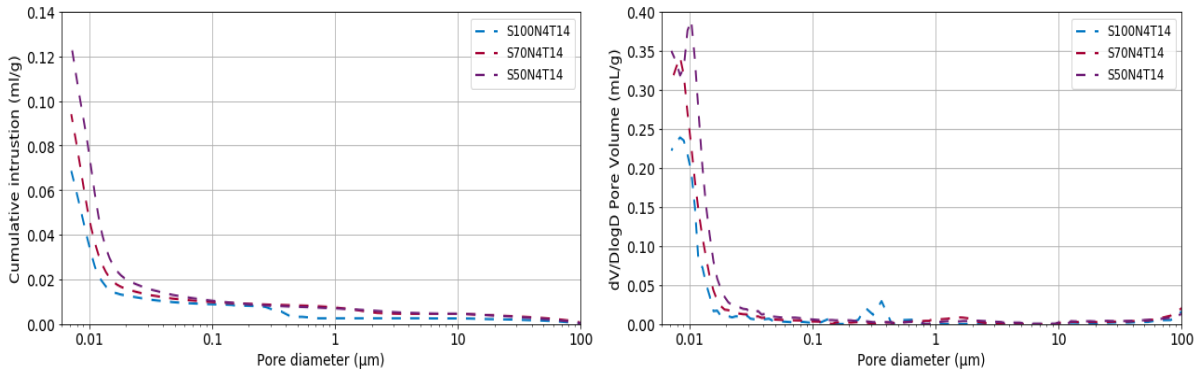

(a) Cumulative pore size distribution after 14 days of curing

(b) Differential pore size distribution after 14 days of curing

Figure 4.21: Capillary pore volume and differential pore size distribution of mixtures with 14 days of curing and 4 wt.% Na_2O

4.3.2. Influence of the curing time on porosity and pore size distribution

The results related to the influence of the curing time (3, 7, 14 and 28 days) on porosity and pore size distribution are presented for mixtures with 100%, 70% and 50% GGBFS, with 4 wt.% Na_2O content.

100% GGBFS

In Figure 4.22, the results of the MIP experiments are presented for samples with 100% GGBFS, including the 28-day measurement. Both results of cumulative pore volume and differential pore size distribution show that with increasing curing time, the pore sizes become refined. From 3 to 28 days, the porosity decreases with 46%. The observed bump around between 70-100 μm is due to incomplete filling of mercury between the particles in the penetrometer in the low pressure analysis, therefore, this region is not of importance for this study.

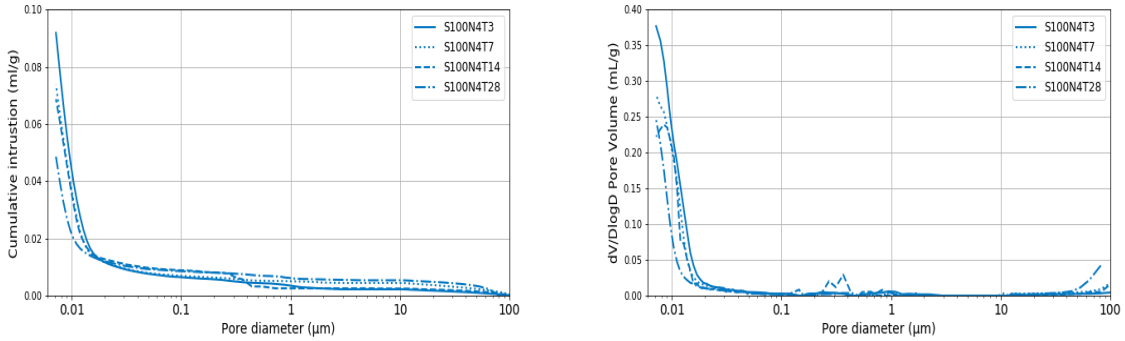

(a) Cumulative pore size distribution of mixtures with 100% GGBFS

(b) Differential pore size distribution of mixtures with 100% GGBFS

Figure 4.22: Capillary pore volume and differential pore size distribution of mixtures with 100% GGBFS and 4 wt.% Na_2O content

70% GGBFS

In Figure 4.23, the results of cumulative pore volume and differential pore size distribution of the mixture containing 70% GGBFS are indicated. The differential pore size distribution shows refining of the pores from 3 to 7 to 14 days. In addition, a peak for both 3 and 14 days mixtures is observed around 0.02 µm. The cumulative intrusion and related porosity indicate a similar refining, with a decrease of 15% from 3 to 7 and 50% from 3 to 14 days.

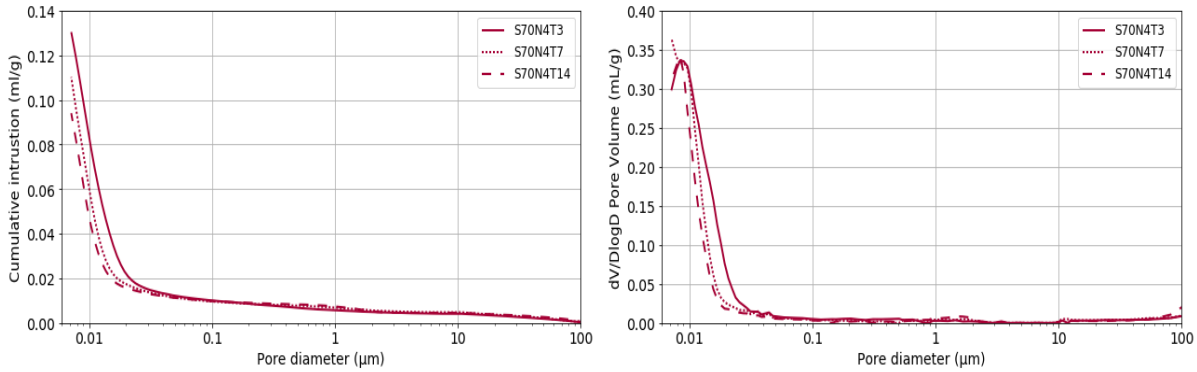

(a) Cumulative pore volume of mixtures with 70% slag

(b) Differential pore size distribution of mixtures with 70% slag

Figure 4.23: Capillary pore volume and differential pore size distribution of mixtures with 70% GGBFS and 4 wt.% Na_2O content

50% GGBFS

Figure 4.24 presents the results of cumulative pore volume and differential pore size distribution for mixtures with 50% GGBFS and 4 wt.% Na_2O content. The refinement of pores is clearly visible from 3 to 14 curing days, since the pore sizes between 0.02 and 0.05 µm disappears after 3 days of curing. The porosity decreases only 3% from 3 to 7 days, in contrast to the porosity between 3 and 14 days which decreases 15%.

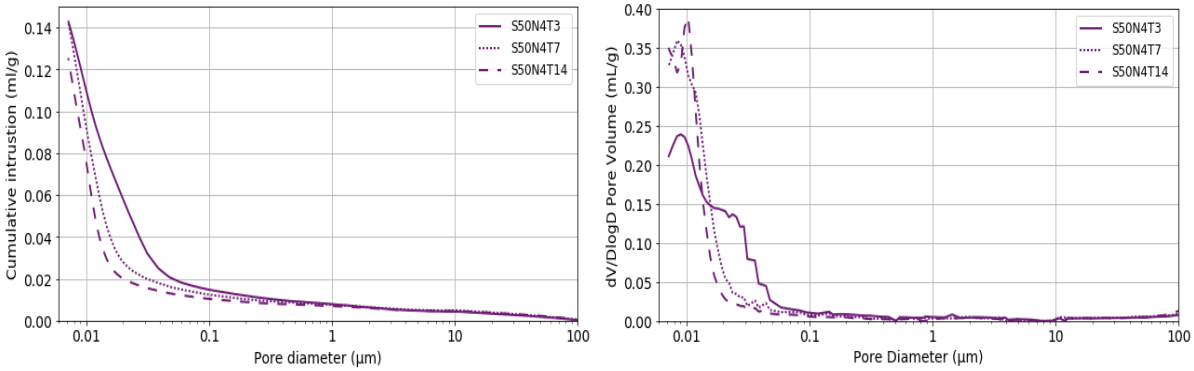

(a) Cumulative pore size distribution of mixtures with 50% slag

(b) Differential pore size distribution of mixtures with 50% slag

Figure 4.24: Capillary pore volume and differential pore size distribution of mixtures with 50% GGBFS and 4 wt.% Na_2O content

4.3.3. Influence of activator content on porosity and pore size distribution

The results presented in Figure 4.25 illustrate the influence of Na_2O content on pore size distribution and porosity for the mixture with 50% slag after 3 days of curing. There is a 19% decrease in porosity when the activator content increases from 4 to 5 wt.% Na_2O. In addition, the coarser pore structure observed for mixtures with 4 wt.% Na_2O is not evident in the mixture with 5 wt.% Na_2O, which demonstrates a more refined structure.

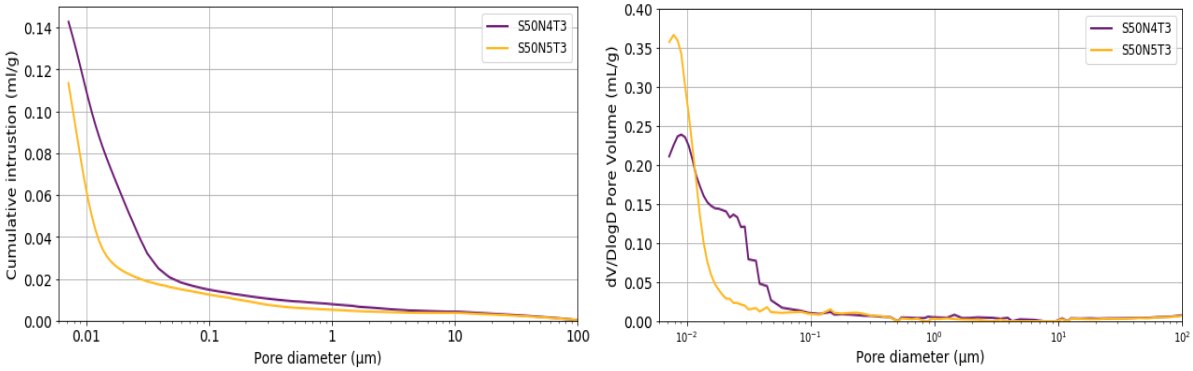

(a) Cumulative pore size distribution with 4 and 5 wt.% Na_2O content

(b) Differential pore size distribution with 4 and 5 wt.% Na_2O content

Figure 4.25: Capillary pore volume and differential pore size distribution with 4 and 5 wt.% Na_2O content

4.4. Results of the pore structure analysis and selection

This section presents the results of the sample selection based on an uniform pore size distribution, following the method outlined in Section 3.5. This approach enables the assessment of how different reaction products affect the drying shrinkage mechanism, given the determined uniformity in pore structure at the time of exposure. The method includes visual inspection, area under the curve analysis, sample selection, and subtraction of the area under the curve for medium (0.01-0.05 μm) and small isolated capillaries (0.0025-0.01 μm). Applying this method demonstrates two occurrences of overlapping pore structures. The first match is between S100N4T3 and S70N4T14, and the second is between S70N4T7 and S50N5T3.

The result of the visual inspection of the first is presented in Figure 4.26a, along with the corresponding area under the curve calculation in Figure 4.26b. For the small isolated capillaries the difference between S100N4T3 and S70N4T14 are 1.51%, the medium capillaries contain a difference of 0.12%. In addition, the results of porosity shown in Table 4.2 are close together.

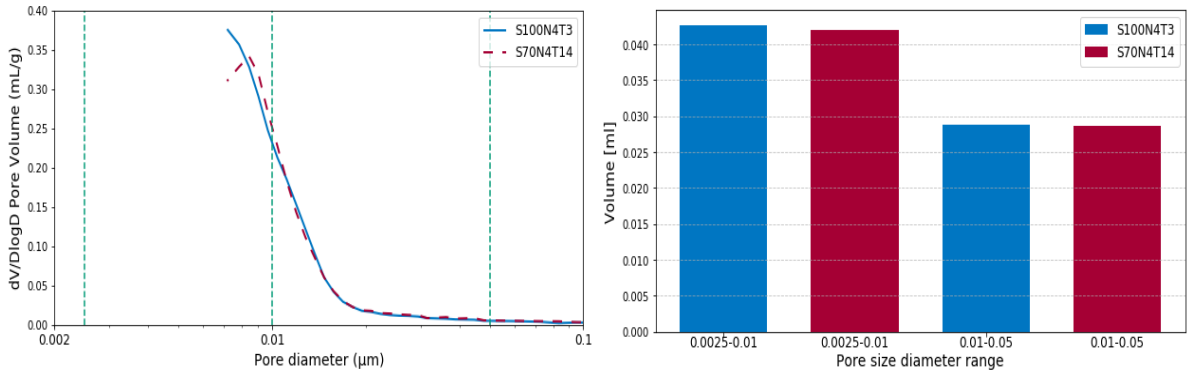

(a) Visual inspection **(b)** Area under the curve

Figure 4.26: Sample selection based on pore size distribution for S100N4T3 and S70N4T14

In Figure 4.27, the results of the pore structure analysis and selection are presented for the samples S70N4T7 and S50N5T3. The results of both visual inspection and area under the curve show that the overlap is within the requirements. Concerning the small isolated capillaries, there is a difference of 3.42%, and for the medium capillaries, a difference of 3.08% is observed. The total porosity results of the samples show a percentage difference of 3.36%.

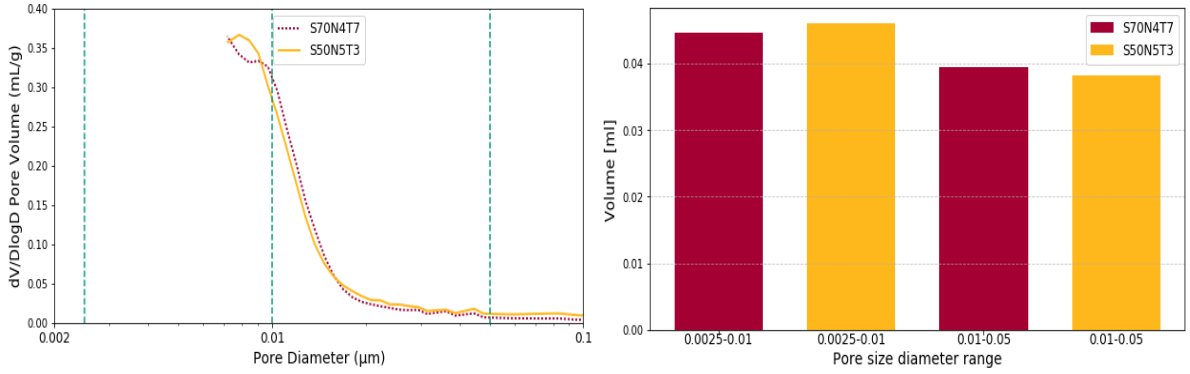

(a) Visual inspection **(b)** Area under the curve

Figure 4.27: Sample selection based on pore size distribution for S70N4T7 and S50N5T3

Based on the aforementioned selection in Figures 4.26 and 4.27, the results of the conducted experiments are compared in Section 4.5 for S100N4T3 and S70N4T14 , and in Section 4.6 for the samples S70N4T7 and S50N5T3.

4.5. A comparative study: S100N4T3 and S70N4T14 results

This section compares the results of samples S100N4T3 and S70N4T14, as the pore size distribution of these samples is equal, as shown in the previous section. The analysis begins with an examination of drying shrinkage and weight results, followed by an evaluation of compressive and flexural strength. Finally, observations regarding chemical composition and the volume of reaction products are shown.

4.5.1. Drying shrinkage and weight loss results

Figure 4.28 presents the results of drying shrinkage and weight loss of the selected samples. Based on the pore structure analysis and selection, it is known that the pore structure at the moment of exposure to the drying shrinkage test (t=0 in Figure 4.28) is considered to be equal. It is observed that, compared to S100N4T3, the S70N4T14 sample displays less drying shrinkage, while the weight loss is higher. After 28 days, S70N4T14 shows 29% less drying shrinkage and a 41% increase in weight loss. After 56 days, the difference in drying shrinkage decreased to 26%, in contrast to the weight loss results, which show a 64% increase (relative to 28 days, an increase of 23%).

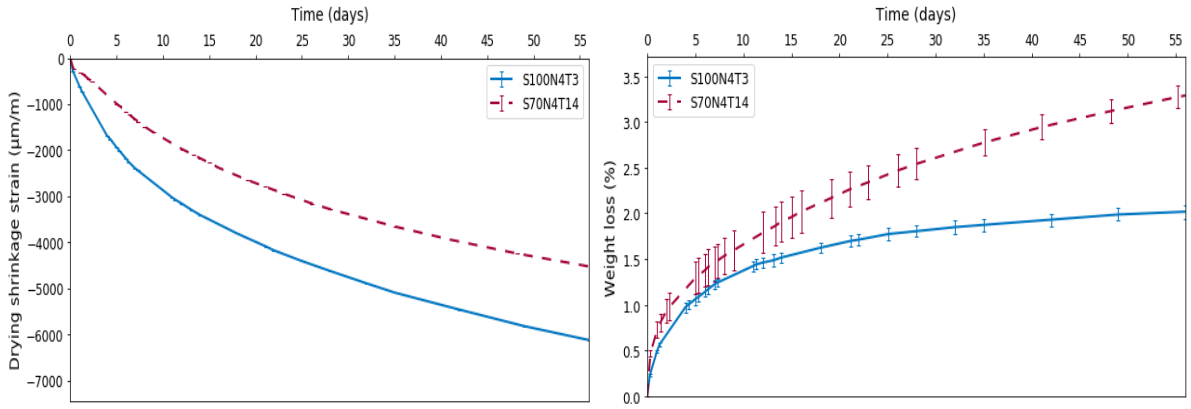

(a) Drying shrinkage strain **(b)** Weight loss

Figure 4.28: Drying shrinkage strains and weight loss of S100N4T3 and S70N4T14

Figure 4.29 illustrates the proportion of autogenous shrinkage and external drying shrinkage for both samples, clearly indicating the moment when the specimens were exposed to 50% RH. A comparison of the two mixtures show that the total drying shrinkage, after the same sample age of 28 days, increases by approximately 100%. When examining the autogenous shrinkage and external drying shrinkage separately, it can be observed that the proportion of external drying shrinkage only increases by 27% from S70N4T14 to S100N4T3, while autogenous shrinkage increases substantially by 350%.

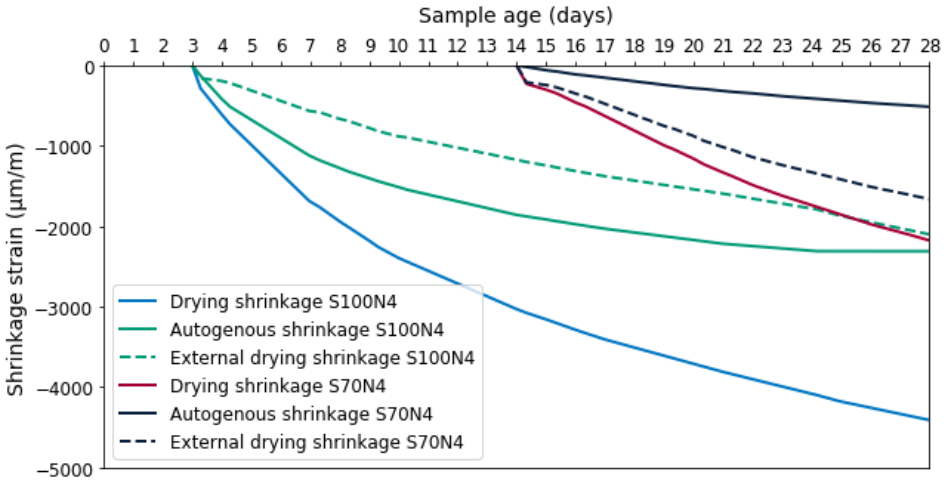

Figure 4.29: Proportion of autogenous shrinkage and external drying shrinkage for the S100N4T3 and S70N4T14 mixtures

4.5.2. Flexural and compressive strength results

In Table 4.3 the results of flexural and compressive strength of S100N4T3 and S70N4T14 are presented. The flexural strength of S70N4T14 is 1.94% lower than S100N4T3, while the compressive strength is observed to be 37% higher.

Table 4.3: Results of flexural and compressive strength of S100N4T3 and S70N4T14

	Flexural strength (MPa)	Compressive strength (MPa)
S100N4T3	10.3	39.9
S70N4T14	10.1	54.6

4.5.3. Volume of reaction products and chemical composition results

The results from SEM-EDX point analysis are demonstrated in Table 4.4. The Al/Si ratio is observed to be approximately equal, while the Ca/Si and Na/Si ratios differ. Specifically, the Ca/Si ratio of S100N4T3 is 21% higher compared to S70N4T14, and the Na/Si ratio is 44% higher.

Table 4.4: Mean atomic ratios and amount of reaction products of S100N4T3 and S70N4T14

	Ca/Si	Na/Si	Al/Si	Amount of products (%)
S100N4T3	1.06	0.34	0.31	70.1
S70N4T14	0.88	0.23	0.32	59.5

Segmentation is performed for the samples based on SEM images shown in Figure 4.30. These images are used to determine the amount of reaction products, and the results are presented in Table 4.4. The quantity of reaction products in S100N4T3 is 18% higher relative to S70N4T14. The SEM image of S100N4T3 preliminary shows reaction products and unreacted slag particles, with some small pores observed. In the S70N4T14 image, unreacted spherical fly ash particles are distinguishable, exhibiting a wide range of diameter sizes. The presence of pores is attributed not only to the matrix, but also to the porous fly ash particles.

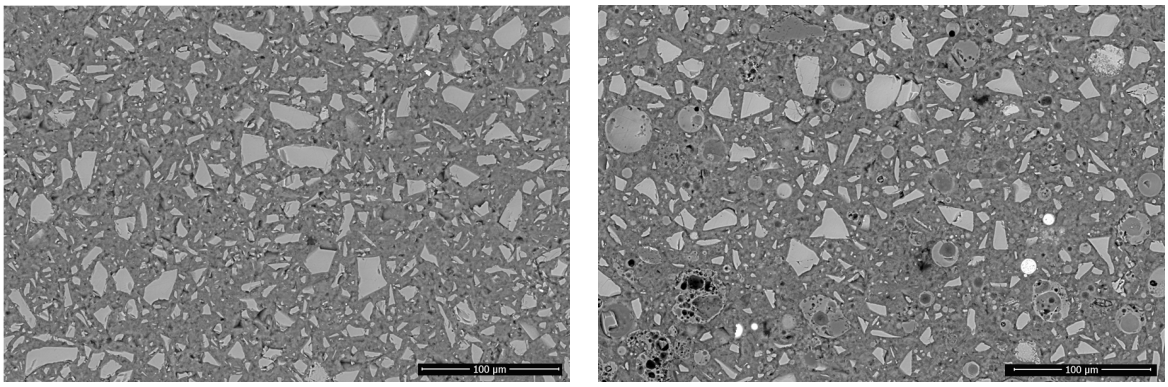

(a) SEM image of S100N4T3

(b) SEM image of S70N4T14

Figure 4.30: SEM images of S100N4T3 and S70N4T14 with accelerating voltage of 15 kV, magnitude of 1000 and 10 mm working distance.

Figure 4.31 presents the results of the points analysis for the Ca/(Si+Al) and Na/(Si+Al) ratios. S100N4T3 is only observed for Ca/(Si+Al) above 0.6, while S70N4T14 is scattered along the complete Ca/(Si+Al) axis with values between 0.1 and 1.1. Therefore, it is stated that the phase distribution of S100N4T3 is more homogeneous.

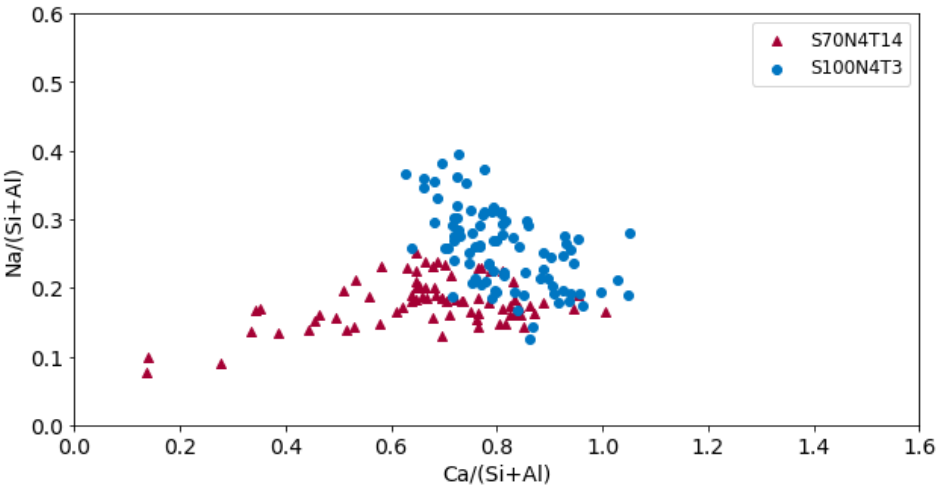

Figure 4.31: 2D scatter plots of EDX point analysis of Na/(Si+Al) and Ca/(Si+Al) ratios for S100N4T3 and S70N4T14

The homogeneous phase distribution of S100N4T3 is also reflected in Figure 4.32a and 4.32b. Figure 4.32c presents the linear correlation between Al/Si and Mg/Si for S100N4T3; for S70N4T14, no linear correlation is observed. In Figure 4.32d, it is visible that more calcium is present in the system than silica, reflecting the presence of C-A-S-H type gels. For S70N4T14, the points are distributed between 0.74 and 6.13, indicating a more heterogeneous distribution. This heterogeneity can be explained due to the incorporation of fly ash, giving the formation of C-N-A-S-H gels or the intermixed binding of both C-A-S-H and N-A-S-H gels. This observation is also mentioned by Garcia-Lodeiro *et al.*, Ismail *et al.* [42, 43].

In Figure 4.33, a ternary diagram presenting normalized values for atomic Ca/Si, Na/Si and Al/Si ratios for S100N4T3 and S70N4T14 mixtures is shown. The ratios of Ca, Na and Al are normalized with respect to the Si quantity, ensuring that the summation of the ratios equals 1. The ternary diagram can be used as a tool to identify the gel composition of the paste matrix [18, 68]. Regarding the results, the more homogeneous distribution of S100N4T3 is once again observed, while the S70N4T14 results indicate scattering of the Ca/Si atomic ratio.

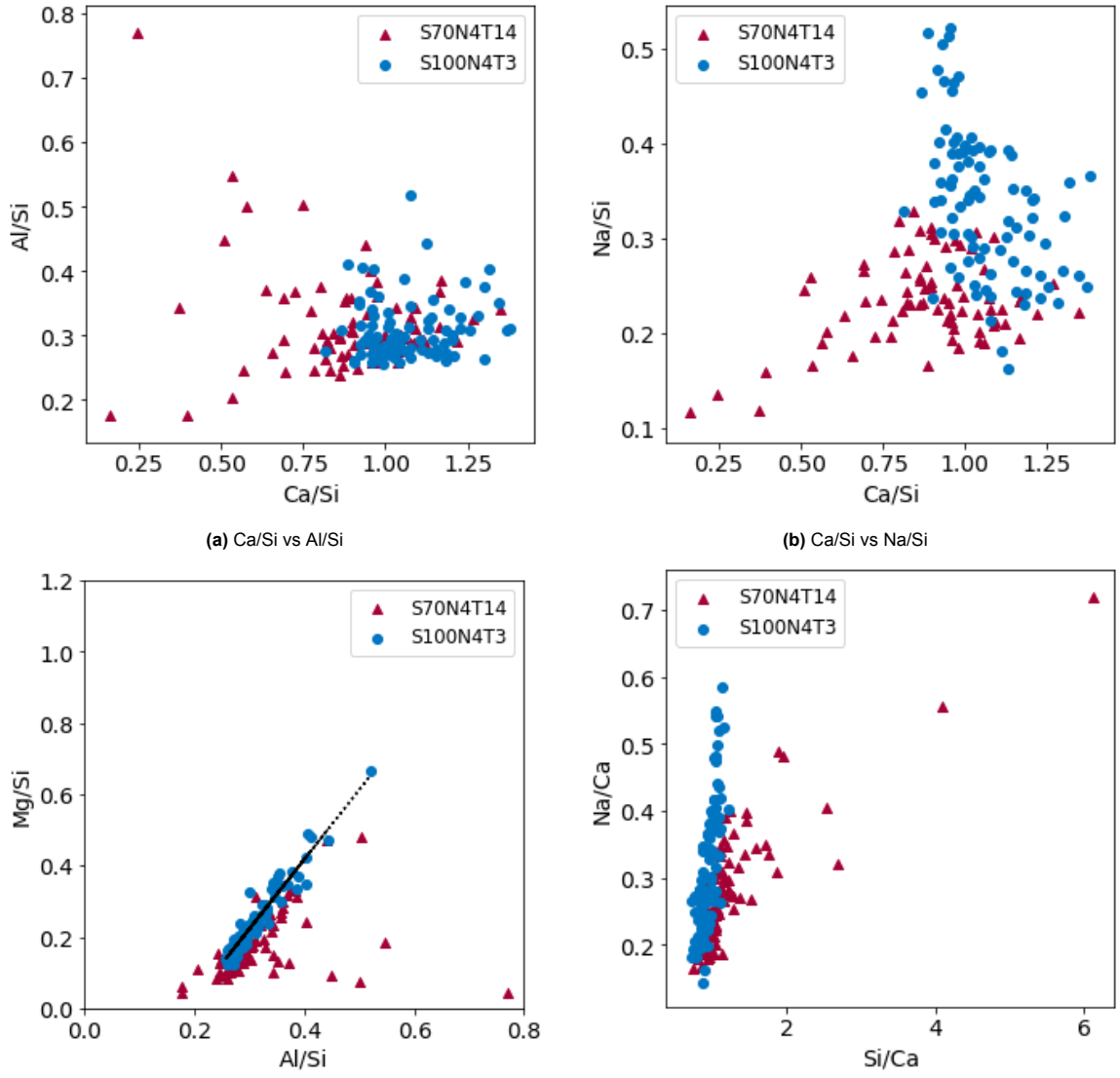

(a) Ca/Si vs Al/Si

(b) Ca/Si vs Na/Si

(c) Al/Si vs Mg/Si

(d) Si/Ca vs Na/Ca

Figure 4.32: Atomic ratios of the elements in the matrix of the S100N4T3 and S70N4T14

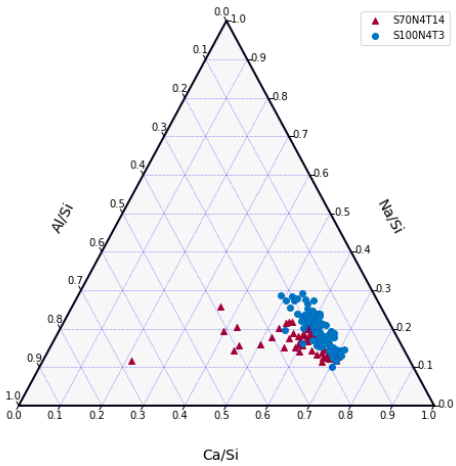

Figure 4.33: Ternary diagram of normalised Ca/Si, Na/Si and Al/Si ratios for S100N4T3 and S70N4T14

4.6. A comparative study: S70N4T7 and S50N5T3 results

This section presents the results of samples S70N4T7 and S50N5T3. In line with Section 4.5, drying shrinkage, weight loss, compressive and flexural strength results are demonstrated. Followed by the finding regarding chemical composition and the volume of reaction products.

4.6.1. Shrinkage and weight loss results

In Figure 4.34, the results of drying shrinkage and weight loss for samples S70N4T7 and S50N5T3 are presented. This comparison shows that the drying shrinkage strain of S50N5T3 is 117% and 74% higher than that of S70N4T7 after 28 and 56 days, respectively. For S50N5T3, the most significant rise in drying shrinkage is observed during the first 15 days after exposure to 50% RH. Moreover, the weight loss of S50N5T3 is 31% higher for 28 days and 20% higher after 56 days. The results indicate that after 28 days, the drying shrinkage and weight loss converge.

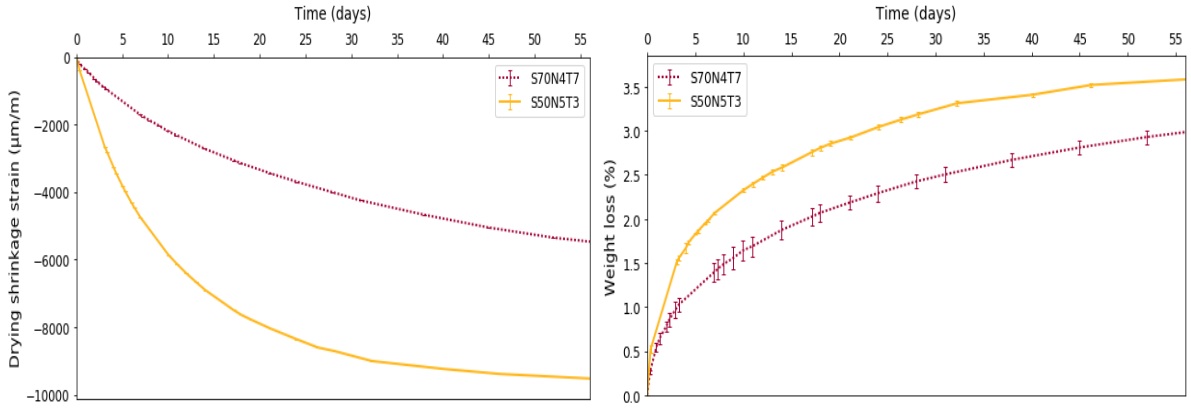

(a) Drying shrinkage strain **(b)** Weight loss

Figure 4.34: Drying shrinkage strains and weight loss of S70N4T7 and S50N5T3

4.6.2. Flexural and compressive strength results

Table 4.5 presents the compressive and flexural strength results of S70N4T7 and S50N5T3. The flexural strength of S70N4T7 is twice as high than the flexural strength of S50N5T3. In contrast, the results of the compressive strength align with each other.

Table 4.5: Results of flexural and compressive strength of S70N4T7 and S50N5T3

	Flexural strength (MPa)	Compressive strength (MPa)
S70N4T7	9.7	45.2
S50N5T3	4.8	44.5

4.6.3. Volume of reaction products and chemical composition

The average atomic ratios extracted from the point analysis are presented in Table 4.6. The comparison shows that the Ca/Si atomic ratio becomes higher for higher GGBFS content. The atomic Na/Si ratio of S70N4T7 is 11% lower relative to S50N5T3, while the atomic Al/Si ratio remains approximately equal.

Table 4.6: Mean atomic ratios and amount of reaction products of S70N4T7 and S50N5T3

	Ca/Si	Na/Si	Al/Si	Amount of products (%)
S70N4T7	0.86	0.26	0.33	52.4
S50N5T3	0.71	0.29	0.32	34.2

In comparison with the Section 4.5, less matrix is observed in Figure 4.35, this observation is in line with the amount of reaction products measured through segmentation (result in Table 4.6). In Figure 4.35a, a selected SEM image of S70N4T7 with 1000 magnitude and 15 kV accelerating voltage is shown. Next to the pores, matrix and unreacted GGBFS and FA particles, micro-cracks are observed. In Figure

4.35b, an SEM image of the S50N5T3 sample is presented, revealing significant more micro-cracks compared to S70N4T7.

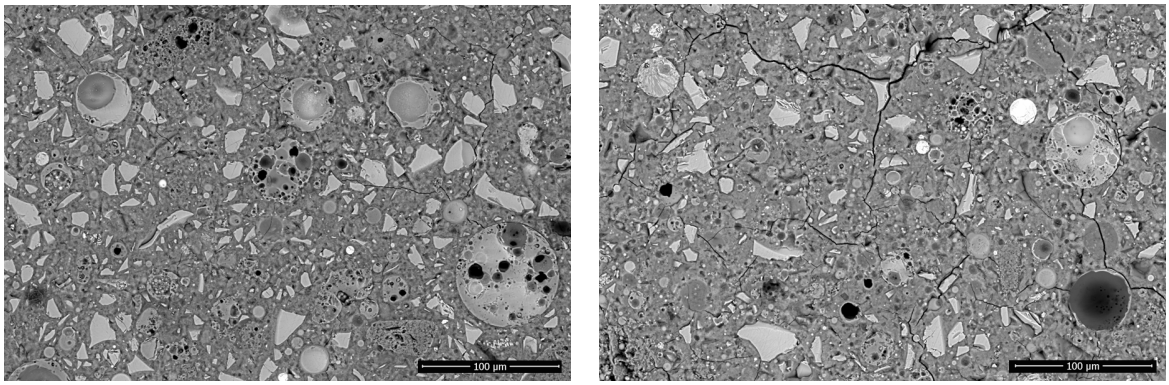

(a) SEM image of S70N4T7

(b) SEM image of S50N5T3

Figure 4.35: SEM images of S70N4T7 and S50N5T3 with accelerating voltage of 15 kV, magnitude of 1000 and 10 mm working distance.

Figure 4.36 shows the results of the atomic Na/(Si+Al) and Ca/(Si+Al) ratios for S70N4T7 and S50N5T3. In this case, the S50N5T3 result is more scattered, moreover, the lower atomic Ca/Si ratio is also reflected in this figure, as the S50N5T3 is relatively governing between 0.0 and 0.6 Ca/(Si+Al), having less calcium present.

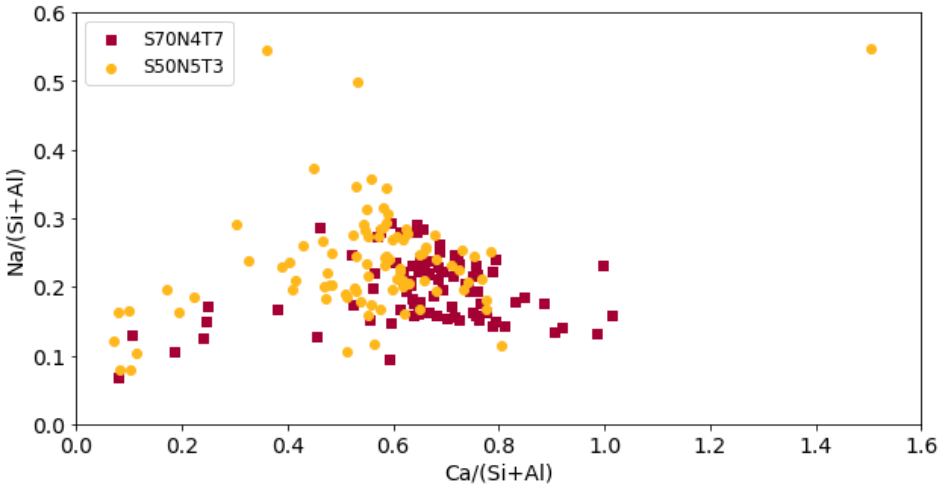

Figure 4.36: 2D scatter plots of EDX point analysis of Na/(Si+Al) and Ca/(Si+Al) ratios for S70N4T7 and S50N5T3

The fact that less calcium is present in the S50N5T3 sample relative to S70N4T7 is also reflected in Figures 4.37a, 4.37b and 4.37d. In addition, it is observed that there is more sodium and silica present in the S50N5T3 system, which is also reflected in Figure 4.37d as a more scattered distribution can be observed with variations between 0.14 and 2.02. For both samples, no linear correlation between Al/Si and Mg/Si is observed, indicating no hydrotalcite-type gel phases are present in this system (Figure 4.37c).

Figure 4.38 illustrates the ternary diagram of S70N4T7 and S50N5T3, following the same method as described in previous section for Figure 4.33. The higher scattering of the normalized Ca/Si ratio for S50N5T3 is again observed, accompanied by a higher presence of sodium in the paste matrix, as reflected by the normalized Na/Si ratio.

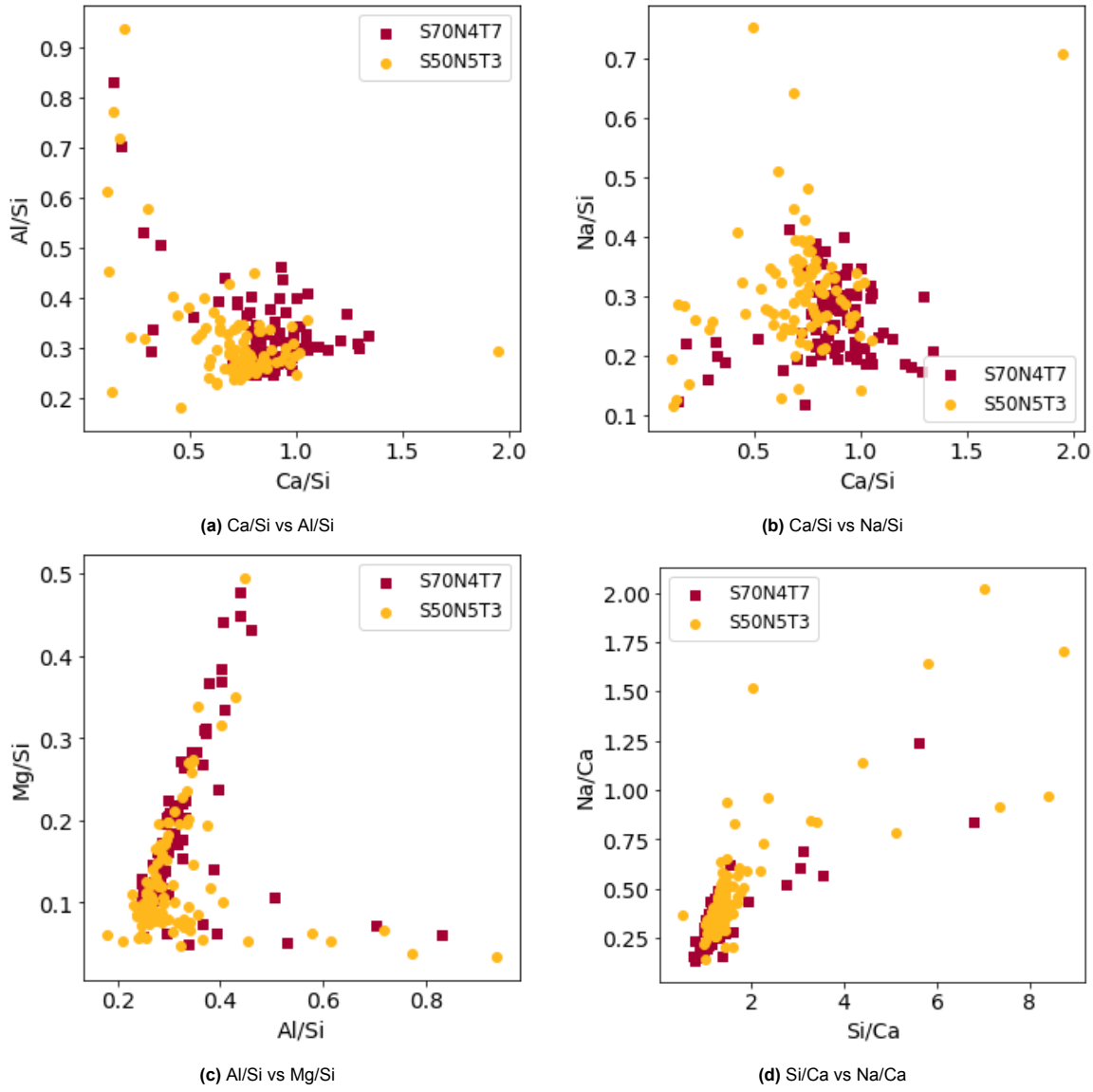

(a) Ca/Si vs Al/Si

(b) Ca/Si vs Na/Si

(c) Al/Si vs Mg/Si

(d) Si/Ca vs Na/Ca

Figure 4.37: Atomic ratios of the main elements in the matrix of the S70N4T7 and S50N5T3

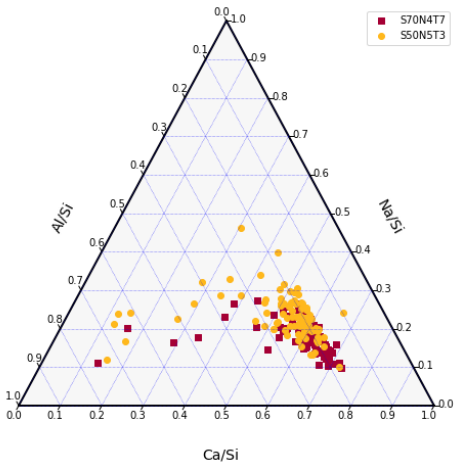

Figure 4.38: Ternary diagram of normalised Ca/Si, Na/Si and Al/Si ratios for S70N4T7 and S50N5T3

5 Discussion

This chapter contains the analysis of results and a discussion on the driving force of drying shrinkage in AAMs. Additionally, it examines the challenges associated with AAMs, reflects on the conducted experiments and analysis, and discusses the novelty of this study.

5.1. Result analysis

In this section, the findings from the performed experiments are combined and discussed. Initially, an examination is conducted on the effects of slag-to-fly-ash ratio, curing time, and activator content. Following this, the correlation between drying shrinkage and mass loss is investigated, along with a discussion on the contribution of external drying shrinkage. Additionally, the comparative results from Sections 4.5 and 4.6 are taken into account. Finally, the development of compressive and flexural strength is discussed.

5.1.1. The effect of slag-to-fly-ash ratio

This section combines the role of the slag-to-fly-ash ratio to drying shrinkage, weight loss, compressive strength, flexural strength, porosity and the pore size distribution. For this analysis, only the samples with 4 wt.% Na_2O content are considered to keep the comparison clear.

The trends in drying shrinkage and weight loss show an increase when the GGBFS content in the mixtures is decreased, observed at 3, 7, and 14 days of curing. After 28 days of curing, the drying shrinkage strain remains the same, while the weight loss for mixtures with lower GGBFS content is at least 1.86 times larger. Although a similar trend is observed for different slag-to-fly-ash ratios, there is no clear linear relationship between drying shrinkage and weight loss. Notably, despite exhibiting the same drying shrinkage strain after 28 days, variations in weight loss suggest that decreasing GGBFS content increases the free water content, leading to more weight loss. This observation aligns with previous research [53]. As highlighted in the literature review, the drying shrinkage of blended AAMs a characterized by a competing mechanism between pore size distribution and stiffness [40]. It is proposed that after 28 curing days, the geopolymerization process in all mixtures is more advanced, and the formed hydration products are more resistant to the drying shrinkage strain. In the S100 mixture, the higher stiffness of calcium-rich reaction products provides an advantage. On the other hand, the more porous structure of S50 mixtures after 28 days is beneficial for drying shrinkage, allowing water to evaporate from larger pores and causing lower capillary tensile stresses.

With an increasing GGBFS content, a decrease in porosity and refinement of the pore size distribution was found, this refinement is best visible after 3 days of curing (see Figure 4.19). The matrix becomes denser because more reaction products are created, this is also found by Lee *et al.* and Nedeljković *et al.* [58, 60]. However, as mentioned, less drying shrinkage is observed for mixtures with higher amount of slag. This finding is in line with research of Marjanović *et al.*, but in contrast to the research of Wang *et al.* [8, 53].

In this study an significant increase of flexural strength was noted for an increase in GGBFS content from 50% to 100%. The compressive strength results show no direct relationship to the GGBFS content, as the outcomes show approximately equal strengths for different GGBFS contents (see Figure 4.2). Additionally, a stagnation of compressive strength development was observed after 28 days comparing the different mixtures. Similar results are documented in the study of Yazdi *et al.*, where an increasing development of flexural strength was observed, whereas the compressive strength does not increase further [69]. An equivalent compressive strength development was also observed in the study of [15]. This result is in contrast with reported findings of Marjanović *et al.*, where samples with higher GGBFS content showed higher compressive strengths [8].

In summary, increasing the GGBFS content in AAMs with 4 wt.% Na_2O content leads despite reduction of porosity and higher volume of medium capillaries to reduction in weight loss and drying shrinkage. This suggests that factors beyond traditional parameters, such as the type of gels formed, may influence the drying shrinkage behavior.

5.1.2. The influence of curing time

This section assembles the findings related to the influence of curing time for AAMs in terms of drying shrinkage, weight loss, porosity, pore size distribution, compressive and flexural strength.

For all mixtures, longer curing times resulted in an increase of compressive and flexural strength. This increase was not observed for the S70N5 mixture where a stagnation after 14 days was measured. In general, longer curing times are related to increase in flexural and compressive strength, which is also documented in literature, due to formation of more and better developed hydration products.

The relative decrease in porosity for the 100% and 70% GGBFS mixtures was similar to each other with a changing curing time, while the decrease in porosity of the 50% GGBFS mixture was less. This may be due to the observation that the pore size distribution of the S50 mixture had to further refine before the total porosity decreased.

The drying shrinkage strains of the mixtures decreased between 69% and 47% when the curing time increased from 3 to 28 days for 56 days of exposure to 50% RH. This while Figure 4.18 showed that the proportion of external drying shrinkage increases substantially with longer curing times. This applies the other way for autogenous shrinkage, which decreases significantly when longer curing times are applied. In addition, to the external drying shrinkage, less weight loss was observed for longer curing times.

To summarize, less drying shrinkage and susceptibility to loose water is noted for the mixtures when longer curing times are considered, while the relative reduction of porosity of mixtures with 100% and 70% was constant. In addition, the flexural and compressive strength increased with a minimum of 26 and 34%.

5.1.3. The effect of activator content

In this section, the findings related to the effect of an increase in Na_2O content are analysed. According to the literature, a higher activator content leads to an intensified degree of chemical reactions during the hydration process. This accelerates the formation of more complete hydration products and restricts the availability of free water. This restricted availability of free water is reflected in the weight loss results, showing a significant decrease while maintaining relatively consistent drying shrinkage behavior. However, the mixtures with a 5 wt.% Na_2O content displayed slightly higher drying shrinkage.

Previous research shows that an increase in activator content results in higher drying shrinkage magnitudes [16, 21, 53, 64]. These studies associate the increase in drying shrinkage with an intensified hydration process, resulting in a denser pore structure due to the formation of more space-filling gel. This leads to a reduction in porosity and a lower quantity of mesopores in the matrix. In addition, Thomas *et al.* noticed an increase in drying shrinkage while increasing the activator content for mixtures with 100% GGBFS, resulting from to the increase of pore refinement and reduction in total porosity [11].

The flexural strength generally decreased for higher activator contents, except for the measurement after 3 days of curing, which showed an increase in strength. In contrast, the compressive strength increased for all mixtures and curing times for higher activator contents. A similar observation was documented by the study of Sun *et al.* [70]. The results are in contrast to Aydin *et al.*, where an increase in both compressive as flexural strength was noted for increase in alkali content [64].

The only measurement of porosity and pore size distribution with a higher activator content (S50N5T3) showed significantly lower porosity compared to the S50N4T3 mixture. This reduction in porosity is also reflected in the differential pore size distribution (Figure 4.25), because the volume of medium capillaries drastically decreased. The refinement of the pore structure using higher activator content is also observed in other studies [16, 53].

In conclusion, differences in activator content provided approximately the same drying shrinkage strains. However, lower activator contents resulted in higher weight losses, increased porosity, and a higher volume of medium capillaries. This indicates that the drying shrinkage strain is not only dependent on the amount of water that can evaporate.

5.1.4. Correlation between drying shrinkage and mass loss

The findings on the correlation between drying shrinkage and weight loss revealed that, in all instances, the mixtures exhibited greater shrinkage and increased weight loss compared to PC. This aligns with the conclusions drawn in previous studies [17, 60]. In line with this, the pore size distribution is significantly more refined and corresponding total porosity is reduced, which is more refined when silicates are present in the activator [71]. When silicates are present in the matrix, more silica-rich gels can be created that show pore filling characteristics. The higher drying shrinkage of AAMs may be attributed due to higher internal capillary stresses built up in the matrix due to this pore refinement, which is also emphasized by Lee *et al.*[60]. However, the results show that the samples with lowest porosity also presented the lowest drying shrinkage and weight loss, proving that the drying shrinkage of AAMs is not directly related to the water loss. This is emphasized by Figure 4.15, where mixtures with higher activator content were less prone to loose water under equal magnitude of drying shrinkage. Additionally, increasing after 28 days of curing time, the drying shrinkage was observed as consistent for mixtures with different GGBFS contents, while the weight loss was significant different.

The results presented in Section 4.2 are in line with all literature, as the drying shrinkage magnitude and weight loss are not directly related in AAMs. Comparison between the different mixtures show that the weight loss also may be related to the amount of reaction products available in the gel matrix. As Figures 4.13 and 4.14 demonstrated that the samples with more GGBFS contain higher amounts of reaction products, which are less sensitive to loose water. Therefore, this gives an indication that the weight loss is related to the amount of reaction products present in the AAMs.

From the results in this study, it can be concluded that the drying shrinkage of AAMs is related to other variables besides water loss and pore structure.

5.1.5. Contribution of external drying shrinkage

The results revealed that in all cases, the extent of external drying shrinkage relative to autogenous shrinkage increases when longer curing times are considered. Moreover, the external drying shrinkage and autogenous shrinkage results showed that an increase in curing time, decreased the proportion of measured autogenous shrinkage in AAMs. Moreover, an increase in GGBFS content leads to a higher proportion of autogenous shrinkage, which finding is in line with reported results of Li *et al.* [72].

5.1.6. Correlation of pore and gel characteristics on the drying shrinkage mechanism

This section discusses the results of both comparative studies of Sections 4.5 and 4.6. The starting point of both analysis is that the pore size distribution and corresponding total porosity measured by MIP of the samples is the same. The samples used to determine the chemical composition and volume of the reaction products were made in the same badge in which specimens were made for MIP,

implying that the pore size distribution and porosity are the same for this experiment. In addition, these properties are also considered as equal during the flexural and compressive strength tests. Regarding the drying shrinkage and weight loss results presented in Figures 4.28 and 4.34, the porosity and pore size distribution are the same at the time of exposure, which is shown in the graphs at the time equal to zero.

Analysis of S100N4T3 and S70N4T14 results

In Figure 4.28, it was demonstrated that the drying shrinkage strain of S100N4T3 is considerably larger than S70N4T14 after 56 days of exposure time, while the weight loss is 39% lower. Despite the fact that the S70N4T14 sample lost significantly more water, the drying shrinkage was always lower than the S100N4T3 sample. The large weight loss relative to the external shrinkage is even better proven with Figure 4.29, because after 28 days the difference between the external drying shrinkage is not so large. The external drying shrinkage of the cementitious and alkali-activated materials is due to water loss to the environment. In other words, the measured weight loss directly correlates with the external drying shrinkage. This explains the higher drying shrinkage strain in S100, despite its lower weight loss. The S100 mixtures exhibit significant early-age autogenous shrinkage, which does not contribute to the measured weight loss.

The analysis of the chemical composition of reaction products is based on the main elements of the blended AAMs, including the atomic Ca/Si, Al/Si, Na/Si and Mg/Si ratios, respectively, this approach is in line with previous studies [8, 18]. In terms of the results of the chemical composition, both atomic Ca/Si and Na/Si ratios were higher for S100N4T3 samples, including a higher amount of reaction products (70.1% versus 59.5%). Figures 4.31, 4.32 and 4.33 revealed that the distribution of S100N4T3 was more homogeneous, which can be dedicated to the higher amount of GGBFS present resulting in production of more 2D layered C-A-S-H gel and higher atomic Ca/Si ratio, this is also observed in the studies performed by [8, 73].

In addition, the linear dependence between Mg/Si and Al/Si was shown, indicating the presence of hydrotalcite-type of reaction products, this dependency is described and supported by previous research [74]. Moreover, the positive intersection with the x-axis for the trendline of S100N4T3 reflects the level of Al incorporation in the C-S-H gel [73, 74]. Furthermore, the slope of the trendline was equal to 1.95, representing the atomic ratio of Mg/Al in the secondary gel, which is in line with previous documented values [8, 73, 74]. The hydrotalcite-type of gel is likely intimately intermixed with C-A-S-H gel on a nano- or micrometer level, when the MgO content of unreacted GGBFS is larger than 5% [8, 75].

While the pore size distribution and porosity at moment of exposure was equal, is the drying shrinkage of S100N4T3 significant higher. Based on the findings, it is indicated that the combination of the higher amount of reaction products, more homogeneous distribution of reaction products, and more C-A-S-H gel represented by the higher Ca/Si ratio is causing more contraction of the paste resulting in more drying shrinkage. This is indicating that drying shrinkage is not about the amount of gel present in the system, but about the type of gel.

Analysis of S70N4T7 and S50N5T3 results

In this section, the analysis focuses on the results obtained from samples S70N4T7 and S50N5T3. The results of both drying shrinkage and weight loss, indicate a consistent increase for the S50N5T3 sample in both scenarios (Figure 4.34). Examining these outcomes from the perspective of sample age reveals a consistent correlation, with the weight loss and drying shrinkage consistently higher for the S50N5T3 sample. Therefore, in this analysis, the sample exhibiting the highest weight loss also demonstrates the highest drying shrinkage strain.

Regarding the chemical composition, the lower GGBFS content of S50N5T3 is reflected in the lower atomic Ca/Si ratio, therefore, less C-A-S-H gels can be formed than in S70N4T7. Moreover, the increased Na_2O-content from 4 to 5 wt.% combined with the same activator modulus, implies that there is also more silicate present in the matrix coming from the used waterglass solution in the activator. The increased presence of sodium is reflected in the atomic Na/Si ratio increasing from 0.26 to 0.29, but also in Figures 4.37b and 4.37d. In the first figure, the distribution of S50N5T3 points is wider spread

than S70N4T14 along the vertical axis, additionally, the lower atomic Ca/Si ratio is also reflected. In the latter, the increased availability of silicate and sodium is clearly visible, as the points are both more distributed and containing of higher values.

Combination of these results show that mixtures with higher availability of both silicate and sodium increase the rate of drying shrinkage. The study of Melo Neto *et al.*, also emphasized the influence of increased drying shrinkage for mixtures where higher contents of silicate were available [16].

5.1.7. Compressive and flexural strength development

In the previous sections, no clear relationship between curing times, slag-to-fly-ash ratios, and compressive strength development was found. Furthermore, the compressive strengths observed in this study did not reach high levels, unlike the results reported in previous studies [57, 76], however, they were higher compared to PC.

During the experiments, brittle behaviour of the mixtures was observed in compressive strength testing, as indicated in Figures B.1 of Appendix B. This brittle behaviour aligns with findings in studies by Duran Atiş *et al.*, Nedeljković *et al.* [71, 76]. While the first study observed different behaviour for different types of activator, this variability was not observed in this study, where the combination of waterglass and sodium hydroxide was consistently used. Besides the brittle behaviour, AAMs showed variations in both flexural and compressive strengths when different types of activators were used [71]. The latter study suggested that this behaviour resulted from the combined influence of low porosity and densely packed grains, especially in high-calcium based binder systems.

Figure 5.1 illustrates the relationship between compressive and flexural strength for different types of alkali-activated concretes, including the relationship of PC concretes indicated with ACI 318-02 [12]. The legend provides clarity on the representation of results from this research. The results in Figure 5.1 cannot be directly compared, because the data of this study is paste, and the data points in the graph represent concrete. However, considering that the strength of cement paste is considered the weakest link in concrete due to much stronger aggregates, the graph provides an idea of the results relative to the lower limit of concrete, as also done in the research by Marjanović *et al.* [8]. From the figure, it is evident that the ratio between flexural and compressive strength for this study are not comparable with PC, especially the mixtures with 100% and 70% GGBFS content. This is in line with findings of previous researchers, however, it is possible to create a mixture with an equal ratio between these strengths.

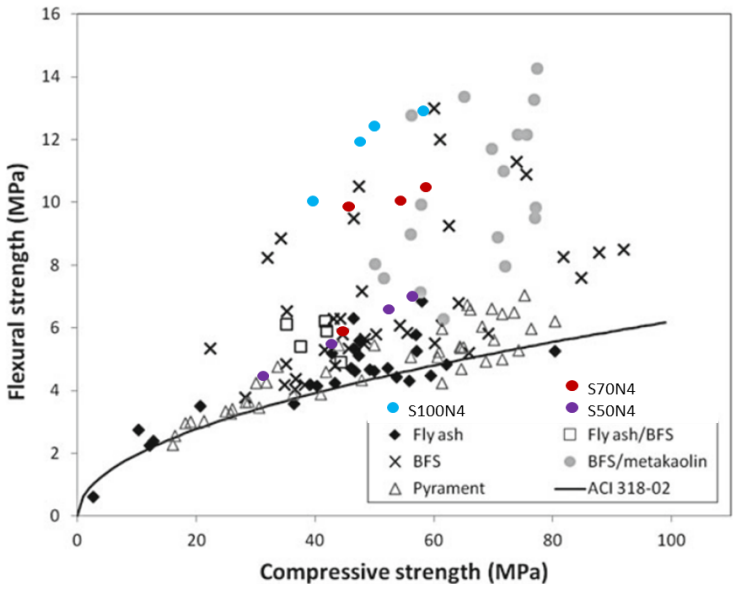

Figure 5.1: Relationship between compressive and flexural strength for different types of alkali-activated concretes, including the relationship of PC concretes indicated with ACI 318-02 [12], including results from this research.

5.2. Drying shrinkage in AAMs: the driving force

This section focuses on the driving force of drying shrinkage in AAMs, combining insights from both the literature and the experimental results presented in this study. Understanding the driving force is crucial for accurately predicting drying shrinkage. As thoroughly examined in the literature review (section 2.2), drying shrinkage is associated with the loss of free water to the environment when exposed to lower RH and water loss due to the internal hydration process. Drying shrinkage is affected by the pore size distribution and gel characteristics present in the microstructure, with various mix design parameters (precursor type and amount, activator type, content and modulus, curing conditions) applying a significant influence on both pore size distribution and gel characteristics, thereby impacting drying shrinkage.

As mentioned in the literature review, the capillary pressure theory is considered the most common driving force for drying shrinkage in cementitious materials around 50% RH. Capillary stresses develop due to the loss of free water through evaporation, forming a meniscus. The evaporation of water starts in the largest pore sizes and continues until a new meniscus is formed in pore sizes equal to the Kelvin radius (equation 2.4). In this equilibrium condition, all pores smaller than the Kelvin radius are completely filled with water [13]. According to the Kelvin-Laplace equation, the magnitude of shrinkage strain that develops is dependent on the pore size distribution, as also noted by Kovler *et al.* [49]. More refined pore size distributions are observed in this study, resulting in higher drying shrinkage magnitudes for AAMs relative to PC. These results are consistent with previous studies [11, 13, 17–19, 49]. Moreover, mixtures with more slag contained higher amounts of small isolated and medium capillaries compared to mixtures with incorporated fly ash.

The first part of the study focuses on the influence of mix design parameters -slag-to-fly-ash ratio, curing time and activator content- on the drying shrinkage, weight loss, total porosity and pore size distribution of AAMs. The influence of these mix design parameters is examined separately in Sections 5.1.1, 5.1.2 and 5.1.3. In summary, mixtures with higher slag-to-fly-ash ratios, longer curing times and higher activator content exhibit more refined pore size distributions, resulting in less weight loss and lower or equal drying shrinkage magnitudes. The increased slag content, prolonged curing times and higher activator content promote the hydration process and geopolymerization, leading to a higher degree of chemical reactions and reactivity, resulting in more complete hydration products. Consequently, more refined pore size distributions are associated with a higher amount and more complete hydration products when these mix design parameters have higher values. Moreover, more water is chemically bound to the formed hydration products, reducing the amount of free water available for evaporation. The results align with previous research, as finer pores contain less water that can evaporate, and the water is more resistant to evaporation [13, 16, 17, 19]. Relating the observed results to the Kelvin-Laplace equation, it is expected that capillary tensile stresses that develop in the paste matrix should be higher for more refined pore structures. Assuming this correlation is valid in AAMs, it is suggested that other driving forces exist to explain the lower drying shrinkage strain, specifically in this study, the influence of gel characteristics.

The second part of this study focuses on correlating pore and gel characteristics with the drying shrinkage mechanism. By controlling the pore size distribution, the contribution of gel characteristics in different mixtures is investigated. The detailed comparisons are discussed in Sections 4.5 and 4.6. Despite equal pore size distributions at the beginning of the drying process, distinct drying shrinkage magnitudes are observed, providing an alternative perspective that emphasizes that pore size distribution is not the primary driving force behind the drying shrinkage.

The combined insights from both parts of this study suggest that pore characteristics are not the primary driving force behind drying shrinkage in AAMs. Instead, gel characteristics play a crucial role as a driving force in the drying shrinkage mechanism. These gel characteristics include the type of hydration products and the degree of hydration, which depend on mix design parameters. Consequently, the magnitude of the driving force is not predetermined but variable. For example, an increased quantity of slag raises the amorphous content of the mixture, providing more amorphous calcium and silicon to react. These chemical substitutes fill up pores and produce higher amounts of reaction products, resulting in a lower drying shrinkage strain. Therefore, the drying shrinkage mechanism is chemically influenced rather than physically.

5.3. Challenges of AAMs

Due to their potential to reduce environmental impact by utilizing industrial by-products, offering sufficient strength development, and demonstrating good resistance in aggressive environments, AAMs are viewed as a promising alternative to PC. While this study specifically highlighted the challenge of drying shrinkage behavior in AAMs, it is important to address additional issues before AAMs can be considered a marketable product.

The availability of GGBFS and FA from the industry presents another potential limitation. In the Netherlands, GGBFS accessibility is relatively high due to the presence of large steel plants, though this may change due to sustainability regulations. Yet, this situation may not apply universally across the globe, and AAMs could remain a valuable material. Utilizing by-products from existing industries is environmentally beneficial, preventing these materials from ending up in landfills. While challenges persist, these issues also present opportunities for research and innovation in the field of AAMs, aiming to develop solutions that enhance their feasibility and sustainability on a global scale.

In terms of the binder manufacturing process, several additional steps are required, particularly concerning safety and activation. Unlike PC, which easily binds with water, AAMs demand high alkali solutions for precursor activation. The choice of activator requires advanced preparation, often 24 hours in advance. Given the high pH and release of harmful fumes during activator preparation, safety precautions, including wearing protective clothing during mixing, must be carefully considered. While these precautions can be effectively implemented in a research lab, the scale-up for large-scale AAM production poses significant challenges, requiring entire concrete plants to be converted for safe operation.

Another notable challenge is the low setting time affecting the workability, especially for high-calcium based binder systems. While casting the samples for this study, it was observed that higher slag content reduces the available working time. This limitation is further evident in the determination of the final setting time (Table 4.1), which is also documented in previous research [76]. Despite the seemingly long setting time, the ability to work with 100% GGBFS paste reduces within 15 minutes, demanding a rapid operating speed. However, the addition of fly ash can extend the setting time sufficiently to allow proper casting and compaction of the alkali-activated specimens. The short setting time of AAMs could be advantageous for the precast industry, allowing for more frequent mold utilization. However, it may pose challenges for in-situ concrete applications.

The short setting time of AAMs could be advantageous for the precast industry, allowing for more frequent mold utilization. However, it may pose challenges for in-situ concrete applications.
While PC and alkali-activated concrete may appear similar, significant differences make direct comparisons challenging. Unlike PC concrete, which requires a mixture of water and cement for binder formation, AAMs involve additional factors such as the choice of raw materials, type of activator, activator content, and curing conditions, making their production more complex. Applying principles established for PC to AAMs, as demonstrated in this study with drying shrinkage, presents challenges. Determining factors influencing drying shrinkage in PC, such as water availability, have less guidance in AAMs. Additionally, directly employing formulas like the Kelvin-Laplace equation is challenging, as it has been observed that the amount of water loss does not correspond directly to the stresses measurable in experiments. Nevertheless, using such formulas provides a solid starting point, allowing researchers to adjust the research direction. It is crucial to always bear in mind the distinctions between PC and AAMs and use each material where its properties are most applicable.

5.4. Reflections on experiments and analysis

The process of making choices and navigating the course of research can take various routes, leading to the same endpoint. In this thesis, decisions were grounded in accumulated knowledge from the literature, weighing specific relevance and feasibility. Prior to starting the experiments, it was essential to clarify the research objectives. This thesis set out to control one of the fundamental parameters - gel characteristics or pore structure. To enhance the likelihood of success, variations were introduced not only in the quantities of raw materials and curing times but also in the activation content. How-

ever, insufficient attention was given to the time required for the measurements across all experiments. Nonetheless, this approach yielded a comprehensive dataset encompassing drying shrinkage, weight loss, compressive, and flexural strength by the end of this study.

Being adaptive and contemplating the next steps is essential before undertaking certain experiments. While charting the course, you consider certain limitations an experiment might have, but you only truly discover them when conducting the experiments. For example, the requirement that specimens must be 100% free of water before conducting MIP or SEM-EDX, necessitating a waiting period of more than 3 weeks in the vacuum freeze dryer to ensure this due to the extremely small pores in the alkali-activated materials. Additionally, the results obtained from experiments are often open to interpretation from various perspectives or come with certain limitations. However, an effort has been made to display as consistently as possible all results. Limitations regarding the performed experiments are specifically apparent for MIP and SEM-EDX. The range of mercury in MIP experiments has a limitation because it cannot detect pore sizes smaller than 0.006 μm, additionally to the ink bottle effect, however, this experiment did provide an accurate insight into the small isolated and medium capillaries. In this study, overlap was found in the pore structure in the designed manner, however, if this difference had been too small it would be an option to also look at N_2 adsorption, as smaller pores can be detected using that experiment. As for the SEM pictures taken and EDX analysis performed, there should be an understanding that anything larger and smaller than this magnification cannot be seen. It gives one an impression of the AAMs at that level in a specific spot, while at larger or smaller magnifications or in other places there is a chance to see other things as well. Therefore, wide range of images and point analysis are made of different small fragments of the paste, to get as good and average a result as possible.

The results of the pore structure analysis and selection form the basis of the analysis of the final conclusion. It should be noted that these results represent the porosity and pore size distribution of the moment that the mixtures were exposed to drying shrinkage and weight loss. However, what is also illustrated in this study is that the pore structure is refining and therefore changing over time. On the other hand, the same applies for the results about the chemical composition and amount of reaction products, because the same samples were used for MIP and SEM-EDX. Therefore, it gives an indication on what is governing.

As previously mentioned, the complexity of AAMs arises from numerous input parameters in the binder system, making direct connections challenging. It necessitates a comprehensive approach, thoroughly examining each aspect within the broader context. In this study, a thorough examination was undertaken, aligning and comparing all results before drawing conclusions. The interpretation of findings is intricate, given the interconnected nature of variables, especially when consolidating results from comparative studies. It is important to highlight that the analysis of S70N4T7 and S50N5T3 involved variations in all considered parameters, introducing complexity to result interpretation. Therefore, it is necessary to revert to the initial goal of this approach, which focused on controlling pore size distribution and porosity.

5.5. Novelty of research

This study stands out for its approach to unravel the drying shrinkage mechanism in AAMs. In addressing the challenges associated with AAMs, this study introduces a fresh approach that prioritizes a thorough understanding of the root causes over symptom mitigation.

A distinguishing feature of this research is the careful decomposition of parameters. Rather than considering the system as a whole, the research systematically isolates and examines individual parameters. This nuanced approach allows for close examination and sheds light on complex interactions that may remain hidden when considering the system as a whole. Breaking down complex relationships into their constituent elements leads to a deeper understanding of the mechanism of drying shrinkage in AAMs.

A major contribution of this research lies in the creation of a comprehensive data set. By strictly adhering to consistent methodologies and carefully considering critical input parameters, the study has

collected a comprehensive set of data on drying shrinkage and weight loss. This dataset not only serves as a valuable resource for future research, but also ensures the reliability and comparability of results under different experimental conditions.

In essence, this research deviates from conventional problem-solving approaches and provides a nuanced understanding of the drying shrinkage behavior of AAMs, adpoting a component-focused analysis. By prioritizing the investigation of origins, decomposing parameters and assembling a comprehensive data set, this research represents an important step forward in the investigation of alkali-activated materials.

6

Conclusion and recommendations

The aim of this thesis is to advance the understanding of the drying shrinkage mechanism in AAMs, by considering the pore and gel characteristics. The influence of differences in the gel composition are identified while controlling the pore size distribution and total porosity at the moment of exposure to lower RH. The study has been divided into three objectives to achieve the main goal:

1. To investigate the impact of mix design parameters, such as slag-to-fly-ash ratio, curing time, and Na_2O wt.% content, on drying shrinkage behavior and mechanical properties of alkali-activated materials, aiming to comprehend their influence on pore structure and gel characteristics.
2. To study how mix design parameters affect the microstructure development of alkali-activated materials, aiming to reveal microstructural changes contributing to drying shrinkage.
3. To attain a fundamental understanding of the drying shrinkage mechanism by conducting a detailed analysis of pore structure and gel characteristics in alkali-activated materials, to identify the primary parameter influencing the mechanism.

In this chapter, an overview and summary of the results is presented. Based on this, the conclusion is drawn based on the objectives. Finally, recommendations for future research are suggested.

6.1. Conclusion

From the results of this study, it can be concluded that the drying shrinkage of blended alkali-activated slag and fly ash pastes is related to other factors beyond water loss and pore structure, unlike the observed correlation in PC.

In the examination of the influence of the slag-to-fly-ash ratio on both microstructure development and drying shrinkage it was found that with increasing GGBFS content, the drying shrinkage magnitude and weight loss decreased, as well as the total porosity reduced. Additionally, an increase in small isolated and medium capillaries was observed. The refinement of the pore sizes would suggest that the capillary stresses in the matrix increase resulting in a higher magnitude of drying shrinkage. However, this cannot be concluded from this study. Moreover, it can be inferred that the proportion of external drying shrinkage increases for mixtures with lower GGBFS content.

Longer curing times help to form a more complete and larger amount of hydration products, which makes the pore structure more refined, so both less drying shrinkage and weight loss have been documented. Comparison between mixtures with 100% and 50% GGBFS content showed after 28 days of curing equal drying shrinkage magnitudes, while more weight loss was documented for mixtures with lower amounts of GGBFS. Moreover, better flexural and compressive strength is been noticed, especially monitored for mixtures with 50% GGBFS content. Furthermore, the proportion of external drying shrinkage increases with longer curing times. This is evident as the degree of autogenous shrinkage decreases over time due to the formation of more reaction products, resulting in a decreasing proportion of autogenous shrinkage.

An increase in activator content results in a more refined pore structure due to enhanced geopolymerization. This leads to a decrease in total porosity, less weight loss, and higher compressive strengths. Despite the drying shrinkage magnitude remaining relatively constant over the 56 days of exposure, a decrease in flexural strength was observed. It can be concluded that the considered difference in Na_2O content has no significant effect on the drying shrinkage behavior.

Regarding the most significant fundamental parameter, based on the mixtures chosen in this study, an overlap of pore structure at the moment of exposure to drying was observed twice. Both comparisons revealed that gel characteristics govern drying shrinkage rather than pore size distribution. The first comparative study between S100N4T3 and S70N4T14 showed that the mixture with more homogeneous reaction products, a higher atomic Ca/Si ratio, and more C-A-S-H gel exhibited more drying shrinkage, indicating that the contraction of this type of reaction product caused an increase in drying shrinkage while less water was lost. Additionally, at the moment of exposure, the type of gel is of greater importance than the amount of gels present in the paste matrix because the mixture with more reaction products exhibited more drying shrinkage. The second comparative study between S70N4T7 and S50N5T3 indicated that the amount of sodium and silicate available from the activator to form reaction products greatly influences drying shrinkage, leading to a significant increase.

In conclusion, the comprehensive findings of this study indicate that gel characteristics have an essential role as a driving force in the drying shrinkage mechanism. This study confirms that the drying shrinkage performance of AAMs is strongly related to the microstructure, especially the activator content used and the type of reaction product created by the combination of precursors and activators. Gel characteristics are closely linked to mix design parameters, significantly influencing the mechanism and, consequently, the drying shrinkage magnitude of moderate- and high-calcium based binder systems. Notably, the drying shrinkage mechanism is primarily influenced by chemical influences rather than physical ones. However, more research is needed, specifically on the reaction products, to facilitate the practical implementation of AAMs in the construction industry.

6.2. Recommendations

Some recommendations are stated for future research on the drying shrinkage mechanism of AAMs:

- To extent the range of mix design parameters, by studying the effect of different types and/or combinations of activators, or using other types and blends of precursors, to evaluate the findings of this study.
- To take the dynamic process of pore size development into account, by determining the pore size distribution after specified amount or time of drying.
- To evaluate the influence of drying on the exposed pore structure of AAMs.
- To determine the reaction speed of raw materials and various mixtures to evaluate its impact to drying shrinkage.
- To determine the pore size distribution of the considered mixtures using N_2 adsorption, because smaller range of pores can be measured using this technique.
- To consider longer curing times to create more complete hydration products, as AAMs need more time to develop a stable microstructure. Moreover, evaluate the extent on pore refinement, reduction in porosity, compressive and flexural strength development on drying shrinkage behaviour. Additionally, this helps to determine when the drying shrinkage of AAMs will stop increasing further, as this was not observed yet in this study.
- To determine if variations in external and internal RH affect the mechanism of drying shrinkage, as the external RH in this study was kept constant, while its influence is extensively documented

in literature. Moreover, the internal RH can change when different mixtures are considered, resulting in differences in internal stresses. This needs further research, as this study found that a finer pore structure can also lead to less shrinkage. Considering the internal RH can show whether the capillary pressure theory is the correct assumption.

- To investigate the cracking potential related to drying shrinkage, as drying shrinkage does not always have to be a problem, as long as the phenomena is counteracted by creep/relaxation, as no cracking will occur that can structurally deteriorate the material. This includes determining the material's modulus of elasticity.

References

[1] P. C. Aïtcin, "Cements of yesterday and today: Concrete of tomorrow," *Cement and Concrete Research*, vol. 30, no. 9, pp. 1349–1359, Sep. 2000, ISSN: 0008-8846. DOI: 10.1016/S0008-8846(00)00365-3.

[2] P. Kumar Metha and P. Monteiro, *Concrete: Microstructure, properties and materials*. McGraw-Hill, 2006. DOI: 10.1036/0071462899.

[3] K. L. Scrivener and R. J. Kirkpatrick, "Innovation in use and research on cementitious material," *Cement and Concrete Research*, vol. 38, no. 2, pp. 128–136, Feb. 2008, ISSN: 00088846. DOI: 10.1016/j.cemconres.2007.09.025.

[4] J. Rogelj, M. Den Elzen, N. Höhne, T. Fransen, H. Fekete, H. Winkler, R. Schaeffer, F. Sha, K. Riahi, and M. Meinshausen, *Paris Agreement climate proposals need a boost to keep warming well below 2 °c*, Jun. 2016. DOI: 10.1038/nature18307.

[5] J. Lehne and F. Preston, *Making Concrete Change: Innovation in Low-carbon Cement and Concrete*. The Royal Institute of International Affairs, 2018, ISBN: 9781784132729. [Online]. Available: www.chathamhouse.org.

[6] J. L. Provis, "Alkali-activated materials," *Cement and Concrete Research*, vol. 114, pp. 40–48, Dec. 2018, ISSN: 0008-8846. DOI: 10.1016/J.CEMCONRES.2017.02.009.

[7] I. Garcia-Lodeiro, A. Palomo, and A. Fernández-Jiménez, "An overview of the chemistry of alkali-activated cement-based binders," in *Handbook of Alkali-Activated Cements, Mortars and Concretes*, Elsevier Inc., 2015, pp. 19–47, ISBN: 9781782422884. DOI: 10.1533/9781782422884.1.19.

[8] N. Marjanović, M. Komljenović, Z. Baščarević, V. Nikolić, and R. Petrović, "Physical-mechanical and microstructural properties of alkali-activated fly ash-blast furnace slag blends," *Ceramics International*, vol. 41, no. 1, pp. 1421–1435, 2015, ISSN: 02728842. DOI: 10.1016/j.ceramint.2014.09.075.

[9] J. L. Provis and S. A. Bernal, "Geopolymers and related alkali-activated materials," *Annual Review of Materials Research*, vol. 44, pp. 299–327, 2014, ISSN: 15317331. DOI: 10.1146/annurev-matsci-070813-113515.

[10] F. Jin, K. Gu, and A. Al-Tabbaa, "Strength and drying shrinkage of reactive MgO modified alkali-activated slag paste," *Construction and Building Materials*, vol. 51, pp. 395–404, Jan. 2014, ISSN: 09500618. DOI: 10.1016/j.conbuildmat.2013.10.081.

[11] R. J. Thomas, D. Lezama, and S. Peethamparan, "On drying shrinkage in alkali-activated concrete: Improving dimensional stability by aging or heat-curing," *Cement and Concrete Research*, vol. 91, pp. 13–23, Jan. 2017, ISSN: 0008-8846. DOI: 10.1016/J.CEMCONRES.2016.10.003.

[12] J. L. Provis and J.S.J. van Deventer, *Alkali Activated Materials: State-of-the-Art-Report, RILEM TC 224-AAM*. Dordrecht, 2014, vol. 13, ISBN: 978-94-007-7671-5. DOI: 10.1007/978-94-007-7672-2. [Online]. Available: http://www.springer.com/series/8780.

[13] H. Ye, C. Cartwright, F. Rajabipour, and A. Radlińska, "Understanding the drying shrinkage performance of alkali-activated slag mortars," *Cement and Concrete Composites*, vol. 76, pp. 13–24, Feb. 2017, ISSN: 09589465. DOI: 10.1016/j.cemconcomp.2016.11.010.

[14] C. Cartwright, F. Rajabipour, and A. Radlińska, "Shrinkage Characteristics of Alkali-Activated Slag Cements," *Journal of Materials in Civil Engineering*, vol. 27, no. 7, Jul. 2015, ISSN: 0899-1561. DOI: 10.1061/(asce)mt.1943-5533.0001058.

[15] X. Gao, Q. L. Yu, and H. J. Brouwers, "Assessing the porosity and shrinkage of alkali activated slag-fly ash composites designed applying a packing model," *Construction and Building Materials*, vol. 119, pp. 175–184, Aug. 2016, ISSN: 09500618. DOI: 10.1016/j.conbuildmat.2016.05.026.

[16] A. A. Melo Neto, M. A. Cincotto, and W. Repette, “Drying and autogenous shrinkage of pastes and mortars with activated slag cement,” *Cement and Concrete Research*, vol. 38, no. 4, pp. 565–574, Apr. 2008, ISSN: 00088846. DOI: 10.1016/j.cemconres.2007.11.002.

[17] Y. Ma and G. Ye, “The shrinkage of alkali activated fly ash,” *Cement and Concrete Research*, vol. 68, pp. 75–82, 2015, ISSN: 00088846. DOI: 10.1016/j.cemconres.2014.10.024.

[18] M. Mastali, P. Kinnunen, A. Dalvand, R. Mohammadi Firouz, and M. Illikainen, “Drying shrinkage in alkali-activated binders – A critical review,” *Construction and Building Materials*, vol. 190, pp. 533–550, Nov. 2018, ISSN: 09500618. DOI: 10.1016/j.conbuildmat.2018.09.125.

[19] F. Collins and J. G. Sanjayan, “Effect of pore size distribution on drying shrinkage of alkali-activated slag concrete,” *Cement and Concrete Research*, vol. 30, no. 9, pp. 1401–1406, 2000.

[20] H. Ye and A. Radlińska, “Shrinkage mechanisms of alkali-activated slag,” *Cement and Concrete Research*, vol. 88, pp. 126–135, Oct. 2016, ISSN: 00088846. DOI: 10.1016/j.cemconres.2016.07.001.

[21] A. Adesina, K. Rajesh Kumar, S. Odeyemi, K. Mahender, S. Das, K. Cyriaque, and K. Cyriaque, “Mitigating of drying shrinkage in alkali-activated slag composites,” in *IOP Conference Series: Materials Science and Engineering*, vol. 981, IOP Publishing Ltd, Dec. 2020. DOI: 10.1088/1757-899X/981/3/032075.

[22] S. Chen, S. Ruan, Q. Zeng, Y. Liu, M. Zhang, Y. Tian, and D. Yan, *Pore structure of geopolymer materials and its correlations to engineering properties: A review*, Apr. 2022. DOI: 10.1016/j.conbuildmat.2022.127064.

[23] C. Shi, A. F. Jiménez, and A. Palomo, “New cements for the 21st century: The pursuit of an alternative to Portland cement,” *Cement and Concrete Research*, vol. 41, no. 7, pp. 750–763, Jul. 2011, ISSN: 0008-8846. DOI: 10.1016/J.CEMCONRES.2011.03.016.

[24] A. Palomo, P. Krivenko, I. Garcia-Lodeiro, E. Kavalerova, O. Maltseva, and A. Fernández-Jiménez, “A review on alkaline activation: New analytical perspectives,” *Materiales de Construccion*, vol. 64, no. 315, Jul. 2014, ISSN: 19883226. DOI: 10.3989/mc.2014.00314.

[25] R. Snellings, G. Mertens, and J. Elsen, *Supplementary cementitious materials*, 2012. DOI: 10.2138/rmg.2012.74.6.

[26] N. B. Winter, *Understanding Cement: An introduction to cement production, cement hydration and deleterious processes in concrete*. WHD Microanalysis Consultants Ltd, 2009.

[27] P. Duxson and J. L. Provis, “Designing precursors for geopolymer cements,” *Journal of the American Ceramic Society*, vol. 91, no. 12, pp. 3864–3869, Dec. 2008, ISSN: 00027820. DOI: 10.1111/j.1551-2916.2008.02787.x.

[28] J. L. Provis and J. S. J. Van Deventer, *Geopolymers: structures, processing, properties and industrial applications*. Cambridge: Woodhead publishing Limited, 2009.

[29] P. Duxson, A. Fernández-Jiménez, J. L. Provis, G. C. Lukey, A. Palomo, and J. S. Van Deventer, “Geopolymer technology: The current state of the art,” *Journal of Materials Science*, vol. 42, no. 9, pp. 2917–2933, May 2007, ISSN: 00222461. DOI: 10.1007/s10853-006-0637-z.

[30] ASTM C618, “Standard specification for coal fly ash and raw or calcined natural pozzolan for use in concrete,” 2019.

[31] S.-D. Wang and K. L. Scrivener, “Hydration products of alkali activated slag cement,” *Cement and Concrete Research*, vol. 25, no. 3, pp. 561–571, 1995. DOI: https://doi.org/10.1016/0008-8846(95)00045-E.

[32] F. Puertas, S. Martínez-Ramírez, S. Alonso, and T. Vázquez, “Alkali-activated fly ash/slag cements. Strength behaviour and hydration products,” *Cement and Concrete Research*, vol. 30, no. 10, pp. 1625–1632, 2000, ISSN: 00088846. DOI: 10.1016/S0008-8846(00)00298-2.

[33] V. Glukhovsky, “Ancient, modern and future concretes,” in *First international Conferene Alkaline Cements and Concretes*, vol. 1, Kiev, Urkaine, 1994, pp. 1–8.

[34] P. Krivenko, “Alkaline cements,” in *First international conference alkaline cements and concretes*, vol. 1, 1994, pp. 11–129.

[35] B. Zhang, H. Zhu, P. Feng, and P. Zhang, *A review on shrinkage-reducing methods and mechanisms of alkali-activated/geopolymer systems: Effects of chemical additives*, May 2022. DOI: 10.1016/j.jobe.2022.104056.

[36] I. García-Lodeiro, A. Fernández-Jiménez, A. Palomo, and D. E. MacPhee, "Effect of calcium additions on N-A-S-H cementitious gels," *Journal of the American Ceramic Society*, vol. 93, no. 7, pp. 1934–1940, Jul. 2010, ISSN: 00027820. DOI: 10.1111/j.1551-2916.2010.03668.x.

[37] M. Criado, A. Fernández Jiménez, I. Sobrados, A. Palomo, and J. Sanz, "Effect of relative humidity on the reaction products of alkali activated fly ash," *Journal of the European Ceramic Society*, vol. 32, no. 11, pp. 2799–2807, Aug. 2012, ISSN: 0955-2219. DOI: 10.1016/J.JEURCERAMSOC.2011.11.036.

[38] B. Zhang, H. Zhu, Y. Cheng, G. F. Huseien, and K. W. Shah, *Shrinkage mechanisms and shrinkage-mitigating strategies of alkali-activated slag composites: A critical review*, Feb. 2022. DOI: 10.1016/j.conbuildmat.2021.125993.

[39] J. L. Provis, R. J. Myers, C. E. White, V. Rose, and J. S. Van Deventer, "X-ray microtomography shows pore structure and tortuosity in alkali-activated binders," *Cement and Concrete Research*, vol. 42, no. 6, pp. 855–864, Jun. 2012, ISSN: 0008-8846. DOI: 10.1016/J.CEMCONRES.2012.03.004.

[40] D. Huang, P. Chen, H. Peng, Y. Yang, Q. Yuan, and M. Su, "A review and comparison study on drying shrinkage prediction between alkali-activated fly ash/slag and ordinary Portland cement," *Construction and Building Materials*, vol. 305, p. 124 760, Oct. 2021, ISSN: 0950-0618. DOI: 10.1016/J.CONBUILDMAT.2021.124760.

[41] M. Nedeljković, K. Arbi, Y. Zuo, and G. Ye, "Microstructural and minerological analysis of alkali-activated fly ash-slag pastes," in *Proceedings of the 3rd International RILEM Conference on Microstructure Related Durability of Cementitious Composites*, 2016, pp. 1–10. [Online]. Available: https://www.researchgate.net/publication/306159054.

[42] I. Garcia-Lodeiro, A. Palomo, A. Fernández-Jiménez, and D. E. MacPhee, "Compatibility studies between N-A-S-H and C-A-S-H gels. Study in the ternary diagram Na2O–CaO–Al2O3–SiO2–H2O," *Cement and Concrete Research*, vol. 41, no. 9, pp. 923–931, Sep. 2011, ISSN: 0008-8846. DOI: 10.1016/J.CEMCONRES.2011.05.006.

[43] I. Ismail, S. A. Bernal, J. L. Provis, R. San Nicolas, S. Hamdan, and J. S. Van Deventer, "Modification of phase evolution in alkali-activated blast furnace slag by the incorporation of fly ash," *Cement and Concrete Composites*, vol. 45, pp. 125–135, 2014, ISSN: 09589465. DOI: 10.1016/j.cemconcomp.2013.09.006.

[44] S. Wang, "Alkaline activation of slag," Tech. Rep., 1995.

[45] B. Walkley, R. San Nicolas, M. A. Sani, G. J. Rees, J. V. Hanna, J. S. van Deventer, and J. L. Provis, "Phase evolution of C-(N)-A-S-H/N-A-S-H gel blends investigated via alkali-activation of synthetic calcium aluminosilicate precursors," *Cement and Concrete Research*, vol. 89, pp. 120–135, Nov. 2016, ISSN: 00088846. DOI: 10.1016/j.cemconres.2016.08.010.

[46] M. Criado, A. Fernández-Jiménez, and A. Palomo, "Alkali activation of fly ash. Part III: Effect of curing conditions on reaction and its graphical description," *Fuel*, vol. 89, no. 11, pp. 3185–3192, Nov. 2010, ISSN: 0016-2361. DOI: 10.1016/J.FUEL.2010.03.051.

[47] G. Kovalchuk, A. Fernández-Jiménez, and A. Palomo, *Alkali-activated fly ash: Effect of thermal curing conditions on mechanical and microstructural development - Part II*, Feb. 2007. DOI: 10.1016/j.fuel.2006.07.010.

[48] Y. Cai, L. Yu, Y. Yang, Y. Gao, and C. Yang, "Effect of early age-curing methods on drying shrinkage of alkali-activated slag concrete," *Materials*, vol. 12, no. 10, May 2019, ISSN: 19961944. DOI: 10.3390/ma12101633.

[49] K. Kovler and S. Zhutovsky, "Overview and future trends of shrinkage research," in *Materials and Structures*, vol. 39, Springer Netherlands, 2006, pp. 827–847. DOI: 10.1617/s11527-006-9114-z.

[50] H. Ye and A. Radlińska, *A Review and Comparative Study of Existing Shrinkage Prediction Models for Portland and Non-Portland Cementitious Materials*, 2016. DOI: 10.1155/2016/2418219.

[51] ASTM C596, “Standard Test Method for Drying Shrinkage of Mortar Containing Hydraulic Cement,” 2009. DOI: DOI:10.1520/C0596-23.

[52] ASTM C1698-09, “Standard Test Method for Autogenous Strain of Cement Paste and Mortar,” 2009. DOI: DOI:10.1520/C1698-19.

[53] G. Wang and Y. Ma, “Drying shrinkage of alkali-activated fly ash/slag blended system,” *Journal of Sustainable Cement-Based Materials*, vol. 7, no. 4, pp. 203–213, Jul. 2018, ISSN: 21650381. DOI: 10.1080/21650373.2018.1471424.

[54] S. Mindess, J. Young, and D. Darwing, *Concrete*, 2nd. Prentice Hall, 2003.

[55] A. Fernández-Jiménez, A. Palomo, and M. Criado, “Engineering Properties of alkali-activated fly ash concrete,” *ACI Materials Journal*, vol. 103, pp. 106–112, 2006. [Online]. Available: https://www.researchgate.net/publication/279897807.

[56] Y. Ma, J. Hu, and G. Ye, “The pore structure and permeability of alkali activated fly ash,” *Fuel*, vol. 104, pp. 771–780, Feb. 2013, ISSN: 0016-2361. DOI: 10.1016/J.FUEL.2012.05.034.

[57] Z. Li, J. Liu, and G. Ye, “Drying shrinkage of alkali-activated slag and fly ash concrete; A comparative study with ordinary Portland cement concrete,” *Heron*, vol. 64, no. 1/2, pp. 01–15, 2019.

[58] M. Nedeljković, B. Šavija, Y. Zuo, M. Luković, and G. Ye, “Effect of natural carbonation on the pore structure and elastic modulus of the alkali-activated fly ash and slag pastes,” *Construction and Building Materials*, vol. 161, pp. 687–704, Feb. 2018, ISSN: 09500618. DOI: 10.1016/j.conbuildmat.2017.12.005.

[59] D. Hou, Y. Zhang, T. Yang, J. Zhang, H. Pei, J. Zhang, J. Jiang, and T. Li, “Molecular structure, dynamics, and mechanical behavior of sodium aluminosilicate hydrate (NASH) gel at elevated temperature: A molecular dynamics study,” *Physical Chemistry Chemical Physics*, vol. 20, no. 31, pp. 20 695–20 711, 2018, ISSN: 14639076. DOI: 10.1039/c8cp03411g.

[60] N. K. Lee, J. G. Jang, and H. K. Lee, “Shrinkage characteristics of alkali-activated fly ash/slag paste and mortar at early ages,” *Cement and Concrete Composites*, vol. 53, pp. 239–248, 2014, ISSN: 09589465. DOI: 10.1016/j.cemconcomp.2014.07.007.

[61] C. Yong, “Shrinkage behaviour of geopolymers,” Ph.D. dissertation, University of Melbourne, 2010.

[62] F. Puertas, M. Palacios, H. Manzano, J. S. Dolado, A. Rico, and J. Rodriguez, *C-A-S-H gels formed in alkali-activated slag cement pastes. Structure and effect on cement properties and durability*, 2014. DOI: 10.1051/C. [Online]. Available: http://dx.doi.org/10.1051/matecconf/20141101002.

[63] Y. Ma, *Microstructure and engineering properties of alkali activated fly ash : as an environment friendly alternative to Portland cement.* [s.n.], 2013, ISBN: 9789461862266.

[64] S. Aydin and B. Baradan, “Effect of activator type and content on properties of alkali-activated slag mortars,” *Composites Part B: Engineering*, vol. 57, pp. 166–172, Feb. 2014, ISSN: 1359-8368. DOI: 10.1016/J.COMPOSITESB.2013.10.001.

[65] B. Chen, “Utilization of MSWI bottom ash as mineral resource for low-carbon constructuion materials,” Ph.D. dissertation, 2023.

[66] NEN-EN 196-1, “Methods of testing cement - Part 1: Determination of strength,” 2016.

[67] NEN-EN 196-3, “Methods of testing cement - Part 3: Determination of setting times and soundness,” 2016.

[68] M. R. Ahmad, L. P. Qian, Y. Fang, A. Wang, and J. G. Dai, “A multiscale study on gel composition of hybrid alkali-activated materials partially utilizing air pollution control residue as an activator,” *Cement and Concrete Composites*, vol. 136, p. 104 856, Feb. 2023, ISSN: 0958-9465. DOI: 10.1016/J.CEMCONCOMP.2022.104856.

[69] M. A. Yazdi, M. Liebscher, S. Hempel, J. Yang, and V. Mechtcherine, “Correlation of microstructural and mechanical properties of geopolymers produced from fly ash and slag at room temperature,” *Construction and Building Materials*, vol. 191, pp. 330–341, Dec. 2018, ISSN: 09500618. DOI: 10.1016/j.conbuildmat.2018.10.037.

[70] B. Sun, Y. Sun, G. Ye, and G. De Schutter, “A mix design methodology of slag and fly ash-based alkali-activated paste,” *Cement and Concrete Composites*, vol. 126, p. 104 368, Feb. 2022, ISSN: 0958-9465. DOI: 10.1016/J.CEMCONCOMP.2021.104368.

[71] C. Duran Atiş, C. Bilim, Ö. Çelik, and O. Karahan, “Influence of activator on the strength and drying shrinkage of alkali-activated slag mortar,” *Construction and Building Materials*, vol. 23, no. 1, pp. 548–555, Jan. 2009, ISSN: 09500618. DOI: 10.1016/j.conbuildmat.2007.10.011.

[72] Z. Li, T. Lu, X. Liang, H. Dong, and G. Ye, “Mechanisms of autogenous shrinkage of alkali-activated slag and fly ash pastes,” *Cement and Concrete Research*, vol. 135, Sep. 2020, ISSN: 00088846. DOI: 10.1016/j.cemconres.2020.106107.

[73] C. Liu, X. Liang, Y. Chen, Z. Li, and G. Ye, “Degradation of alkali-activated slag subjected to water immersion,” *Cement and Concrete Composites*, vol. 142, p. 105 157, Sep. 2023, ISSN: 0958-9465. DOI: 10.1016/J.CEMCONCOMP.2023.105157.

[74] M. B. Haha, B. Lothenbach, G. Le Saout, and F. Winnefeld, “Influence of slag chemistry on the hydration of alkali-activated blast-furnace slag — Part I: Effect of MgO,” *Cement and Concrete Research*, vol. 41, no. 9, pp. 955–963, Sep. 2011, ISSN: 0008-8846. DOI: 10.1016/J.CEMCONRES.2011.05.002.

[75] S. A. Bernal, R. San Nicolas, R. J. Myers, R. Mejía De Gutiérrez, F. Puertas, J. S. Van Deventer, and J. L. Provis, “MgO content of slag controls phase evolution and structural changes induced by accelerated carbonation in alkali-activated binders,” *Cement and Concrete Research*, vol. 57, pp. 33–43, Mar. 2014, ISSN: 0008-8846. DOI: 10.1016/J.CEMCONRES.2013.12.003.

[76] M. Nedeljković, Z. Li, and G. Ye, “Setting, strength, and autogenous shrinkage of alkali-activated fly ash and slag pastes: Effect of slag content,” *Materials*, vol. 11, no. 11, Oct. 2018, ISSN: 19961944. DOI: 10.3390/ma11112121.

A

Remaining results

A.1. Original data set of flexural and compressive strength results

Table A.1: Flexural strength of all samples in MPa

	T3	T7	T14	T28
S100N4	10.3	11.9	12.4	12.9
S70N4	5.9	9.7	10.1	10.6
S50N4	4.4	5.5	6.6	7.0
S70N5	6.6	7.2	5.7	7.7
S50N5	4.8	4.8	5.7	6.8

Table A.2: Compressive strength of all samples in MPa

	T3	T7	T14	T28
S100N4	39.9	47.1	49.3	57.9
S70N4	43.1	45.2	54.6	57.9
S50N4	31.1	43.8	52.3	56.1
S70N5	51.7	58.9	61.1	66.5
S50N5	44.5	52.8	58.2	64.0

A.2. Drying shrinkage and weight loss results of N5 samples

A.2.1. 70% BFS, 5 wt.% Na_2O content

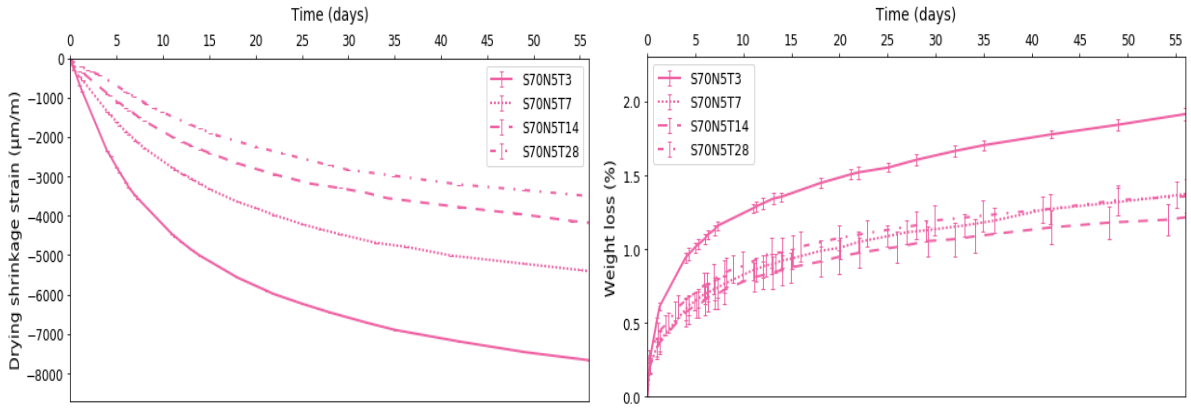

(a) Drying shrinkage strain

(b) Weight loss

Figure A.1: Drying shrinkage strain and weight loss of samples with 70% slag and 5 wt. % Na_2O content

A.2.2. 50% BFS, 5 wt.% Na_2O content

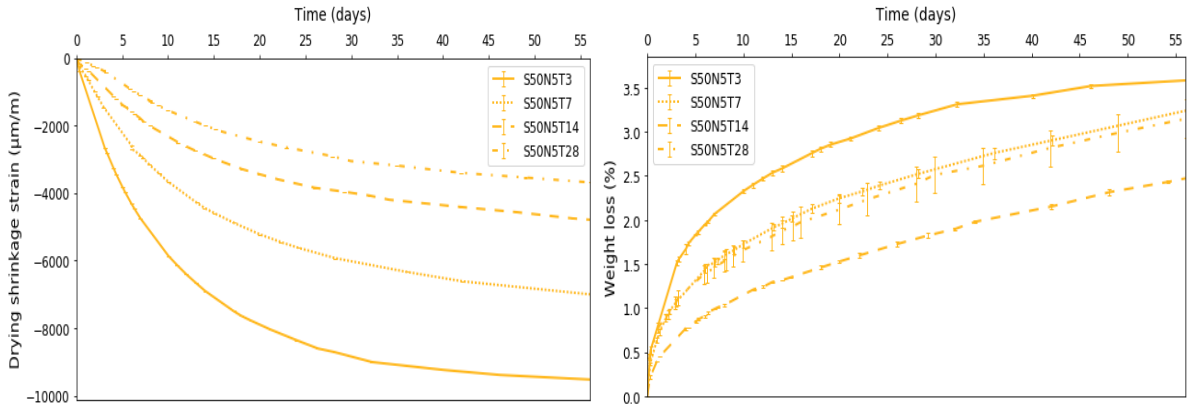

(a) Drying shrinkage strain **(b)** Weight loss

Figure A.2: Drying shrinkage strain and weight loss of samples with 50% slag and 5 wt.% Na_2O content

A.2.3. 50% BFS, 4 and 5 wt.% Na_2O content, 7 and 14 curing days

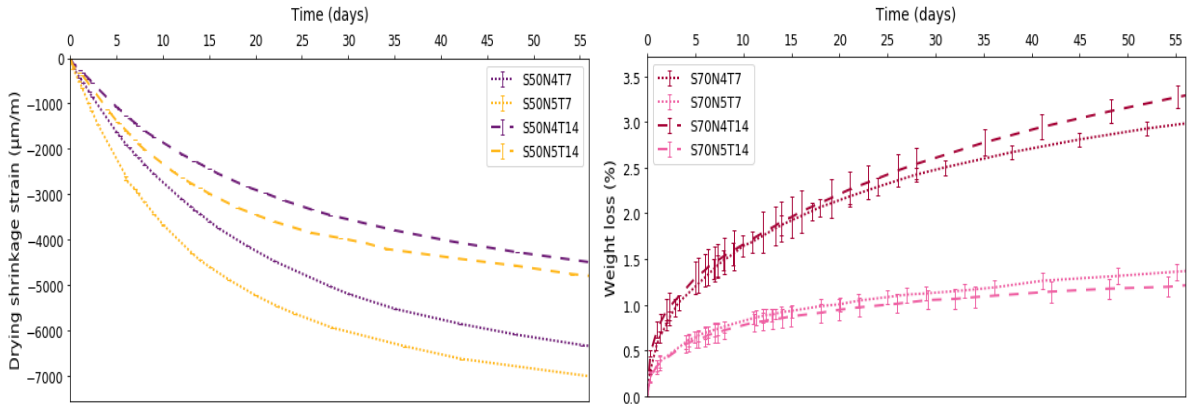

(a) Drying shrinkage strain **(b)** Weight loss

Figure A.3: Drying shrinkage strains and weight loss of samples with 70% slag and 4 or 5 wt.% Na_2O content after 7 and 14 days of curing

A.2.4. 70% BFS, 4 and 5 wt.% Na_2O content

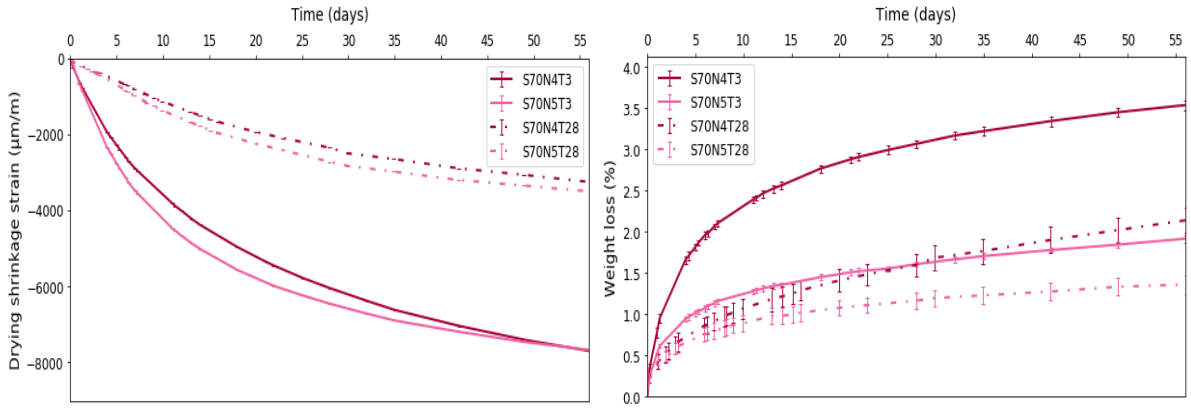

(a) Drying shrinkage strain **(b)** Weight loss

Figure A.4: Drying shrinkage strains and weight loss of samples with 70% slag and 4 or 5 wt.% Na_2O content after 3 and 28 curing days

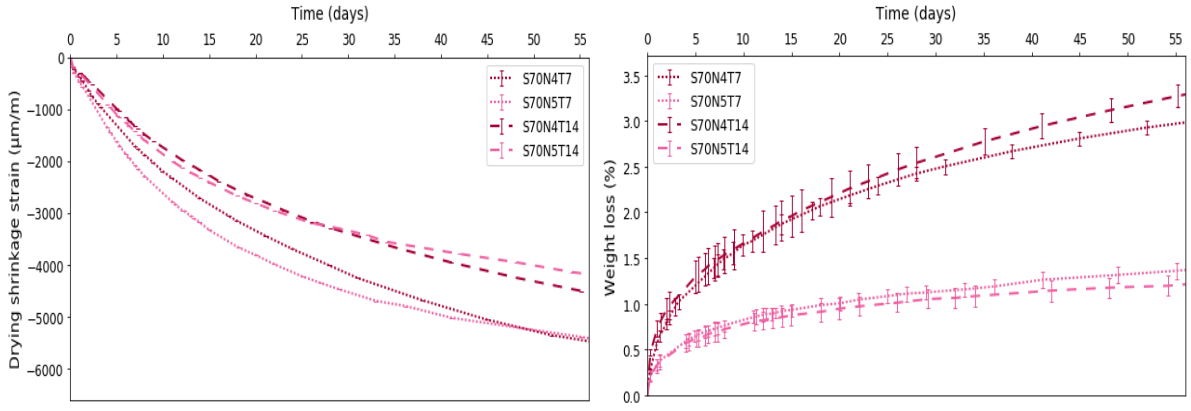

(a) Drying shrinkage strain **(b)** Weight loss

Figure A.5: Drying shrinkage strains and weight loss of samples with 70% slag and 4 or 5 wt.% Na_2O content after 7 and 14 curing days

B

Pictures of samples after compressive strength test

(a) S100N4T28

(b) S70N4T14

(c) S50N4T14

Figure B.1: Pictures of samples after compressive strength test, showing brittle failure

C

Pictures of samples during drying shrinkage measurements

(a) S50N4T3 after 3 days of exposure

(b) S50N5T3 after 3 days of exposure

(c) S50N4T3 after 28 days of exposure

(d) S50N5T3 after 33 days of exposure

Figure C.1: Pictures of samples with 50% GGBFS during drying shrinkage measurements

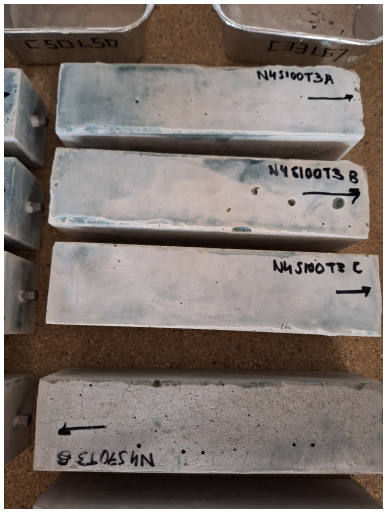

(a) S100N4T3 after 3 days of exposure

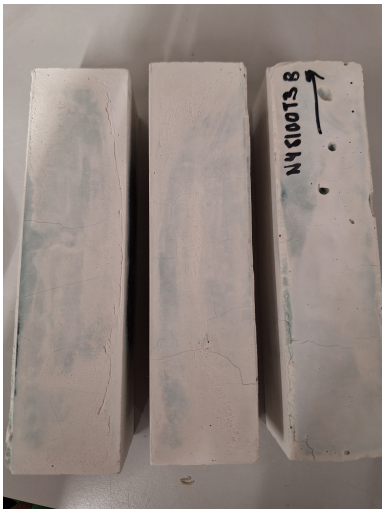

(b) S100N4T3 after 28 days of exposure

Figure C.2: Pictures of samples with 100% GGBFS during drying shrinkage measurements